



Esko Lahdenperä

**MASS TRANSFER MODELING IN SLOW-RELEASE
DISSOLUTION AND IN REACTIVE EXTRACTION
USING EXPERIMENTAL VERIFICATION**



Esko Lahdenperä

MASS TRANSFER MODELING IN SLOW-RELEASE DISSOLUTION AND IN REACTIVE EXTRACTION USING EXPERIMENTAL VERIFICATION

Dissertation for the degree of Doctor of Science (Technology) to be presented with due permission for public examination and criticism in Auditorium 2310 at Lappeenranta-Lahti University of Technology LUT, Lappeenranta, Finland on the 5th of December, 2019, at noon.

Acta Universitatis
Lappeenrantaensis 876

Supervisor Professor Tuomas Koiranen
LUT School of Engineering Science
Lappeenranta-Lahti University of Technology LUT
Finland

Reviewers Professor Anders Brink
Laboratory of Process and Systems Engineering
Åbo Akademi
Finland

Associate Professor Pekka Oinas
Department of Chemical and Metallurgical Engineering
Aalto University
Finland

Opponent Associate Professor Pekka Oinas
Department of Chemical and Metallurgical Engineering
Aalto University
Finland

ISBN 978-952-335-436-4
ISBN 978-952-335-437-1 (PDF)
ISSN 1456-4491
ISSN-L 1456-4491

Lappeenranta-Lahti University of Technology LUT
LUT University Press 2019

Abstract

Esko Lahdenperä

Mass transfer modeling in slow-release dissolution and in reactive extraction using experimental verification

Lappeenranta, 2019

81 pages

Acta Universitatis Lappeenrantaensis 876

Diss. Lappeenranta-Lahti University of Technology LUT

ISBN 978-952-335-436-4, ISBN 978-952-335-437-1 (PDF), ISSN 1456-4491,

ISSN-L 1456-4491

In this thesis, models related to mass transfer operations were studied in two cases. One study case was the dissolution of potassium chloride (KCl) particles in water, and another study case was the reactive solvent extraction of metal ions from aqueous solution into an organic droplet. In these study cases, the common point was that mass transport takes place over a phase boundary. However, the system structure and the hydrodynamic behavior of the interfaces are different. These differences are reflected in the mass transfer models. In the dissolution of KCl particles, the system is a suspension, and the measured parameters are averages. The phase interface is rigid between the particle and solution. In solvent extraction, the system consists of a single droplet surrounded by a large continuous phase. The interface between the droplet and the continuous phase is dynamic.

The dissolution rate of the KCl particles was controlled by using a suitable coating. Two coating materials were used: native starch and lignin. Native starch is water soluble and has a tendency to form hydrogels. Conversely, lignin is insoluble in neutral water. In addition, experiments with two uncoated KCl particles were performed. Four models were evaluated to find a suitable model to predict the dissolution: (1) a reaction kinetic model, (2) a gel model, (3) an active surface model, and (4) an active surface model assuming diffusion layer thickness is equal to particle radius. Model (1) was able to give acceptable predictions for all particles. For starch-coated particles, dissolution was explained by the gel model (2). For the lignin-coated particles, the active surface model (4) was found to be suitable.

Mass transfer in reactive solvent extraction was studied using single droplet experiments. Cu ions were extracted from the aqueous solution into a droplet where the organic solvent contained an extractant. A new image analysis method was developed to measure droplet concentration, size, and velocity. Using the new analysis method, models of mass transfer were formulated for the droplet formation, droplet rise, and droplet coalescence stages.

For droplet formation, a new empirical model was formulated taking into account the molecular diffusion coefficient, the empirical eddy diffusivity, and an empirical sur-

face mobility parameter. A numerical model was constructed to simulate droplet formation, and the model showed that in this system, the velocity profile in the droplet during formation was non-circulating. The new model was able to better predict the mass transfer during formation when compared with findings from the literature. For mass transfer during the droplet rise, an existing empirical method was modified by using a numerical model where conservation of momentum and the mass transport equation were used to calculate mass transfer between the continuous phase and the droplet. The model predicts mass transfer coefficients and extraction reaction kinetic constants. It was recognized, that in this system, the mass transfer resistance was located at the phase interface.

The effect of droplet coalescence on the mass transfer was studied experimentally by letting two droplets coalesce in a controlled manner. The coalescence process was recorded on video. Based on concentration analysis, it was recognized that mass transfer is not affected by droplet coalescence. In addition, a droplet coalescence process is not affected by mass transfer. A numerical model of a droplet coalescence process was built and validated with experimental results.

Keywords: mass transfer, models, dissolution, solvent extraction

Acknowledgments

This dissertation is based on studies that were carried out at Lappeenranta-Lahti University of Technology LUT over the period of 2014–2019. This study has also received funding from Finnish Academy project *Analysis of polydispersity in reactive liquid-liquid systems* and the financial support is gratefully acknowledged.

I wish to express my gratitude to my supervisor, Professor Tuomas Koiranen, for his encouragement, guidance and patience during this work. The reviewers of this manuscript are acknowledged; Professor Anders Brink is thanked for his careful evaluation and suggestions for correction and Associate Professor Pekka Oinas is thanked for his valuable comments and questions.

Professor Ville Alopaeus and his research group at Aalto University are thanked for the inspiring co-operation during the project *Analysis of polydispersity in reactive liquid-liquid systems*.

Professors J.A.M. Kuipers and N.G. Deen and their research group are thanked for offering a fruitful and enjoyable 5 month period as a visiting researcher in the Laboratory of Multi-scale Modelling of Multi-phase Flows in TUE Eindhoven, Netherlands.

I am also grateful to my co-authors, particularly M.Sc. Jussi Tamminen from LUT for his experimental and modeling efforts and stimulating discussions.

I would like to express my sincere thanks to the current and former staff of our research group.

Finally, I owe my family, relatives, and friends a debt of gratitude for their support.

Esko Lahdenperä
October 2019
Lappeenranta, Finland

Contents

Abstract

Acknowledgements

Contents

List of publications	9
Nomenclature	11
1 Introduction	17
1.1 Process design and mass transfer	17
1.2 Thesis goal	18
1.3 Thesis outline	19
1.4 New results	20
2 Interfacial mass transfer models	21
2.1 Interface description	21
2.2 Solid particle dissolution	24
2.2.1 Empirical models	25
2.2.2 Mechanistic models	25
2.3 Single liquid droplets	30
2.3.1 Single droplet experiments	30
2.3.2 Mass transfer to droplets	33
2.3.3 Mass transfer with interface reaction	37
2.3.4 Droplet coalescence and mass transfer	37
2.3.5 Mass transfer numerical modeling	38
3 Dissolution of slow release particles	41
3.1 Models of KCl dissolution	41
3.2 Dissolution modeling: results and discussion	43
3.2.1 Reaction rate model	43
3.2.2 Constant gel radius model	43
3.2.3 Active surface model	44
3.2.4 Active surface model having diffusion layer thickness equal to particle radius	46
4 Image analysis based concentration measurement in single droplet experi- ments	49
4.1 Direct measurement: principle	49
4.2 Examples	53
4.3 Discussion	53

5	Mass transfer during droplet formation and rise	55
5.1	Mass transfer during droplet formation	55
5.2	Mass transfer during droplet rise	58
6	Mass transfer during droplet coalescence	63
6.1	Coalescence experiments	63
6.1.1	Mass transfer during droplet coalescence	64
6.1.2	Droplet rest time distribution	65
6.2	Modeling of the coalescence process	67
6.3	Discussion	69
6.3.1	Experimental results	69
6.3.2	Modeling results	69
7	Conclusions and suggestions for future work	71
7.1	Conclusions	71
7.2	Future work	72
	References	73
	Publications	83

List of publications and author's contribution

This dissertation consists of an introductory part and four original, refereed articles in scientific journals. The articles and the author's contribution in them is summarized below.

- I **E. Lahdenperä and T. Koironen.** A Novel Manufacturing Method for Sustained Release Products and Modelling Dissolution, *Journal of Thermodynamics & Catalysis*, 7(1), 2016, DOI: 10.4172/2157-7544.1000159.
- II **J. Tamminen, E. Lahdenperä, T. Koironen, T. Kuronen, T. Eerola, L. Lensu, H. Kälviäinen.** Determination of single droplet sizes, velocities and concentrations with image analysis for reactive extraction of copper, *Chemical Engineering Science*, 167, pp. 54–69, 2017, DOI: 10.1016/j.ces.2017.03.048.
- III **E. Lahdenperä, J. Tamminen, T. Koironen, T. Kuronen, T. Eerola, L. Lensu, H. Kälviäinen.** Modeling mass transfer during single organic droplet formation and rise, *Journal of Chemical Engineering & Process Technology*, 9(2), 2018, DOI: 10.4172/2157-7048.1000378.
- IV **J. Tamminen, E. Lahdenperä, T. Koironen, T. Kuronen, T. Eerola, L. Lensu, H. Kälviäinen.** The mass transfer and coalescence time scales in binary droplet systems for copper extraction, *Journal of Chemical Engineering & Process Technology*, 9(4), 2018, DOI: 10.4172/2157-7048.1000387.

Esko Lahdenperä is the principal author of papers I and III and has participated in writing papers II and IV and he has computed and analyzed the results in papers I,II and III and IV. He has participated in experimental work in papers II, III and IV.

Nomenclature

Symbols

A	area, m^2
a	active surface ratio, ratio of active surface to the total surface in particle dissolution, –
a, b	coefficients in Weibull dissolution model, –
A	absorbance, –
a_1	coefficient in Popovich droplet formation model, –
c	mass concentration, kg/m^3
c	molar concentration, mol/m^3
$c.i.$	parameter confidence interval
D	diameter, m
\mathcal{D}	diffusivity, m^2/s
d_e	volume equivalent droplet diameter, m
\mathcal{D}_E	eddy diffusion coefficient, m^2/s
\mathcal{D}_{eff}	effective diffusion coefficient, m^2/s
\mathcal{D}_m	molecular diffusion coefficient, m^2/s
e	ratio of the effective diffusivity and diffusivity in water in the constant gel layer model, –
E	extraction ratio, $(c_d - c_{d,0}) / (c_d^* - c_{d,0})$, –
E_d	extraction ratio when there are no concentration changes, –
f_v	stagnant part volume fraction in stagnant cap model, –
h	diffusion layer thickness, m
K	overall mass transfer coefficient, m/s
k	local mass transfer coefficient, m/s
K, K_1	coefficients in empirical dissolution models, Table 2.1
k'	dissolution: empirical constant in Eq. (2.9), $m^{1/2}$
k_R	dissolution: empirical constant in the reaction rate model, 1/s
$k_{H,F}$	interface mobility parameter in formation, –
$k_{H,R}$	interface mobility parameter in rise, –
K^*	partition coefficient

$k_{R,A}$	area based reaction kinetic constant, $m^4/mol\ s$
$k_{R,A}^0$	maximum reaction kinetic constant, area based, $m^4/mol\ s$
k_R^+	forward reaction rate constant in Eq. (2.38), –
L_{ch}	chord length of the light beam passing a droplet, m
L	characteristic dimension in Sherwood number, m
L	length, m
m	mass, kg
N	number
n	amount of moles, mol
n	exponent in Korsmayer–Peppas dissolution model, –
n	forward reaction rate order in Eq. (2.38), –
N''	molar flux, $mol/(s\ m^2)$
p	pressure, Pa
R	mass transfer resistance, s/m
r, R	radius, m
R_A	area based reaction rate, $mol/(s\ m^2)$
R^2	goodness of fit, –
<i>s.d.</i>	standard deviation
<i>s.e.</i>	parameter standard error
SSQ	sum of squares
t	time, s
u	velocity, m/s
V	volume, m^3
\dot{V}	volumetric feed rate, m^3/s
W	total mass of particles, kg
z	ratio of diffusion layer thickness to particle initial diameter, $h/R_{p,0}$, –

Greek letters

θ	contact angle, rad
δ	apparent diffusion layer thickness, m
Δ	difference
ε	apparent absorptivity in droplet concentration determination, $L/mmol/mm$

ε	Level-Set method, interface thickness controlling parameter, m
γ	Level-Set method, reinitialization parameter, m/s
κ	viscosity ratio, μ_d/μ_c , -
ϕ	Level-Set function, -
Ψ	property
ρ	density, kg/m ³
τ	dissolution lag time in Weibull dissolution model, s
μ	dynamic viscosity, kg/(m s)

Subscripts

0	initial state
1, 2	species indices, phase indices
c	continuous phase, column
cell	cell in computational grid
ch	chord
coal	coalesced droplet
d	droplet phase
E	eddy diffusivity
e	estimation
eff	effective diffusivity
F	formation
f	final dissolved concentration in bulk
G	gel + core in gel model
g	volume force
<i>i</i>	species index, feed, inlet, interface
∞	concentration in bulk
in	inlet
if	interface
L	liquid phase
m	measurement
out	outlet
P	pendant droplet

p	particle, penetration
R	rise
r	rest time
S	sessile droplet
st	surface tension
tot	overall, total
t	terminal velocity
x, y	phases x and y

Superscripts

*	equilibrium concentration
---	---------------------------

Abbreviations, units

CFD	Computational Fluid Dynamics
D[4,3]	volume or mass moment mean – De Brouckere mean diameter
LS	Level-Set
SEM	Scanning Electron Microscopy
VOF	Volume-of-Fluid
vol %	volume percent
w %	weight percent

Dimensionless numbers

Fo _d	droplet Fourier number in formation, $4\mathcal{D}_m t_F / d_e^2$
Fo' _d	modified droplet Fourier number in formation, $4\mathcal{D}_{F,eff} t_F / d_e^2$
Pe _{cell}	cell Peclet number, UL_{cell} / \mathcal{D}
Re	droplet Reynolds number, $\rho u_t d_e / \mu_c$
Sc	Schmidt number, $\mu / (\rho \mathcal{D}_m)$
Sh	Sherwood number, kL / \mathcal{D}_m

Overbar

–	average
---	---------

Operators

∇	partial derivative operator
d/d⟨x⟩	ordinary derivative with respect to variable ⟨x⟩
$\partial/\partial\langle x \rangle$	partial derivative with respect to variable ⟨x⟩

T matrix transpose

Matrices

F_g volume force field, N/m³

F_{st} surface force field, N/m³

I identity matrix

u velocity field, m/s

Introduction

1.1 Process design and mass transfer

In most chemical industrial processes, mass transfer is an essential transfer phenomenon. It is an important factor in the design of products and processes that use less material and are cheaper, safer and environmentally friendly. To obtain the most optimal result and to lower the costs involved in the process and product development requires the development of models and modeling methods in parallel with experimental practices. By applying rigorous and detailed models, time-consuming and costly pilot-plant experiments can be partially or fully replaced (Eiswirth et al., 2011). This can be accomplished by developing models that are as accurate as possible given the limits of available resources. The ultimate goal is to gain a deep enough understanding about the mass transfer phenomenon that the mass transport parameters can be determined through experiments using a laboratory scale unit or a small pilot-plant. The full-scale unit is then designed using an accurate model with the experimentally determined parameters. In most cases, this requires that the models are based on the conservation of mass, energy, and momentum. In practice, the ultimate problem is how models can be simplified in order to minimize the number of experimentally tunable model parameters and how to minimize the computational burden when the models are solved.

Mass transfer is interlinked with two other transport phenomena: heat transfer and momentum transport. In principle, this mutual interdependence should be considered in mass transfer models. These three transport phenomena are generally included in the models of fluid systems using continuum mechanics, where the system properties are assumed to be continuous functions of space coordinates. However, transport phenomena are approximations of the true physical reality of atomic-level phenomena.

Aside from certain simplified formulations, transport phenomena based models have remained unsolvable until recently because of computational complexity, missing understanding about profound physical phenomena, and lack of experimental data for physical properties. (Bird, 2004) Due to advancements in computational hardware and numerical algorithms combining with the formulation of theories and vast amount of experimental data on physical properties, today's scientists have an opportunity to formulate and solve complex problems in transport phenomena. Bird (2004) listed some challenges for this area of research, particularly emphasizing mass transfer, the need

for measurements of diffusivity, and transport properties in multicomponent systems. These problems have been approached by Peters et al. (2017) and Babaei et al. (2018), among others. Topics of current interests in transport phenomena research not considered by Bird include transport phenomena of complex fluids (Lee et al., 2017) and multiscale modeling of interfaces, especially in nanotechnology (Cardellini et al., 2016).

In designing mass transfer units, the goal is to design equipment at the lowest cost while also taking into account the design constraints. This often means that the unit size is as small as possible. If the main purpose is to minimize the unit size, then the mass transfer rate has to be maximized. The mass transfer rate between phases depends on three factors: mass transfer area, mass transfer driving force, and mass transfer coefficient. Smaller droplets are generated in the case of liquid–liquid systems, when the fluid shear rate is increased, and thus the available mass transfer area is increased. The increasing shear rate also affects the mass transfer coefficient. The boundary layer around objects becomes thinner, meaning the mass transfer resistance decreases, and the mass transfer coefficient becomes larger. Additionally, the increased shear rate can be used to maintain driving force due to transporting the species from the phase boundary to the bulk.

Mass transfer rate control is an implicit design object in applications where valuable material dissolution control is a design issue. The goal is to have environmentally friendly, safer, and cheaper products. Examples of these applications can be found in, for example, pharmaceutical applications (Chaudhari et al., 2012; Kola and Kumar, 2013; Mahapatra et al., 2013) and agricultural applications (Hanafi et al., 2000; Zhan et al., 2004; Wu and Liu, 2008; Han et al., 2009; Azeem et al., 2014). The dissolution models are often empirical, and thus the model and model parameters are application-dependent and extrapolation is not possible outside the variable value range used in experiments. This is a driving force for building dissolution models based on the actual dissolution mechanism because they are more rigid and are not limited to a certain application and variable range.

1.2 Thesis goal

This thesis is a case study where mass transfer between two phases was modeled. Two systems were used. The first utilized solid particles where the dissolution rate was controlled by a coating in order to design slow-release particles. The other was a liquid–liquid system where the transport of metal ions from aqueous solution to organic droplets was modeled.

In dissolution, empirical and mechanistic models were used to model the dissolution of slow release particles. The purpose was to find a model that could predict the dissolution rate and also had explanatory power. Four models were tested: the first-order reaction kinetic model, the gel model, the active surface model, and the active surface model assuming $Sh_p = 2$. The reaction vessel was assumed to be well mixed so the concentrations in the models are volume averages.

Semi-empirical and CFD-based models have been applied in models of single droplet extraction. Single droplet hydrodynamics and mass transfer was modeled in three stages: droplet formation, droplet rise, and droplet coalescence. Mass transfer during droplet formation was modeled using an enhanced Walia–Vir model applying the effective diffusivity principle. The hydrodynamics of formation was modeled with a Level-Set (LS) method in order to validate the non-circulatory formation velocity profile and to test the effect of the contact angle on the droplet internal velocity profile during formation. During the droplet rise, mass transfer was calculated with a CFD model assuming a stagnant phase interface and interfacial reaction, where the critical model parameter tested was an interfacial reaction kinetic constant. The model was validated with experiments. Droplet coalescence hydrodynamics was also modeled with the LS method, where the goal was to determine if the coalescence process was affected by the mass transfer.

1.3 Thesis outline

This thesis starts with Chapter 1 giving an introduction to the basics of mass transfer and its part in process design. Then, the thesis goal is set. The general outline of the thesis is provided, and new results are discussed at the end of this chapter. Chapter 2 is a literature-based review of interfacial mass transfer, mass transfer models, and numerical methods used in working with mass transfer models, with an emphasis on purely empirical models and mechanistic models. The aim of this section is to set up the thesis focus and formulate the research question.

The next section introduces two applications of the mass transfer model: modeling of dissolution of salt particles, and modeling of mass transfer in a single droplet experiment using copper reactive solvent extraction. The dissolution model was based on experiments where potassium chloride (KCl) particles were dissolved in water. The particles were coated with two different materials in order to control their dissolution rate, and empirical and mechanistic models were applied. Scanning electron microscope (SEM) images are provided to give insight into the proposed coating mechanisms. The reactive solvent extraction mass transfer model were designed for copper ion transport from an aqueous continuous phase into an organic droplet in a single droplet experiment. The models are empirical and mechanistic CFD models. Mass transfer was modeled during droplet formation, the rise stage, and during droplet coalescence. A separate chapter, Chapter 4 is devoted to the direct concentration measurement methodology based on image analysis of the droplet.

Finally, conclusions and proposals for future research are given in Chapter 7.

1.4 New results

The following novel and interesting results were obtained in the current study.

Slow release particle dissolution and modeling

- i) The dissolution mechanism of starch-coated KCl particles is different from lignin-coated particles. Starch-coated particle dissolution is explained well with the gel model, and the lignin-coated dissolution is best explained with the active surface model assuming $Sh_p = 2$.

Reactive solvent extraction of copper in single droplet experiments

- ii) Development of single droplet direct concentration measurement that allows concentration determination during all droplet stages in the experimental column.
- iii) A non-circulating droplet formation velocity profile in this system is validated with CFD.
- iv) Stagnant cap model parameters determined with the direct concentration measurement and combined with a CFD model provides the droplet concentration distribution during the droplet rise.
- v) Kinetic constants determined in high shear reactors cannot be used directly in models for macroscopic size droplets.

Mass transfer during droplet coalescence

- vi) Coalescence does not have an enhancing effect on droplet mass transfer.
- vii) Mass transfer does not have an effect on the coalescence process.

Interfacial mass transfer models

The treatment of diffusion can be based on either the kinetic theory of matter or the thermodynamics of irreversible processes (Handlos and Baron, 1957). Handlos and Baron claim that the kinetic theory of liquids is not advanced enough to be useful in the treatment of mass transfer in liquids. Although a substantial amount of new knowledge has been collected about the kinetic theory of liquids (see, for example, Bird, 2004) since the publication of Handlos and Baron's (1957) paper, the treatment of mass transfer in liquids is, today, still based on thermodynamics.

The species are transported due to the tendency to reach thermodynamic equilibrium, which produces entropy. Based on the entropy generation, diffusion flux can be evaluated as a function of the species' chemical potential gradient. Chemical potential in this flux equation can be replaced with species concentration or activity (Handlos and Baron, 1957).

2.1 Interface description

In both dissolution and liquid-liquid extraction, material is transported over the phase interface. When the mass transfer rates are estimated, the interface itself has to be described in a way that can be used to explain the mass transfer phenomenon (Krishna and Taylor, 1986).

The interface between the phases is defined as a finite width zone that separates the bulk phases x and y . In this zone, the value of an intensive physical property (e.g. density, activity, specific heat) Ψ changes from value Ψ_x to Ψ_y , as shown in Figure 2.1 (Krishna and Taylor, 1986). The change of the property Ψ may not follow a monotonic path, and due to the interface, properties can sometimes behave in a very peculiar way (see, for example, Hu et al., 2017). Although the interface occupies only a minimal part of the total volume, interface properties can define the major part of the system (Krishna and Taylor, 1986).

The interface can be modeled as an entity with a particulate, discontinuous structure or as a system that is a continuum where detailed structure can't be recognized (Figure 2.1). The molecular model is, of course, the most fundamental model, and with

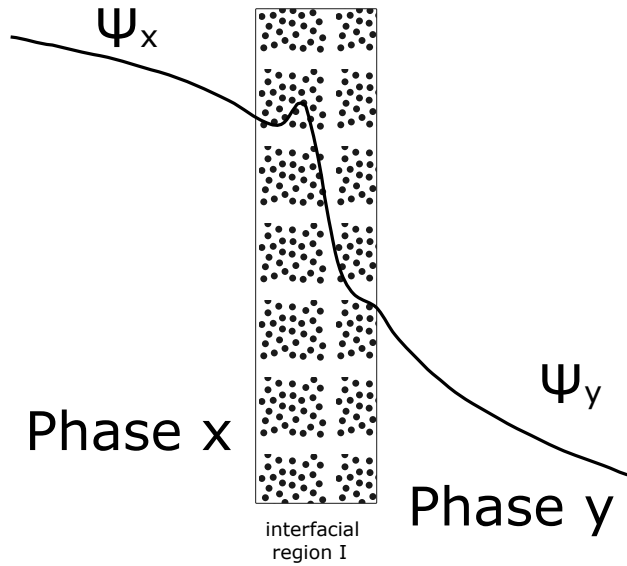


Figure 2.1: Interface region I and property Ψ profile (Krishna and Taylor, 1986, p. 261).

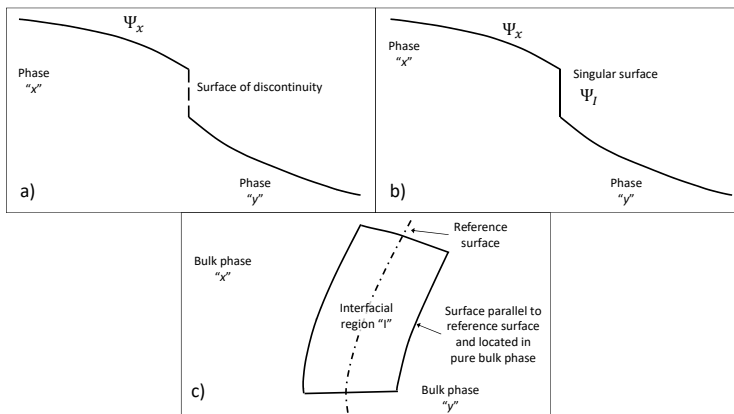


Figure 2.2: Principal models for phase interface. a) Surface of discontinuity; b) Singular surface; c) Transition zone (Krishna and Taylor, 1986, pp. 262–264).

suitable calculations, the macroscopic properties can also be derived, starting from atomic-level properties. However, there are certain advantages to using macroscopic continuum models (Slattery et al., 2007). Three of these continuum models are (Krishna and Taylor, 1986; Slattery et al., 2007)

1. Surface of discontinuity,
2. Singular surface, and
3. Transition zone,

and are shown in Figure 2.2. The transition zone (Figure 2.2c) is a three-dimensional model consisting of a finite width interfacial region. Due to the realistic three-dimensional nature of the interface, it seems obvious that the transition zone model should be utilized, but there are certain inherent problems related to this model. The approach is to use two-dimensional dividing surface models (Slattery et al., 2007). The difference between the surface of discontinuity and singular surface models (Figures 2.2a and b) is that in the former model, the property Ψ does not have any value, while in the singular surface model, the property exhibits the value of Ψ_1 . The model chosen to describe the interface depends on the problem at hand. The deficiency of the simplest model is the inability to catch the effect of the interface on mass transfer (like Marangoni convection), which is possible with the singular surface model (Krishna and Taylor, 1986, p. 263).

At a macroscopic level, there are three principal models for interfacial mass transfer:

1. Film model,
2. Penetration model, and
3. Surface renewal model.

In the film model, it is assumed (as explained earlier) that the phases are separated by a zone having a finite width. Inside the zone, the concentration changes from bulk concentration c_1 to another phase bulk concentration c_2 . The interface itself is assumed to be infinitely thin in comparison to the films where the concentration changes from bulk concentration to interface concentration. It is assumed that at the interface, concentrations are in equilibrium. If there is an interface reaction, then the assumption of a pseudo-steady state is used. This means that the flux of any species from bulk to the interface has to be equal to the reaction rate of the species. Correspondingly, the flux of species diffusing from interface to the bulk has to be the same as the generation rate due to reaction. The film model, although physically not correct, is often a good approximation, and in certain situations, is a viable option.

In penetration theory, it is assumed that the interface itself is periodically renewed with certain lumps of material from the bulk phase. These material lumps remain near the interface for a time and after that period, volume near the surface is renewed and the mass transfer cycle is restarted. The mass transfer is transient, and the model used is the semi-infinite slab model. One weakness of this model is the penetration time Δt_p , which is assumed to be constant, and that is not physically valid.

The physically more accurate approach is the surface renewal model, which is the same as the penetration model except that the parameter penetration time has a certain probability distribution.

When these three models are compared, it can be pointed out that a mass transfer coefficient determined from the film model is higher than the corresponding coefficients in the penetration and surface renewal models. This is due to the higher average driving force in the film model as compared to the penetration and surface renewal models, where the driving forces decrease during the mass transfer cycle.

All three of these models contain empirical parameters. The film model requires a suitable correlation to estimate the mass transfer coefficients, or if not available, they are to be determined experimentally. In the penetration and surface renewal models, the penetration time is the empirical parameter. With the application of CFD models, the determination of the mass transfer coefficients can be performed by simulation using first-principle modeling.

CFD can also be used to model hydrodynamically complex phenomena, for example, liquid–liquid and gas–liquid systems, where droplets and bubbles are deformed, coalesced and broken up, and the shape of these objects is changed. The solution to these problems involves the development of interface resolving numerical methods for two phase flows. These methods, however, are computationally very demanding, especially when time dependent 3D problems are dominated by turbulence, including multiphase systems and phase transport phenomena (Wörner, 2012). These detailed interface resolving simulations are used in, for example, providing data to derive closure equations and to calculate coefficients for interface forces between the bubble–bubble and the bubble–liquid interactions. These equations are used by Euler–Lagrange or Euler–Euler models to simulate the actual bubble column with large time and length scales (Deen et al., 2004). Also mass transfer coefficients using detailed interface resolving simulations have been solved in applications where there is mass transfer present between phases (Darmana et al., 2005; Darmana, 2006; Darmana et al., 2006, 2007).

The following two sections discuss the mass transfer models for dissolution and mass transfer and hydrodynamics for a single droplet formation, rise, and coalescence.

2.2 Mass transfer models for solid particle dissolution

Dissolution models for particles are often empirical. The model parameters for empirical models are application dependent, and the model applicability is limited to the range used in experiments. Direct extrapolation is normally not possible, and in practice, new experiments have to be performed.

The mechanistic models are based on the prevailing physical phenomenon, and their validity is better maintained when it is applied outside the range used in experiments. Also, models based on the physical mechanism are more easily applied in another application.

Dissolution models can be grouped roughly into two classes: pure empirical models and mechanistic models (Cussler, 1999; Costa and Lobo, 2001a,b; Di Colo et al., 2006; Safari et al., 2009).

2.2.1 Empirical models

Table 2.1 tabulates a selection of empirical dissolution models. Pure empirical models are mostly n-th order reaction kinetic functions which can be either analytical functions or a certain release parameter that has been used to characterize the transient dissolution process. For some of these models, the equation can be developed based on theoretical analysis. For instance, with the zero-order kinetics model, when the solute releases slowly, equilibrium is not reached, and the particle area is not changed. Otherwise, the models are empirical or semi-empirical (Costa and Lobo, 2001b).

Table 2.1: Empirical models for dissolution

Model type	Formula	Reference
Zero-order kinetics	$(1 - \frac{m_p}{m_{p,0}}) = Kt$	Costa and Lobo (2001b)
First-order kinetics		
Noyes–Whitney equation	$dc_\infty/dt = K(c^* - c_\infty)$	Noyes and Whitney (1897), Costa and Lobo (2001b)
Brunner equation	$dc/dt = AK_1(c^* - c_\infty)$	Brunner (1904), Costa and Lobo (2001b)
Weibull model	$(1 - \frac{m_p}{m_{p,0}}) = \exp[-(t - \tau)^b/a]$	Costa and Lobo (2001b)
Higuchi model	$(1 - \frac{m_p}{m_{p,0}}) \frac{1}{A} = \sqrt{\mathcal{D}_m(2c^* - c_\infty)c^*t}$	Higuchi (1961, 1963)
Korsmayer–Peppas model	$(1 - \frac{m_p}{m_{p,0}}) = Kt^n$	Korsmeyer et al. (1983); Rit- ger and Peppas (1987a,b)

Symbols: $m_{p,0}$, initial amount of particles; m_p , amount of particles at time t ; K , constant in a model; A , mass transfer area; t , time; c_∞ , concentration of the solute in liquid; c^* , solute equilibrium concentration; a and b , constants in Weibull model; τ , dissolution lag time in Weibull model; \mathcal{D}_m , solute molecular diffusivity; n , exponent in Korsmayer–Peppas model

2.2.2 Mechanistic models

The dissolution mechanism consists of two steps: On the solid surface, molecules are transported into the liquid phase, and then these dissolved molecules are diffused over the diffusion layer into the liquid phase bulk. It is assumed that the detachment of a molecule from the crystal into liquid is faster than diffusion, so the mass transfer from surface to liquid bulk is the rate determining step.

The assumptions made in modeling are (Wang and Flanagan, 1999)

1. A pseudo steady-state, meaning the rate of solid dissolution at the solid-liquid interface is equal to the diffusion mass transfer rate over the diffusion layer around the particle.
2. The solution at the solid-liquid interface is saturated.
3. The Fickian model of diffusion is valid.
4. Bulk concentration c_∞ is ≈ 0 , or $c^* \gg c_\infty$ where c^* is saturation concentration.

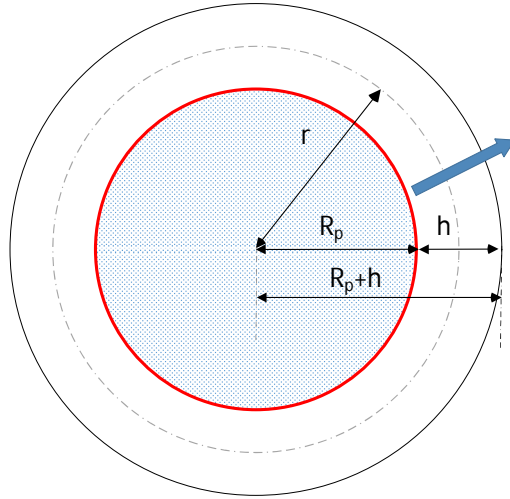


Figure 2.3: Dissolution from a spherical particle over a diffusion layer. R_p , sphere radius; h , diffusion layer thickness; r , location inside the diffusion layer.

Figure 2.3 is a schematic description of the mass transfer from a sphere having radius R_p over the diffusion layer having thickness h . Based on mass balance, the transient mass loss of a particle is equal to the rate of diffusion over the boundary layer having spherical geometry (Wang and Flanagan, 1999):

$$\frac{dm_p}{dt} = -\mathcal{D}_m A \left(\frac{1}{R_p} + \frac{1}{h} \right) (c^* - c_\infty) = -k_c A (c^* - c_\infty), \quad (2.1)$$

where m_p is droplet mass and \mathcal{D}_m is solute diffusivity in the solvent, A is particle area, h is diffusion layer thickness, and k_c is a film mass transfer coefficient on the liquid side. The unit for concentrations c^* and c_∞ is kg/m^3 .

The general solution of Eq. (2.1) (Wang and Flanagan, 1999) using the previously mentioned assumptions is

$$\frac{\mathcal{D}_m c^*}{\rho_p h} t = R_{p,0} - R_p - h \ln \frac{h + R_{p,0}}{h + R_p}. \quad (2.2)$$

According to Wang and Flanagan (1999), three cases can be formulated, depending on the thickness of the diffusion layer h :

1. Diffusion layer h is very thin compared to the initial and prevailing particle radius $R_{p,0}$ and R_p : $R_p, R_{p,0} \gg h$. Then the general solution for Eq. (2.2) is reduced to

$$\frac{\mathcal{D}_m c^*}{\rho_p h} t \simeq R_{p,0} - R_p. \quad (2.3)$$

2. Initial sphere radius $R_{p,0}$ is very small compared to the diffusion layer thickness h : $R_{p,0} \ll h$. Then the general solution to Eq. (2.2) is reduced to

$$\frac{2\mathcal{D}_m c^*}{\rho_p h} t \simeq R_{p,0}^2 - R_p^2. \quad (2.4)$$

3. The diffusion layer thickness does not satisfy either of these conditions.

Wang and Flanagan (1999) introduced the following basic models:

$$m_p^{1/3} = m_{p,0}^{1/3} - k_{1/3} t, \quad (2.5)$$

$$m_p^{1/2} = m_{p,0}^{1/2} - k_{1/2} t, \quad (2.6)$$

$$m_p^{2/3} = m_{p,0}^{2/3} - k_{2/3} t, \quad (2.7)$$

where $k_{1/3}$, $k_{1/2}$, and $k_{2/3}$ are so-called composite rate constants:

$$k_{1/3} = \left(\frac{4\pi\rho_p}{3} \right)^{1/3} \frac{\mathcal{D}_m c^*}{\rho_p h}, \quad (2.8)$$

$$k_{1/2} = \left(\frac{3\pi\rho_p}{2} \right)^{1/2} \frac{\mathcal{D}_m c^*}{\rho_p k'}, \quad (2.9)$$

$$k_{2/3} = \left(\frac{4\pi\rho_p}{3} \right)^{2/3} \frac{2\mathcal{D}_m c^*}{\rho_p}, \quad (2.10)$$

where k' is an empirical coefficient. Eqs. (2.5) and (2.7) correspond to cases 1 and 2, respectively. Eq. (2.6) is a semi empirical model developed by Niebergall et al. (1963) (Wang and Flanagan, 1999). The cube root model (Eq. 2.8) was derived by Hixson and Crowell (1931), and the two-thirds root model (Eq. 2.10) was derived by Higuchi and Hiestand (1963). However, Wang and Flanagan have derived both these models starting from the specific general solutions to Eqs. (2.3) and (2.4). These three exponential

models are the basis of the models used in dissolution testing, and each of them can fit certain experimental data. However, there are no clear-cut rules for selecting between these models (Wang and Flanagan, 1999).

The solution of the diffusive mass transfer equation, Eq. (2.1) uses an assumption that the whole particle area is available for mass transfer and the particle diameter is decreasing. In the gel model, the dissolving particle consists of the solid dissolving core covered with a layer of gel. The dissolving core radius is decreasing but the particle size does not change. The gel model is analogous to the shrinking-core model for a particle of unchanging size (see, for example, Yagi and Kunii, 1955, in Levenspiel, 1999; Safari et al., 2009).

In the gel model, the solute diffuses from the core thorough a layer of gel that produces a substantial mass transfer resistance compared to diffusion in pure liquid. Instead of molecular diffusivity \mathcal{D}_m , the effective diffusivity \mathcal{D}_{eff} is used. Effective diffusivity is a certain fraction e of the solute diffusivity \mathcal{D}_m :

$$\mathcal{D}_{\text{eff}} = e\mathcal{D}_m. \quad (2.11)$$

The mass transfer coefficient k_c is (Cussler, 1999, p. 383)

$$k_c = \frac{\mathcal{D}_{\text{eff}}}{R_G - R_p} = \frac{e\mathcal{D}_m}{R_G - R_p}, \quad (2.12)$$

where R_G is the radius of the dissolving core and the gel, and R_p is the core radius. The dissolution model consists of differential equations for dR_p/dt and dc_∞/dR_p . The first equation is the same as the transient particle mass loss (Eq. 2.1), where mass m_p is converted into radius R_p :

$$\begin{aligned} \frac{dm_p}{dt} &= \rho_p \frac{dV_p}{dt} = \rho_p \frac{4}{3}\pi 3R_p^2 \frac{dR_p}{dt} = -k_c 4\pi R_p^2 (c^* - c_\infty) \\ \Rightarrow \frac{dR_p}{dt} &= \frac{k_c}{\rho_p} (c^* - c_\infty). \end{aligned} \quad (2.13)$$

When k_c from Eq. (2.12) is assigned, the expression of dR_p/dt is

$$\frac{dR_p}{dt} = -\frac{e\mathcal{D}_m}{\rho_p(R_G - R_p)} (c^* - c_\infty). \quad (2.14)$$

dc_∞/dR_p is

$$\frac{dc_\infty}{dR_p} = -\frac{dc_p}{dR_p} = \frac{d}{dR_p} \left(\frac{m_p Z}{V_L} \right) = \rho_p \frac{4}{3}\pi \frac{Z}{V_L} \frac{dR_p^3}{dR_p} = \rho_p 4\pi \frac{Z}{V_L} R_p^2,$$

where ρ_p is particle density, Z is the number of particles, and V_L is the liquid phase volume. Number of particles Z is

$$Z = \frac{V_L c_{p,0}}{m_{p,0}} = \frac{3V_L c_{p,0}}{\rho_p 4\pi R_{p,0}^3}.$$

When the expression of Z is assigned to the expression of dc_∞/dR_p , the final expression is

$$\frac{dc_\infty}{dR_p} = -\frac{3c_{p,0}}{R_{p,0}^3}R_p^2, \quad (2.15)$$

where $c_{p,0}$ is the initial particle concentration, and $R_{p,0}$ is the initial particle radius. This model (Eqs. 2.14 and 2.15) has two parameters: e , the ratio of effective diffusivity to molecular diffusivity, and R_G , the radius of the core and the gel layer.

Another model to explain the dissolution is the active surface model. In this model, only a certain fraction of the particle surface is active. The remaining part is covered with a layer that has so large mass transfer resistance that it can practically be regarded as an impenetrable material, thus decreasing the effective mass transfer area. The active surface model consists of two differential equations. First is Eq. (2.1) (see Wang and Flanagan, 1999):

$$\frac{dR_p}{dt} = -\frac{a\mathcal{D}_m}{\rho_p} \left(\frac{1}{R_p} + \frac{1}{h} \right) (c^* - c_\infty). \quad (2.16)$$

Second is the change of liquid concentration due to radius decrease:

$$\frac{dc_\infty}{dR_p} = -\frac{3c_{p,0}}{R_{p,0}^3}R_p^2. \quad (2.17)$$

The model contains two parameters: 1) a , the ratio of the active surface to the total particle area, and 2) the diffusion layer thickness h . It is assumed that h does not change during the whole dissolution process. This assumption is supported by Wang and Flanagan (2002).

Wang et al. (2012) proposed that for small particles, it is valid to assume $Sh_p = 2$. This means that the apparent diffusion layer thickness $\delta = R_p$ and

$$Sh_p = 2 \Rightarrow \frac{k_c 2R_p}{\mathcal{D}_m} \Rightarrow \frac{\mathcal{D}_m R_p}{\delta \mathcal{D}_m} = 1 \Rightarrow \delta = R_p.$$

Wang and Flanagan (2002) provided an expression for δ in spherical geometry:

$$\frac{1}{\delta} = \frac{1}{R_p} + \frac{1}{h}, \quad (2.18)$$

and in order that $\delta = R_p$, $R_p \ll h$.

Now, the mass transfer coefficient can be calculated directly using $Sh_p = 2$:

$$k_c = \frac{\mathcal{D}_m}{R_p}. \quad (2.19)$$

2.3 Mass transfer models for single liquid droplets

2.3.1 Single droplet experiments

Single droplet experiments are applied to provide experimental data to investigate mass transfer in liquid–liquid systems and to validate numerical models. When the experiments with dispersions in contact units are replaced with experiments with single droplets, the complexity provided by interactions in a multiphase polydispersed system can be reduced, and a better prediction of mass transfer properties can be expected (Wegener et al., 2014).

A droplet is allowed to form at the tip of a needle and, due to difference in densities of the droplet and continuous phases, the droplet rises or settles through the experimental unit and after reaching the end, is collected and analyzed. The experimental methodology is well established, and studies using this method have been consistently derived since the 1930s (see, for example, Sherwood et al., 1939). Newer applications of single droplet experiments in liquid–liquid systems can be found in Biswas et al. (1996), Biswas et al. (1997), Henschke and Pfennig (1999), Kumar and Hartland (1999), Wegener et al. (2009) and Altunok et al. (2012), among others.

As an example of a single droplet unit, Figure 2.4 shows the unit used in this work. Organic solution is fed from the column bottom and droplets are formed at the top of the needle. After rising through the column, the droplets are collected in the funnel.

The mass transfer rate when a droplet is passing through the continuous phase is

$$\bar{N}'' = \frac{V_d}{A_d \Delta t} (c_{\text{in}} - c_{\text{out}}), \quad (2.20)$$

where \bar{N}'' is the molar flux of solute between a droplet and continuous phase having unit $\text{mol}/(\text{m}^2 \text{s})$, V_d is the volume of all droplets, A_d is the droplet area, Δt is the length of time the droplets stay in the column, and c_{in} and c_{out} are droplet inlet and outlet concentrations. Droplet volume is determined based on the feed rate \dot{V}_d :

$$V_d = \dot{V}_d \Delta t / N_d, \quad (2.21)$$

where N_d is the number of droplets in the experimental run and area A_d is $(\pi/4)d_e^2$, where d_e is the volume equivalent spherical droplet diameter (Clift et al., 2013):

$$d_e = \sqrt[3]{\frac{6}{\pi} V_d}. \quad (2.22)$$

Using the concept of volume equivalent spherical droplet diameter d_e and the ratio $A_d/V_d = 6/d_e$ for a spherical droplet, the flux is

$$\bar{N}'' = \frac{6}{d_e \Delta t} (c_{\text{in}} - c_{\text{out}}). \quad (2.23)$$

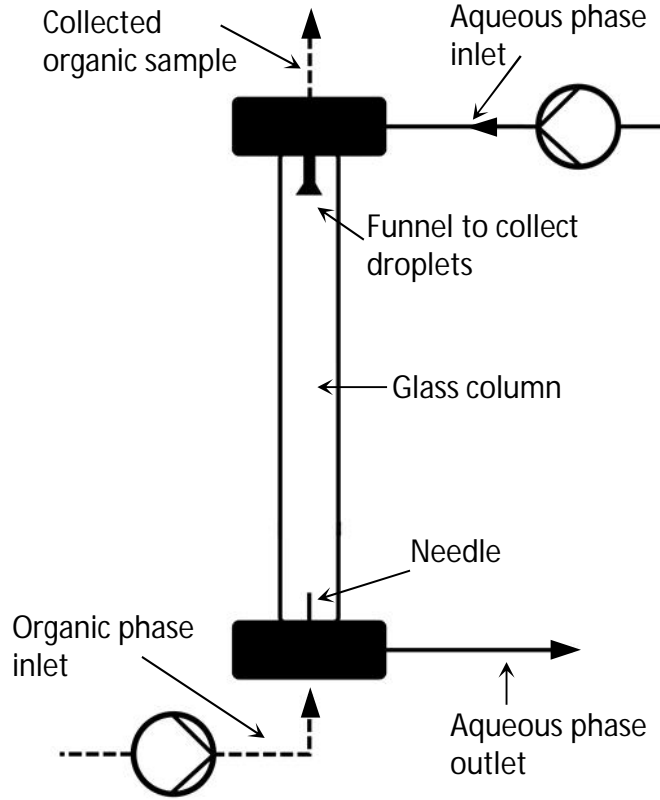


Figure 2.4: Single droplet experimental unit used in this work. The droplet phase is organic, and the continuous phase is aqueous.

The average total mass transfer coefficient \bar{K}_d is calculated by integrating the differential droplet material balance:

$$\begin{aligned}
 \frac{dn}{dt} &= K_d A_d (c^* - c) \\
 \Rightarrow V_d \frac{dc}{dt} &= K_d A_d (c^* - c) \\
 \Rightarrow \frac{dc}{c^* - c} &= K_d \frac{A_d}{V_d} dt = K_d \frac{6}{d_e} dt, \quad (2.24)
 \end{aligned}$$

where K_d is the instantaneous mass transfer coefficient. The average mass transfer

coefficient \bar{K}_d after integration of Eq. (2.24) is

$$\begin{aligned} -\ln \frac{c^* - c_{\text{out}}}{c^* - c_{\text{in}}} &= \bar{K}_d \frac{6}{d_e} \Delta t \\ \Rightarrow \bar{K}_d &= -\ln \frac{c^* - c_{\text{out}}}{c^* - c_{\text{in}}} \frac{d_e}{6\Delta t}, \end{aligned} \quad (2.25)$$

where c^* is the corresponding equilibrium concentration related to the continuous phase concentration. The concentration in the continuous phase is assumed to remain constant because the phase volume is large when compared with the amount of solute transferred.

The problem with the traditional single droplet experiments is related to the experimental arrangement. When applying Eqs. (2.20) and (2.25), it is important that the concentrations used are the valid concentrations for the mass transfer process under consideration. As recognized in the literature (for example, see Clift et al., 2013), the droplet life is divided into stages:

1. Formation
2. Release and acceleration to the terminal velocity
3. Steady rise at terminal velocity
4. Coalescence in the sample collection unit

Usually, the measured concentrations are the feed concentration and the concentration of the collected sample of droplets. Feed concentration is used as the inlet concentration c_{in} , and the collected sample is used as the outlet concentration c_{out} . Using a good experimental arrangement, the effect of the coalescence stage (stage 4) can be minimized so that the sample analyzed corresponds to the concentration in the column top before coalescence. The effects of stages 1 and 2 on the mass transfer can be substantial (Licht and Conway, 1950; Licht and Pansing, 1953; Liang and Slater, 1990; Wegener et al., 2014) and has to be taken into account by a suitable experimental arrangement where the length of the column L_c (=different droplet rise time Δt_R) is adjusted, and by extrapolation to the zero-length column, the effects of the formation and release stages can be determined indirectly. The principle is shown in Figure 2.5.

One solution to overcome these difficulties would be the measurement of concentration directly from droplets. First, the experimental arrangement of the collection stage can be simpler because the concentration can be measured directly at the top of the column before coalescence. Second, the effect of the droplet formation step is determined without different droplet rise times and additional measurements is not required thus speeding up the experimental work. Third, using the direct concentration measurement gives access to the concentration distribution inside the droplet. In the traditional single droplet experiment, the droplet properties are always averages of several droplets. The direct concentration measurement provides the properties of a single droplet.

Another advantage is the possibility to see how the solute is distributed inside the droplet, and this provides a better possibility of determining detailed mass transfer

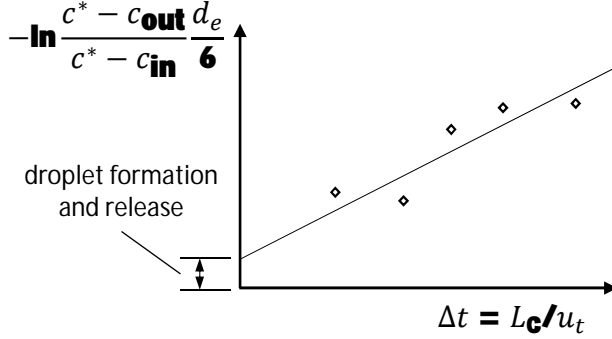


Figure 2.5: Principle to determine the effect of formation and release stages on the mass transfer in single droplet experiments. \diamond , $-\ln[(c^* - c_{\text{out}})/(c^* - c_{\text{in}})]d_e/6$ plotted at different droplet rise times Δt_R ; u_t , droplet velocity; L_C , column length; —, Eq. (2.25) fitted to experiments. \bar{K}_d is the slope of the line.

models. In the literature, the direct measurement or visualization of droplet concentration has been documented in certain cases. Schulze (2007) and Pawelski et al. (2005) have visualized concentrations inside a droplet with a suitable indicator, but the concentrations themselves are not determined. MörTERS and Bart (2000) and Baumann and Mühlfriedel (2002) performed direct measurement of tracer concentrations using laser induced fluorescence, and they determined concentration profiles near the interface. Another laser-optical measurement technique was used by Lohner et al. (2001), where light scattering provided concentration profiles inside and outside of a droplet.

2.3.2 Mass transfer to droplets

Mass transfer during dissolution between a single droplet and the ambient phase is controlled by three factors: diffusion between ambient and droplet interface, mass transfer at the interface, and diffusion between the droplet interface and the droplet internals. When the film model is applied, the overall mass transfer resistance R_{tot} is a combination of all three factors (Ferreira et al., 2010):

$$R_{\text{tot}} = R_c + R_i + R_d, \quad (2.26)$$

where R_c and R_d are diffusive resistances for the continuous and droplet sides of the interface, and R_i is the resistance provided by the interface. When resistances are expressed as mass transfer coefficients, the formula is

$$1/K_d = 1/k_d + K^*/k_c + R_i, \quad (2.27)$$

where K_d is the overall mass transfer coefficient seen from the droplet side, k_d and k_c are corresponding film mass transfer coefficients for the droplet and continuous sides, and K^* is the partition coefficient between the droplet and continuous phases. Often, in the literature for regarding liquid–liquid extraction, the selected chemical system is

determined so that either of the diffusive resistances in Eq. (2.26) is negligible when compared with another resistance.

Droplet formation

Mass transfer during droplet formation is transient, and most of the empirical models are functions of droplet Fourier number Fo_d (Popovich et al., 1964; Walia and Vir, 1976a,b; Heideger and Wright, 1986):

$$Fo_d = \frac{4\mathcal{D}_m t_F}{d_e^2}, \quad (2.28)$$

where t_F is the droplet formation time, and d_e is the volume equivalent spherical droplet diameter. Often, the models assume pure diffusion inside the droplet, but in many cases, this is not a valid assumption. This has been handled by Liang and Slater (1990) by application of the concept of effective diffusivity to take into consideration the droplet internal hydrodynamics and surface mobility affecting the mass transfer. The expression for effective diffusivity is

$$\mathcal{D}_{F,\text{eff}} = k_{H,F}(\mathcal{D}_m + \mathcal{D}_{F,E}), \quad (2.29)$$

where $\mathcal{D}_{F,E}$ is eddy diffusivity to describe the effect of droplet circulation on the mass transfer (see Handlos and Baron, 1957; Liang and Slater, 1990 and Altunok et al., 2012), and $k_{H,F}$ is an empirical parameter to take into account the effect of surfactants on the surface mobility. Liang and Slater (1990) also proposed a criterion for droplet formation hydrodynamics based on the needle Reynolds number. This allows making a conclusion whether the velocity field inside the droplet is circulatory or not.

Popovich et al. (1964) proposed an empirical model for the amount of Δn extracted during a droplet formation

$$\Delta n = a_1(c_d^* - c_{d,0}) \frac{1}{2} \sqrt{\pi Fo_d} d_e^3, \quad (2.30)$$

where a_1 is an empirical coefficient. The model developed by Walia and Vir (1976a,b) for the extraction ratio $E = (c_d - c_{d,0}) / (c_d^* - c_{d,0})$ is

$$E = f(E_d), \quad (2.31)$$

where $f(E_d)$ takes into account the boundary curvature, flow outside the droplet, and concentration changes near the interface outside the droplet (Liang and Slater, 1990). E_d is for a droplet that has a constant concentration. For the transient concentration, the extraction ratio is a polynomial function

$$E = f(E_d) = E_d - \frac{7}{8} E_d^2 - \frac{49}{72} E_d^3 - 0.476 E_d^4. \quad (2.32)$$

The expression for E_d by Liang and Slater (1990) is

$$E_d = \frac{36}{\sqrt{21}\pi} \frac{1}{2} \sqrt{Fo'_d} \left(1 + \frac{1}{2} \sqrt{Fo'_d} \right), \quad (2.33)$$

where Fo'_d is the modified droplet Fourier number having the molecular diffusivity \mathcal{D}_m replaced with the effective diffusivity $\mathcal{D}_{\text{F,eff}}$, Eq. (2.29). The average overall mass transfer coefficient in formation is

$$K_{d,F} = -\ln [(c_d^* - c_d)/(c_d^* - c_{d,0})] \frac{d_e}{6t_R}. \quad (2.34)$$

Droplet rise

Correlations for droplet rise are given separately to the continuous phase and droplet phase. For the continuous phase, correlations are given as functions of Sherwood number

$$Sh_c = f(\text{Re}, Sc_c, \kappa), \quad (2.35)$$

where κ is the ratio between the viscosities of the droplet and continuous phases. The droplet phase correlations are based on the Newman (1931) model of the solution of sphere diffusion equation and the model implies that the droplet has no internal circulation. Several approaches to taking the circulation into account can be found in the literature (see Table 2.2).

Table 2.2: Models to take into account the effect of droplet circulation and contamination on mass transfer during a droplet rise

Model	Explanation	Reference
Effective diffusivity \mathcal{D}_{eff}	Assumption of laminar flow inside the droplet, molecular diffusivity multiplied with a constant	Kronig and Brink (1951)
Eddy diffusivity \mathcal{D}_E	Assumption of turbulent flow regime inside the droplet, function of droplet terminal velocity, diameter, and viscosity ratio	Handlos and Baron (1957); Altunok et al. (2012)
Stagnant cap model	Assumption of two different hydrodynamic zones: one with pure diffusion, and another with circulation. Effective diffusivity calculated as a function of molecular diffusivity \mathcal{D}_m and eddy diffusivity \mathcal{D}_E	Slater (1995)

A mass transfer model for an internally non-circulating droplet was first formulated by Newman (1931). The solution is a closed form solution of the diffusion equation inside a sphere. The model assumes that the mass transfer resistance is mainly on the droplet side, and the effect of internal circulation is taken into account using effective diffusivity \mathcal{D}_{eff} (Kronig and Brink, 1951) or eddy diffusivity \mathcal{D}_E (Handlos and Baron, 1957; Altunok et al., 2012).

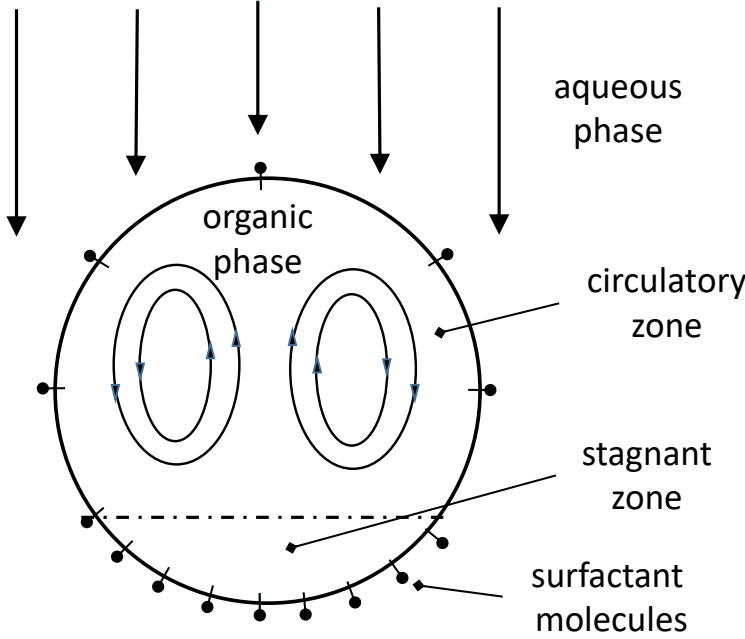


Figure 2.6: Description of the stagnant cap model of a rising droplet. Arrows describe the flow relative to the droplet.

By applying a stagnant cap model based on Savic's (1953) ideas, Slater (1995) has formulated a model for a system where surfactants hinder the mass transfer. In the stagnant cap model, it is assumed that due to hydrodynamics, the droplet becomes divided into two zones (see Figure 2.6). At the interface, due to surface flow, the distribution of surfactants is not uniform. Surfactants have a tendency to become enriched at the droplet bottom, near the wake (Slater, 1995). Correspondingly, on the top there are less surfactants. Due to this, the interface mobility is hindered more near the bottom of the droplet. The stagnant cap model assumes circulation in the droplet upper region and pure diffusion in the bottom region (stagnant zone). Slater (1995) formulated an empirical model where the Newman model is enhanced by using an overall effective diffusivity $\mathcal{D}_{R,\text{eff}}$:

$$\mathcal{D}_{R,\text{eff}} = f_v \mathcal{D}_m + (1 - f_v)(\mathcal{D}_m - \mathcal{D}_{R,E}), \quad (2.36)$$

where f_v is the fraction of the stagnant zone, and \mathcal{D}_m and $\mathcal{D}_{R,E}$ are molecular and eddy diffusivities. Mass transfer is solved by utilizing the Newman model where the diffusivity used is the overall effective diffusivity $\mathcal{D}_{R,\text{eff}}$. Originally, Slater (1995) determined empirically stagnant cap fractions f_v and eddy diffusivity $\mathcal{D}_{R,E}$. In this work, f_v was determined using images taken from the rising droplets. Slater (1995) used a modified Handlos and Barron (1957) method to determine the eddy diffusivity $\mathcal{D}_{R,E}$:

$$\mathcal{D}_{R,E} = \frac{k_{H,R} u_i d_e}{2048(1 + \mu_d/\mu_c)}, \quad (2.37)$$

where u_t is terminal velocity and μ_d and μ_c are, respectively, droplet and continuous phase viscosities. The coefficient $k_{H,R}$ takes into account the effect of contamination and surfactants on the interface mobility. It is an empirically determinable parameter in Slater's method.

2.3.3 Mass transfer with interface reaction

When there is an interface reaction, as with solvent extraction of metals from aqueous solutions into organic solvent, the interface reaction itself provides an additional resistance for the mass transfer. The expression for the interface mass transfer resistance R_i can be found in some special cases. For example, for a heterogeneous equilibrium reaction, the expression is (Bart and Stevens, 2004)

$$R_i = \frac{1}{k_R^+} \left[\frac{c_{d,i}^* - c_{d,i}}{(c_{d,i}^*)^n - (c_{d,i})^n} \right], \quad (2.38)$$

where k_R^+ is the forward reaction rate constant, n is the reaction rate order, $c_{d,i}$ is the droplet side solute concentration on the interface, $c_{d,i}^* = K^* c_{c,i}$ where $c_{c,i}$ is the solute concentration on the continuous side.

2.3.4 Droplet coalescence and mass transfer

There is a certain droplet size distribution in liquid–liquid contact units, which is affected by mixing (or using other means to produce smaller droplets). There is a balance between two processes: two or more smaller droplets coalesce into one large droplet, and one large droplet is broken into two or more smaller droplets. The goal is to keep droplet size as small as possible using an optimal amount of energy.

When droplets coalesce, the mass transfer area is decreased and the mass transfer rate is reduced. On the other hand, droplet coalescence is a vigorous hydrodynamical process, and it is expected to create turbulence and mixing inside the coalescing droplets and near the vicinity of the interface in the continuous phase.

In the studies from the literature, the effect of mixing during coalescence was not intensively examined directly. Several researchers have published results showing how to control the droplet coalescence rate and how the coalescence rate is affected by the mass transfer direction, for example, is it from a continuous phase to a droplet phase or vice versa (Ban et al., 2000; Chevaillier et al., 2006; Kamp and Kraume, 2014). They have reached the conclusion that coalescence times increase when the mass transfer is from the continuous to the droplet phase. Other parameters examined were droplet size, Marangoni convection due to concentrations (Wegener et al., 2014), and effect of surfactants (Mitra and Ghosh, 2007). Droplet size was found to affect droplet coalescence (Villwock et al., 2014), but Kamp and Kraume (2014) did not find a clear relationship between the droplet size and coalescence.

2.3.5 Mass transfer numerical modeling

In principle, the direct numerical simulation (DNS) method for solving transport equations provides parameters for constitutive equations like mass transfer coefficients. During droplet rise, if a droplet is smaller than the critical diameter, it maintains sphericity and can be modeled as a sphere with a constant shape and diameter. This approach has been used by Piarah et al. (2001), Wegener et al. (2009), Jeon et al. (2011), and Pawelski et al. (2013). When a droplet is deformed because the diameter is larger than the critical diameter, interface resolving algorithms offer a method for modeling the combined effects of hydrodynamics and interface evolution on the mass transfer. Rising droplet interface tracking has been applied by, for example, Yang and Mao (2005), Deshpande and Zimmerman (2006), Kenig et al. (2011), and Wang et al. (2013), who all used the LS method. For droplet formation, LS method was used by Lu et al. (2010) and Volume-of-Fluid (VOF) by Soleymani et al. (2008).

In this work Comsol Multiphysics (COMSOL, 2017) modeling software was used to simulate mass transfer during droplet rise, droplet formation, and droplet coalescence hydrodynamics.

Mass transfer during droplet rise

It is assumed that flow is incompressible, in which case the equations for continuity and steady state momentum are

$$\nabla \cdot \mathbf{u} = 0, \quad (2.39)$$

$$\rho(\mathbf{u} \cdot \nabla)\mathbf{u} = \nabla \left\{ -p\mathbf{I} + \mu \left[\nabla\mathbf{u} + (\nabla\mathbf{u})^T \right] \right\}, \quad (2.40)$$

where \mathbf{u} is the velocity field, ρ is density, p is pressure, and \mathbf{I} is the identity matrix. The species i transient transport equation is

$$\frac{\partial c_i}{\partial t} + \nabla(\mathbf{u}c_i) - \mathcal{D}_{m,i}\nabla^2 c_i. \quad (2.41)$$

Eqs. (2.39), (2.40), and (2.41) are formulated separately for the continuous and droplet phases.

Droplet formation and coalescence hydrodynamics

The LS method was used to model droplet formation and coalescence. The method formulation is based on work by Olsson and Kreiss (2005). The continuity and momentum equations for transient incompressible flow are

$$\nabla \cdot \mathbf{u} = 0, \quad (2.42)$$

$$\rho \frac{\partial \mathbf{u}}{\partial t} + \rho(\mathbf{u} \cdot \nabla)\mathbf{u} = \nabla \left\{ -p\mathbf{I} + \mu \left[\nabla\mathbf{u} + (\nabla\mathbf{u})^T \right] \right\} + \mathbf{F}_g + \mathbf{F}_{st}, \quad (2.43)$$

where \mathbf{F}_g and \mathbf{F}_{st} are force fields due to gravitational acceleration and surface tension. The interface between the continuous and droplet phases is tracked by conservation of LS function ϕ :

$$\frac{\partial \phi}{\partial t} + \mathbf{u} \cdot \nabla \phi = \gamma \left[\varepsilon \nabla \phi - \phi(1 - \phi) \frac{\nabla \phi}{|\nabla \phi|} \right], \quad (2.44)$$

where γ is the re-initialization parameter, and ε is the interface thickness controlling parameter. Expression $\nabla \phi / |\nabla \phi|$ is the interface normal.

The LS function ϕ is defined to be a so-called signed distance function (Olsson and Kreiss, 2005), and ϕ gets values between 0 and 1 and $\phi > 0.5$ on one side of the interface and, correspondingly, $\phi < 0.5$ on the other side of the interface. The LS function ϕ is continuous and can be used to set physical properties to change continuously over the interface (Olsson and Kreiss, 2005). Details of the LS method can be found in the work by Olsson and Kreiss (2005).

Dissolution of slow release particles

3.1 Models of KCl dissolution

Six dissolution experiments were conducted with KCl particles. The experiments and corresponding treatments are listed in Table 3.1.

Table 3.1: Dissolution experiments conducted with KCl

Case	Label	Name	Treatment
1	U	unground	unground, pure KCl particles
2	G	ground	ground pure KCl particles
3	NS10	starch 10 w %	KCl particles coated with 10 w % native starch
4	NS20	starch 20 w %	KCl particles coated with 20 w % native starch
5	L10	lignin 10 w %	KCl particles coated with 10 w % lignin
6	L20	lignin 20 w %	KCl particles coated with 20 w % lignin

Three models were initially considered:

1. *Reaction rate model*: It was assumed that the particle dissolution rate dc_p/dt is analogous to first order reaction model:

$$\frac{dc_p}{dt} = -k_R c_p. \quad (3.1)$$

Using the dissolved concentration c_∞ as a state variable

$$\frac{dc_\infty}{dt} = k_R c_p. \quad (3.2)$$

2. *Gel model*: A particle is covered with a gel layer. It was assumed that the particle itself is dissolving, but the total particle size does not change. The solute has to diffuse through the gel coating. Model equations are Eqs. (2.14) and (2.15).
3. *Active surface model*: Only a certain fraction of the particle surface is active, and otherwise, it is covered with a layer that has mass transfer resistance so large

in comparison to the free surface that it can practically be regarded as a non-penetrable material. This decreases the effective mass transfer area. Model equations are (3.4) and (2.17).

In addition, a fourth model based on the active surface model was evaluated. In this model, the diffusion layer thickness is equal with the particle radius.

Particle size distributions were determined before the dissolution measurements and the $D[4,3]$ based average diameters are tabulated in Table 3.2.

Table 3.2: $D[4,3]$ mean diameters. U = unground KCl, G = ground KCl, NS10 = native starch 10 w %, NS20 = native starch 20 w %, L10 = lignin 10 w %, L20 = lignin 20 w %

Case	U	G	NS10	NS20	L10	L20
$D[4,3]$ diameter, μm	361	92	137	137	110	110

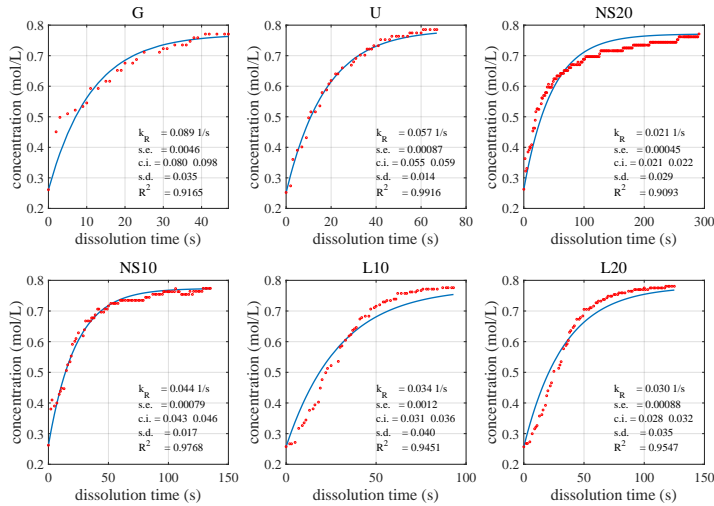


Figure 3.1: First-order reaction model: \dots , measurements; — , fitted model. Model parameters: k_R , apparent dissolution constant; $s.e.$, parameter standard error; $c.i.$, parameter 95% confidence interval; $s.d.$, standard deviation; R^2 , goodness of fit. U = unground KCl, G = ground KCl, NS10 = native starch 10 w %, NS20 = native starch 20 w %, L10 = lignin 10 w %, L20 = lignin 20 w %.

3.2 Dissolution modeling: results and discussion

3.2.1 Reaction rate model

In Figure 3.1, the results when the first-order model Eq. (3.2) was used for model dissolution are shown. Based on R^2 values, this model was able to predict dissolution well in all cases. Especially good prediction was achieved for the unground (U), ground (G), and 10 w % native starch (NS10) cases. With the dissolution of lignin-coated particles (cases L10 and L20), it can be seen that there is a phenomenon that this model cannot catch: initially, the slope of the curve is lower in comparison to the model.

k_R can be used to predict the dissolution rate between the different types of spheres. When particles were sorted according to 90% dissolution times (Table 2, Publication I), it provides the same order as if the particles are sorted from the largest to the smallest k_R (Table 4, Publication I).

Based on a material balance analysis, the constant k_R value at time t can be related to physical properties:

$$k_R(t) = \frac{A(t)k_c(t)}{V_L}. \quad (3.3)$$

Alternatively, in this case, the parameter k_R becomes averaged over the time span, so it can be regarded as a lumped parameter about the particle surface area and mass transfer coefficient, and it can produce a decent fit.

3.2.2 Constant gel radius model

The fitted model is

$$\frac{dR_p}{dt} = -\frac{e\mathcal{D}_m}{\rho_p(R_G - R_p)}(c^* - c_\infty), \quad (2.14)$$

$$\frac{dc_\infty}{dR_p} = -\frac{3c_{p,0}}{R_{p,0}^3}R_p^2, \quad (2.15)$$

where there are two parameters: e , the ratio of salt diffusivity in the gel to diffusivity in water, and R_G , the radius of the particle with a gel layer. The gel model was expected to predict the dissolution of starch-coated KCl particles. The model worked well for the experimental runs of starch (see Figure 3.2), cases NS10 and NS20. The estimated gel diameters were 141 and 170 μm , which is approximately the same as the measured average particle diameter of 137 μm . The SEM image (Figure 3.3) of 20 w % starch-coated particles reveals that the particles had a tendency to agglomerate due to the starch. The particles are round and consist of several smaller KCl particles. When compared with the SEM image for the lignin case (Figure 3.4), there is a deficiency of small sharp-edged particles.

Dissolution of unground KCl (U) was also estimated well with the constant gel radius model. The fitted parameter values were $e = 1$ and $D_{p,0} = 530 \mu\text{m}$. The value of

$e = 1$ was expected for the unground KCl particles. However, the fitted diameter value of $530 \mu\text{m}$ is quite high in comparison to the initial particle diameter of $361 \mu\text{m}$ (Table 3.2). For the ground (G) KCl, the fitted diffusivity ratio e was 0.192 and not 1, as was expected. One explanation could be the aggregation/agglomeration of fine particles during dissolution.

For the lignin cases (L10 and L20), the gel model could not provide a reasonable identification of parameters: the standard errors and the confidence intervals for both parameters were large.

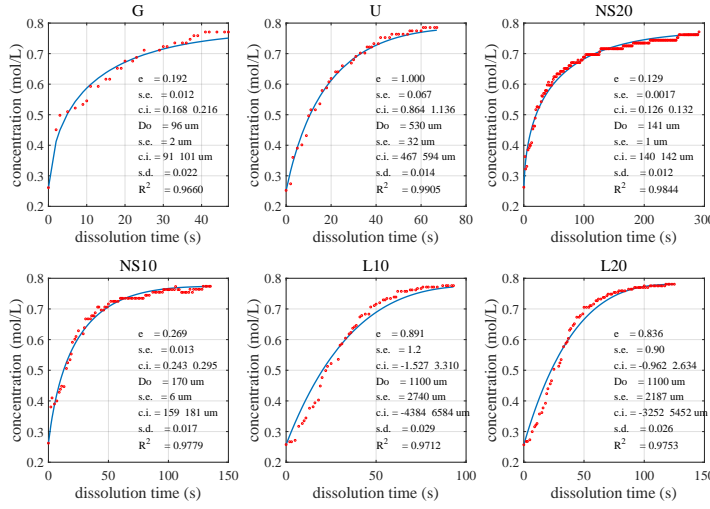


Figure 3.2: Constant gel radius model: \dots , measurements; — , fitted model. Model parameters: e , diffusivity ratio; D_0 , constant gel diameter; $s.e.$, parameter standard error; $c.i.$, parameter 95% confidence interval; $s.d.$, standard deviation; R^2 , goodness of fit. U = unground KCl, G = ground KCl, NS10 = native starch 10 w %, NS20 = native starch 20 w %, L10 = lignin 10 w %, L20 = lignin 20 w %.

3.2.3 Active surface model

The fitted model is

$$\frac{dR_p}{dt} = -\frac{ak_c}{\rho_p}(c^* - c_\infty) = -\frac{a\mathcal{D}_m}{\rho_p} \left(\frac{1}{R_p} + \frac{1}{zR_{p,0}} \right) (c^* - c_\infty), \quad (3.4)$$

$$\frac{dc_\infty}{dR_p} = -\frac{3c_{p,0}}{R_{p,0}^3} R_p^2, \quad (2.17)$$

which has two parameters: a , the active surface ratio, and $z = h/R_{p,0}$, the dimensionless diffusion layer thickness. It was assumed that with a hydrophobic coating (e.g.

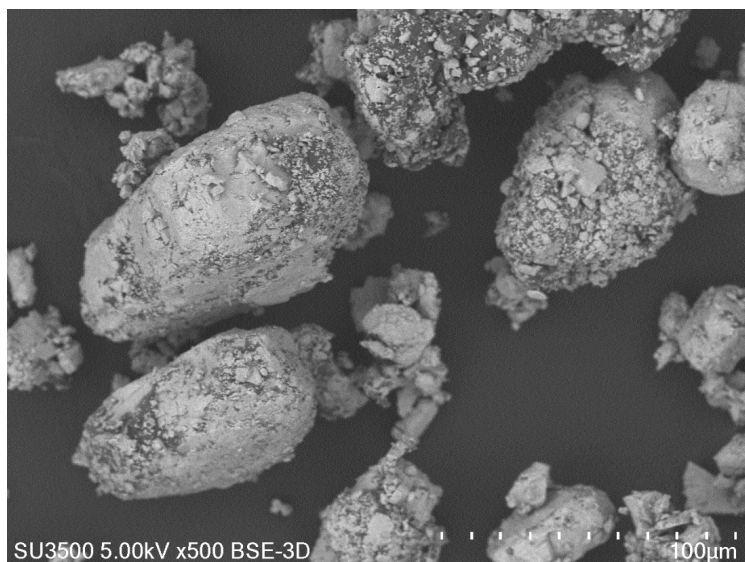


Figure 3.3: SEM image of 20 w % starch-coated KCl particles.

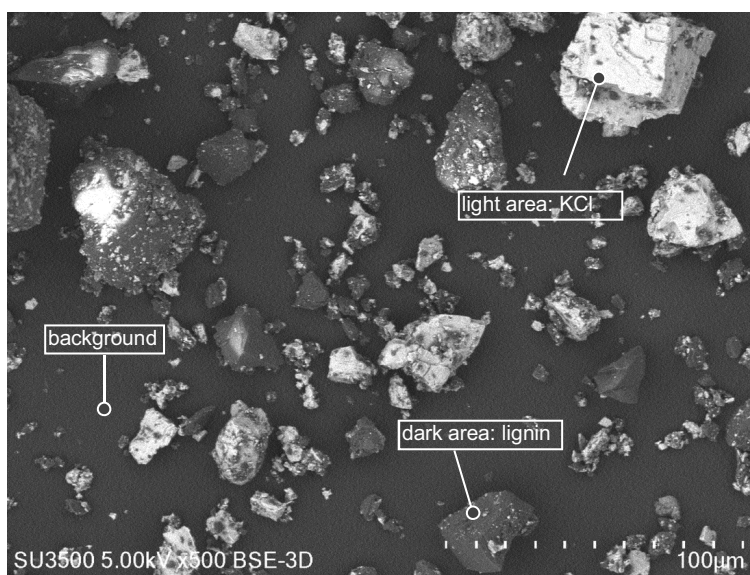


Figure 3.4: SEM image of 10 w % lignin-coated KCl particles. Dark areas (except the background) are lignin; light areas are KCl.

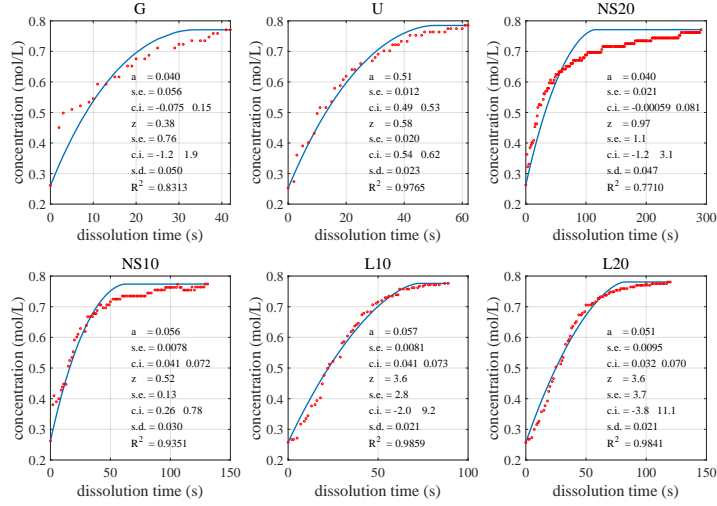


Figure 3.5: Active surface model: $\cdot\cdot\cdot$, measurements; — , fitted model. Model parameters: a , active surface ratio; z , ratio between the diffusion layer thickness h and initial sphere radius R_0 ; $s.e.$, parameter standard error; $c.i.$, parameter 95% confidence interval; $s.d.$, standard deviation; R^2 , goodness of fit. U = unground KCl, G = ground KCl, NS10 = native starch 10 w %, NS20 = native starch 20 w %, L10 = lignin 10 w %, L20 = lignin 20 w %.

(lignin), dissolution could be hindered due to the partial blanking of the sphere surface. This was confirmed by a visually good fitting of the lignin experiments (see Figure 3.5), L10 and L20. The lignin coating is also visible in the SEM image (see Figure 3.4). The fitted parameter a is approximately 6%. Another parameter, z , was 3.7 for both lignin cases. This is the same as the upper boundary given to the parameter z . For starch-coated particles, this model was not as suitable as the gel model, and the parameter errors and confidence intervals were large. However, for the unground particles (U), model fitted well and gave $a = 51\%$ and $z = h/R_{p,0} = 0.58$. For the ground particles (G), the model estimated smaller values of a and z : 0.040 and 0.38, respectively.

The statistics in Figure 3.5 reveal, that the parameters a and $z = h/R_{p,0}$ were not identified well except for the unground (U) case. This model was expected to work for the lignin-coated particles L10 and L20, but the parameter errors were high and the model validity can be suspected.

3.2.4 Active surface model having diffusion layer thickness equal to particle radius

Wang et al. (2012) proposed that for small particles, it is valid to assume $Sh_p = 2$. This means that the apparent diffusion layer thickness $\delta = R_p$:

$$Sh_p = 2 \Rightarrow \frac{k_c 2R_p}{\mathcal{D}_m} \Rightarrow \frac{\mathcal{D}_m R_p}{\delta \mathcal{D}_m} = 1 \Rightarrow \delta = R_p.$$

Wang and Flanagan (2002) provided an expression for δ in spherical geometry:

$$\frac{1}{\delta} = \frac{1}{R_p} + \frac{1}{h}. \quad (3.5)$$

In order for $\delta = R_p$, $R_p \ll h$. Now the mass transfer coefficient can be calculated directly using $Sh_p = 2$:

$$k_c = \frac{\mathcal{D}_m}{R_p}. \quad (3.6)$$

The fitting results are shown in figure 3.6. The dissolution of lignin-coated particles

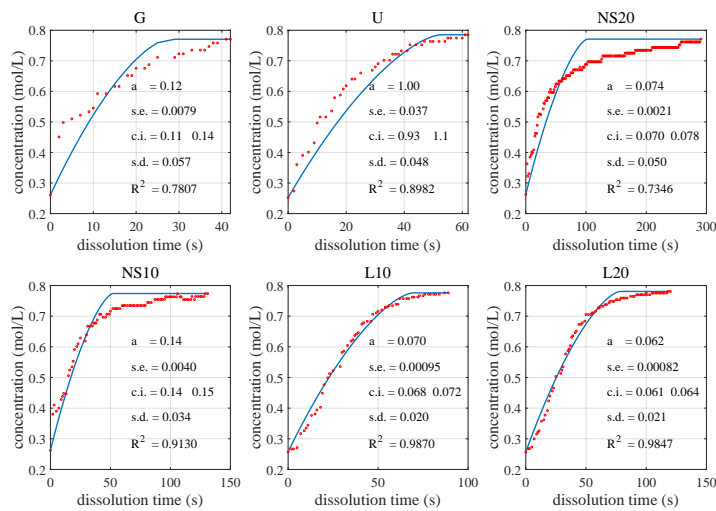


Figure 3.6: Active surface model. Sherwood number $Sh_p = 2$. \dots measurements; — fitted model. Model parameters: a , active surface ratio; $s.e.$, parameter standard error; $c.i.$, parameter 95% confidence interval; $s.d.$, standard deviation; R^2 , goodness of fit. U = unground KCl, G = ground KCl, NS10 = native starch 10 w %, NS20 = native starch 20 w %, L10 = lignin 10 w %, L20 = lignin 20 w %..

was modeled well. Only in the final 10% did the estimate have a tendency to overshoot. Starch-coated particles NS10 and NS20 did not fit well, and the gel model was better because the diffusion takes place over the gel layer, which stays constant. The unground (U) KCl was undershoot but the fitted a was 1, which was to be expected. Because the unground particles were initially large with a diameter of $361 \mu\text{m}$, then the assumption of $R_p = \delta$ cannot be valid for the whole time. For the ground particles (G), the fit was not satisfactory. This again supports the hypothesis that there is a phenomenon like aggregation/association slowing down the dissolution, which was not taken into account in the model.

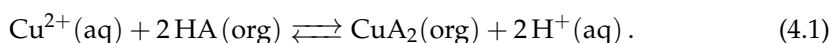
Image analysis based concentration measurement in single droplet experiments

4.1 Direct measurement: principle

The direct concentration measurement is based on the traditional method, where the transparent sample is illuminated with a suitable radiation, and intensities of the radiation are measured before and after the beam passes the sample. Based on the differences between the intensities, concentration is determined when compared with a calibration curve. The problems in this method are

1. Whether the absorbance of the solute is adequate, specifically in comparison to the other substance so that it can reliably be detected.
2. If the visible light can be used or if either IR- or UV-bands will be required.

The interface extraction reaction in this study was



The reactant HA is 5-nonyl-2-hydroxybenzaldoxime (CAS 174333-80-3), which is the active agent in Agorca M5640 commercial extraction reagent by Cytec Solvay Group. The extraction reagent was dissolved in Exxsol D80 organic diluent by Exxon.

The reactant HA exchanges Cu ions from the aqueous phase into the organic phase, producing a complex CuA_2 . This complex can be followed directly using visible light due to a color change. The spectra of the aqueous CuSO_4 solution and organic Agorca M5640 are shown in Figure 4.1. The camera provided the most sensitive spectra for the red channel and it can be seen that visible light can be used to detect the complex CuA_2 because the absorbance has a maximum at 600 nm wavelength, and the reactant HA has a maximum absorbance of 400 nm. This provides the possibility for a difference between the reactant and the copper complex. Using image analysis combined with the Lambert-Beer law, pixel intensities can be converted into complex CuA_2 concentrations, thus providing the distribution of complex inside the droplet.

Using this arrangement, the droplet is seen only from one direction, which raises a few difficulties:

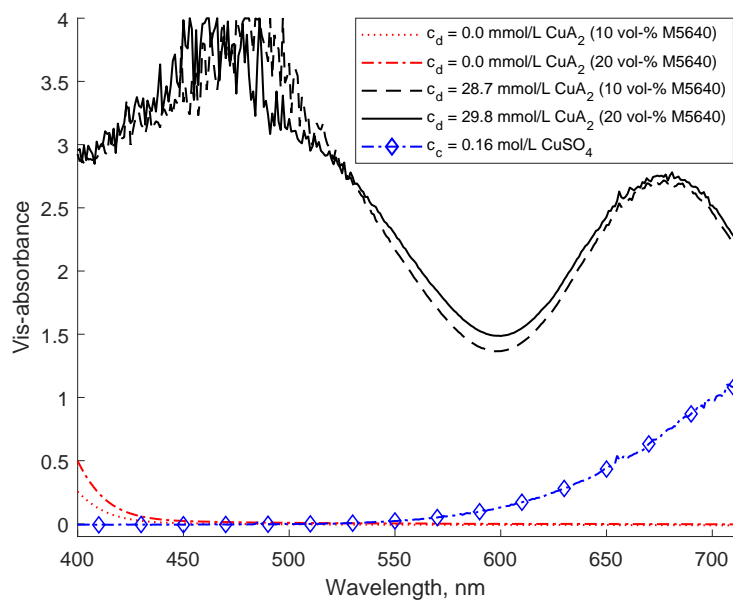


Figure 4.1: The visible range spectra of organic Acorga M5640 solutions dissolved in Exxsol D80 and aqueous CuSO_4 solution. c_d , copper complex concentration in a droplet; c_c , aqueous solution CuSO_4 concentration. The spectra is for the red channel, which was the strongest for the camera used.

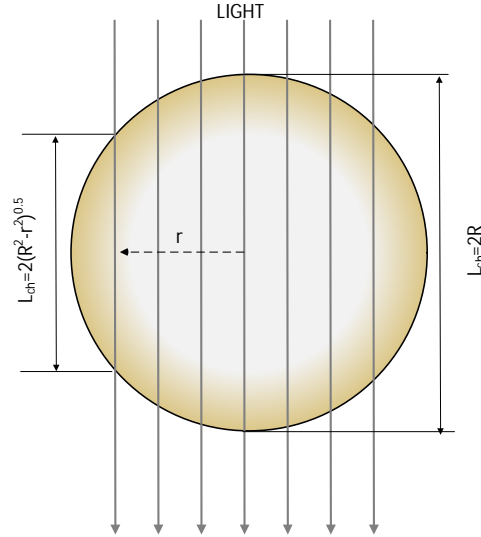


Figure 4.2: Optical path lengths L_{ch} at different distances measured from the droplet axis parallel to the light beam passing the droplet.

1. There are several layers of optically different material densities between the illuminating lamp and the camera and light refracts at each of the interfaces. Therefore, this phenomenon must be dealt with.
2. A droplet has different optical path lengths depending on the distance measured from the droplet axis parallel to light (see Figure 4.2).
3. Because light intensity is measured only in one direction, the pixel intensity reflects the total amount of complex in the direction of the light, thus not providing the concentration distribution inside the droplet.

The scattering was taken into account by determining an apparent absorptivity ε as a function of the chord length L_{ch} (Figure 4.3). Then, by applying the Lambert-Beer law, concentration at the pixel is calculated:

$$c_p = \frac{A}{\varepsilon L_{ch}}, \quad (4.2)$$

where A is absorbance.

The optical path length L_{ch} was calculated by assuming the droplet was an oblate ellipsoid.

The third item was taken into account by assuming that the complex was distributed symmetrically inside the droplet (see Figure 4.2). Then the measured absorbance reflected the concentration distribution inside the droplet.

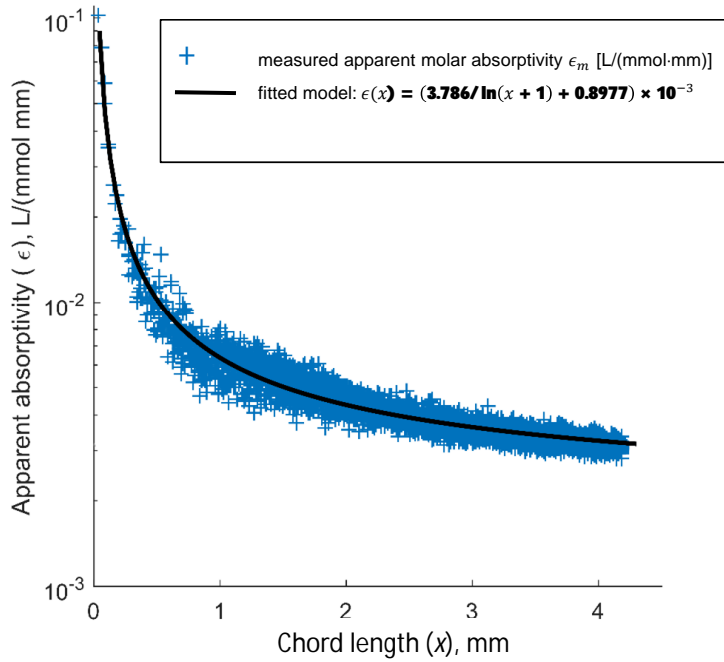


Figure 4.3: The effect of scattering due to the droplet interface curvature on molar absorptivity ϵ .

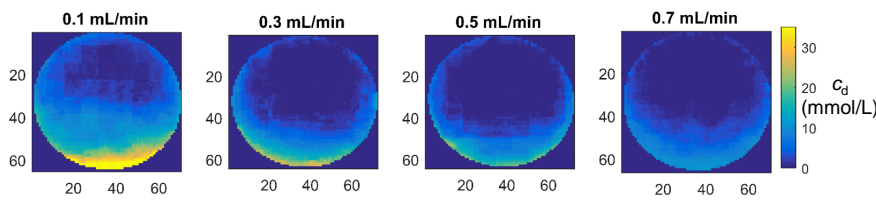


Figure 4.4: Example of determined copper complex (CuA_2) concentrations in a rising organic droplet for four organic phase feed velocities. Measurement location at the top of the column, just before coalescence. x - and y -axes, pixel coordinates; color, detected copper complex concentration c_d in the droplet (mmol/L). The color bar shows concentration scale.

4.2 Examples

An example of concentration determination is shown in Figure 4.4. It reveals that the complex had a tendency to become enriched at the droplet bottom. This can be due to the combined effect of hydrodynamics around a rising droplet and Marangoni convection. Marangoni convection is caused by the spatial change of the interfacial tension due to the concentration differences, which causes a convective downward flow along the surface. The combined effect of hydrodynamics and Marangoni convection means that the surfactants become enriched at the lower part of the droplet, thus preventing droplet internal circulation. This can be modeled with the stagnant cap model which is discussed in detail in Chapter 5.

4.3 Discussion

The developed method provides a way to get more accurate data about the mass transfer of the solute in single droplet experiments. The traditional method is based on measurement of the bulk material, and on that basis only average values are received. Conversely, this method is based on the analysis of several individual droplets, and the averages calculated from a large set of droplets is expected to better reflect the measured properties.

Mass transfer during droplet formation and rise

5.1 Mass transfer during droplet formation

Traditionally, the models used to predict mass transfer during droplet formation and rise are either purely empirical or semi-empirical based on simplified mechanistic models. Recently, however, due to developments in computational power and software, CFD-based methods have become popular for calculating mass transfer combined with hydrodynamics. The simplified models are often based on assumptions like assuming fully mixed conditions, and they do not take into account the effects of the ambient phase or circulation inside the droplet.

Drop formation is divided into two regimes: jet formation and low flow rate formation (Clift et al., 2013, pp. 657–659). The flow rate should be high enough to cause continuous jet formation. At sufficiently low flow rates, separate drops are formed. In this work, drop formation was assumed to take place with low flow rate mechanism.

The hydrodynamics during droplet formation has a tremendous effect on the conditions inside a droplet. Clift et al. (2013) make a distinction between *slow formation*, where there is no internal circulation, and *fast formation*, where the momentum of the inflow generates circulation inside a droplet. Clift et al. (2013) have provided correlations for average mass transfer coefficients of both formation types using droplet formation time t_F and droplet area $A_{d,F}$ after formation.

Popovich et al. (1964) presented a model in terms of the total mass transfer Δn during droplet formation as a function of the droplet Fourier number Fo_d :

$$\Delta n = a_1(c_d^* - c_{d,0})\frac{1}{2}\sqrt{\pi Fo_d}d_e^3, \quad (5.1)$$

where c_d^* is equilibrium concentration in a droplet, $c_{d,0}$ is the initial droplet concentration, and t_F is the formation time of a spherical droplet having volume equivalent diameter d_e . This model assumes that mass transfer is purely diffusion-controlled; interfacial instabilities and droplet internal circulation are not considered. According to Wegener et al. (2014), the constant a_1 varies between 0.857 and 3.45 for pure systems. Figure 5.1 show plotting of the experimental and estimated cumulative molar mass transport Δn as a function of $\sqrt{Fo_d}$. The estimated value of constant a_1 was 0.35 for

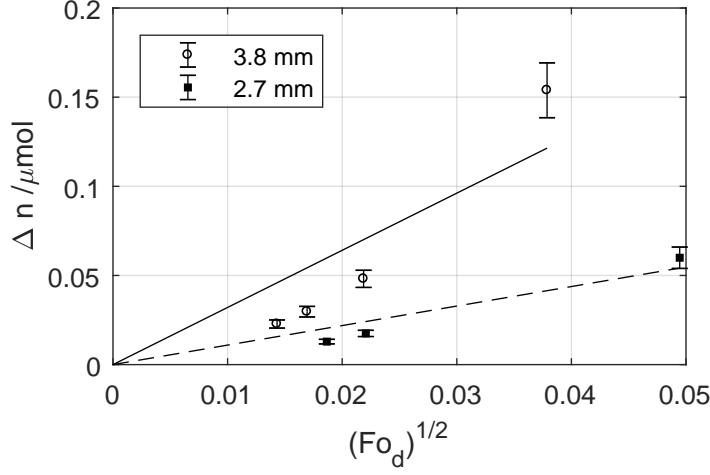


Figure 5.1: Measured and estimated cumulative mass transfer Δn against square root of droplet Fourier number. Symbols: experimental values. Estimation using the Popovich et al. (1964) model (Eq. 5.1): — 3.8 mm, - - 2.7 mm. R^2 values: 0.59 for 3.8 mm and 0.84 for 2.7 mm droplets.

both droplet sizes and 95% confidence limits for a_1 were 0.14 and 0.55. These are lower than the values proposed by Wegener et al. (2014), and it is reasonable to assume that in this chemical system, interface phenomena have a substantial effect on the mass transfer.

Walia and Vir (1976a,b) formulated a model based on the solution of the diffusion equation to model mass transfer during droplet formation using extraction ratio E as a measure of the transported amount:

$$E = E_d - \frac{7}{8}E_d^2 - \frac{49}{72}E_d^3 - 0.476E_d^4, \quad (5.2)$$

where E_d is the extraction ratio assuming negligible droplet concentration change:

$$E_d = \frac{36}{\sqrt{21}\pi} \frac{1}{2} \sqrt{Fo_d} \left(1 + \frac{1}{2} \sqrt{Fo_d} \right). \quad (5.3)$$

To also take into account droplet internal circulation and interface effects, a model proposed by Liang and Slater (1990) was used in which the pseudo-eddy diffusivity $\mathcal{D}_{F,E}$ is combined with the molecular diffusivity \mathcal{D}_m and then multiplied by a coefficient to take into account the interface effects when formulating an overall effective diffusivity $\mathcal{D}_{F,eff}$ during droplet formation:

$$\mathcal{D}_{F,eff} = k_{H,F}(\mathcal{D}_m + \mathcal{D}_{F,E}). \quad (5.4)$$

The coefficient $k_{H,F}$ function is to include the interfacial effects that can slow down the mass transfer between the droplet and continuous phases. A modified Fourier number

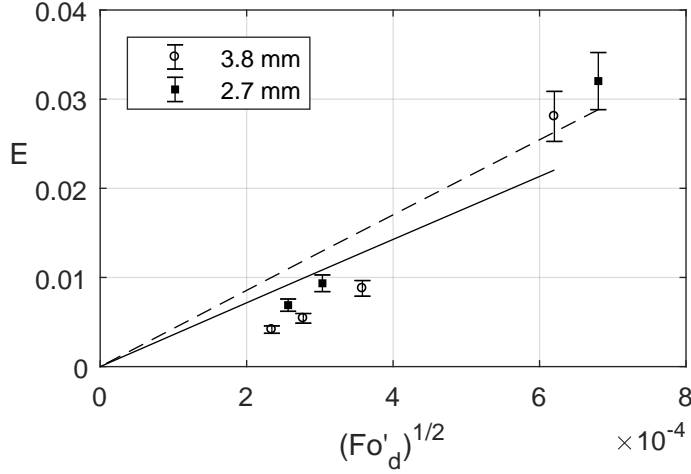


Figure 5.2: Measured and estimated extraction ratio E vs. square root of droplet modified Fourier number Fo'_d . Symbols: experimental values. Estimation using the Walia and Vir (1976a,b) model enhanced with Liang and Slater (1990) (Eqs. (5.2)–(5.5)): — 3.8 mm, – – 2.7 mm. Correction factor $k_{H,F}$ due to surface mobility is $\simeq 0.07$ for both droplet diameters.

Fo'_d is used to evaluate E_d :

$$Fo'_d = \frac{4\mathcal{D}_{F,eff}t_F}{d_p^2}. \quad (5.5)$$

Figure 5.2 plots the experimental and estimated extraction ratio E using Eqs. (5.2)–(5.5). The estimated value of the surface mobility parameter $k_{H,F}$ was $\simeq 0.07$, signaling a markedly stagnant interface. The calculation of the pseudo-eddy diffusivity $\mathcal{D}_{F,E}$ was relied on the assumption that there was no circulation inside the droplet during formation. This was based on the criteria proposed by Liang and Slater (1990), who claimed that formation is purely diffusion-based (meaning no circulation) if the needle Reynolds number Re_N is less than 35. In the present experiments, this condition was satisfied with all feed rates. In addition, the formation was modeled with CFD using the LS method to track the interface between the droplet and ambient continuous phases during formation. This also supported the conclusion that formation takes place without circulation (Figure 5.3). With large contact angles, however, the simulation gave a non-circulating velocity profile during droplet formation. With a small contact angle, the formation had a tendency to have a circulating velocity profile inside the droplet. In this study, the measured contact angle was $\simeq 120^\circ$.

In Figures 5.1 and 5.2, experimental points having the largest Fourier number, meaning the lowest organic feed rate through the needle, did not fit well with this model. One explanation is that with low feed velocities (meaning longer formation times), there is more time for the reactant HA to diffuse to the interface, and the overall mass transfer rate is greater than in the experiments with higher feed velocities corresponding smaller Fourier numbers and shorter formation times.

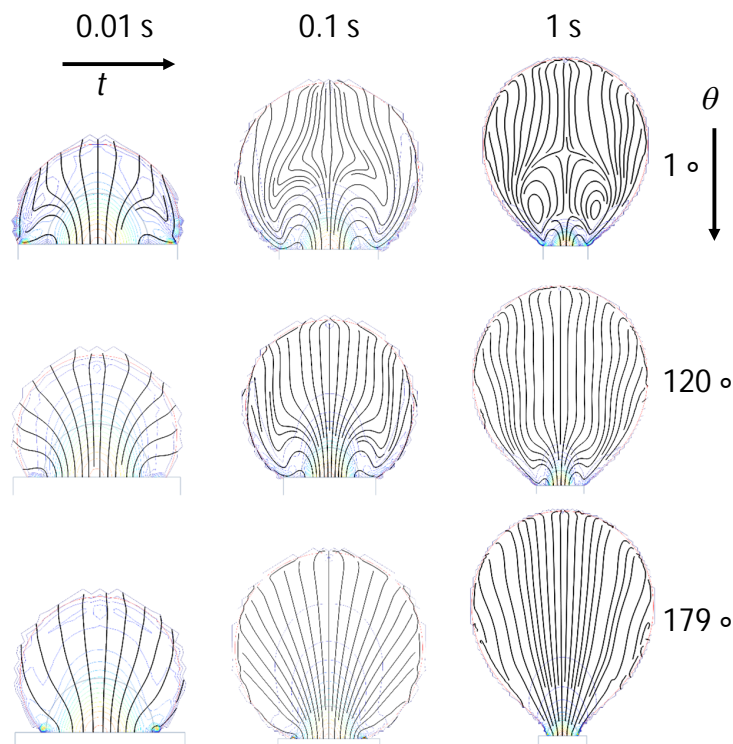


Figure 5.3: Simulated velocity profiles during droplet formation using different contact angles. Feed rate was 1 mL/min, and needle diameter 0.8 mm.

5.2 Mass transfer during droplet rise

Mass transfer during droplet rise takes place in a different environment than during droplet formation. During formation, the droplet volume and geometry are changing, but during the rise, droplet geometry is not changed after the initial release and acceleration stage, provided the droplet's diameter is smaller than a critical diameter (Wegener et al., 2014).

Mass transfer correlations for the droplet rise exist (Kumar and Hartland, 1999), but they are determined in chemical systems without contamination and surfactants. Therefore, they have limited applicability for systems where industrial grade chemicals are used.

Mass transfer between a droplet and continuous phase is also affected by an interface reaction. The reaction can provide substantial resistance to the mass transfer. The film model can be used to estimate the proportion of the interface reaction of the total mass transfer resistance if the overall mass transfer coefficient K_d , the film coefficients k_d and k_c , and a partition coefficient K^* between the phases are known. Total mass transfer

resistance is the sum of the individual resistances,

$$R_{\text{tot}} = R_{\text{d}} + R_{\text{c}} + R_{\text{if}}, \quad (5.6)$$

and is expressed using the mass transfer coefficients

$$\frac{1}{K_{\text{d}}} = \frac{1}{k_{\text{d}}} + \frac{K^*}{k_{\text{c}}} + R_{\text{if}}, \quad (5.7)$$

where R_{if} is mass transfer resistance for the interface.

In this work, a CFD model was used to determine the interface mobility parameter during the droplet rise $k_{\text{H,R}}$ and the area-based reaction kinetic constant $k_{\text{R,A}}$. The CFD model solves transient mass transfer between the ambient aqueous phase and the rising spherical droplet when the droplet has reached the terminal velocity. In this case, the velocity profile was a steady state profile. It was assumed that the initial droplet concentrations were the concentrations after the formation. The concentrations were estimates calculated using the modified Walia–Vir model formulated in Section 5.1.

It was assumed that the interface is rigid, on average, so the interface mobility coefficient $k_{\text{H,R}}$ was approximated having value 0. This approximation was used when the boundary condition for the interfacial velocity was set. The boundary condition was a no-slip condition, signaling a pure diffusive mass transfer inside the droplet.

To set $k_{\text{H,R}}$ to 0 in the model means that the effective diffusivity $\mathcal{D}_{\text{R,eff}}$ is equal to the molecular diffusivity \mathcal{D}_{m} . However, the stagnant cap fraction f_{v} was used to set the initial concentration distribution inside the droplet. Fractions were estimated using the figures taken from the rising droplets, and the distribution resembled the stagnant cap profile.

Simulations were performed with 3.8 mm droplets. The fitted parameter was the reaction kinetic constant $k_{\text{R,A}}$. The fitting criterion was to minimize the sum of the squared differences between the measured and estimated concentrations,

$$SSQ = \min \left(\sum_{j=1}^4 (c_{\text{R,m},j} - c_{\text{R,e},j})^2 \right), \quad (5.8)$$

where $c_{\text{R,m},j}$ is the measured concentration and $c_{\text{R,e},j}$ is the CFD estimated concentration in the j -th feed flow.

The fitted value for the kinetic constant $k_{\text{R,A}}$ was $0.13 \cdot 10^{-6} \text{ dm}^4/\text{mol s}$. Tamminen et al. (2013) determined experimentally in a high shear reactor the kinetic constant $k_{\text{R,A}}^0 = 1.4 \cdot 10^{-3} \text{ dm}^4/\text{mol s}$. This value is much larger than the fitted value $k_{\text{R,A}}$. The obvious reason for the large difference between the values of kinetic constants $k_{\text{R,A}}^0$ and $k_{\text{R,A}}$ is the totally different hydrodynamic conditions. Tamminen et al. (2013) performed experiments in a high shear reactor, where the emulsion was mixed vigorously, the interface between the phases was continuously renewed, and mass transfer between the interface and bulk of a phase did not contribute a significant mass transfer resistance. In single droplet experiments, the interface did not experience any violent mixing and was not renewed. Instead, the active extractant in Agorca had a possibility

to adsorb on the interface, which effectively slowed down the mass transfer between the continuous and droplet phases. Also, the mass transfer diffusion layer thickness increased and provided an additional mass transfer resistance. The kinetic constant $k_{R,A}$ represents the combined effect of the diffusive mass transfer and the interfacial reaction.

Mass transfer coefficients were estimated using three methods: (1) calculation of the coefficients directly from CFD results, (2) using the Newman model for the droplet side mass transfer film coefficient k_d , and (3) the continuous side film coefficient k_c using a correlation for stagnant droplets, as proposed by Kumar and Hartland (1999):

$$\text{Sh}_c = 1 + 0.724\text{Re}^{0.48}\text{Sc}_c^{1/3}, \quad (5.9)$$

$$100 < \text{Re} < 2000 \text{ and } \text{Sc}_c > 200.$$

The estimated mass transfer coefficients are given in Table 5.1. For the droplet side, the Newman and CFD models gave the same value for the estimated mass transfer coefficient. This was to be expected because the Newman model is a pure diffusion solution for a spherical droplet, and when the interface was assumed to be rigid, the CFD model provided also a solution of pure diffusion. The Newman solution, however, assumes that the concentration field is homogeneous. In the CFD model, concentrations had an initial distribution that was calculated based on the stagnant cap model and the observed distributions. The continuous side film coefficient k_c was slightly smaller

Table 5.1: Estimated and measured mass transfer coefficients for the droplet rise

	K_d 10^{-6} m s^{-1}	k_c 10^{-6} m s^{-1}	k_d 10^{-6} m s^{-1}
Newman			13
Kumar and Hartland, Eq. (5.9)		28	
CFD model	0.7	34	13
Measurement	0.7		

than provided by the Kumar and Hartland correlation, Eq. (5.9), as compared to the CFD model, but the difference was not large. So the selected CFD model has certain empirical support from the literature.

The total mass transfer coefficient calculated from Eq. (2.25) using estimated formation concentrations and measured concentrations after droplet rise gave $K_d = 0.7 \cdot 10^{-6} \text{ m/s}$, with standard deviation $s = 0.6 \cdot 10^{-6} \text{ m/s}$. The estimated K_d from the experiments and those calculated using the CFD model were equal.

When the film model (Eqs. 5.6 and 5.7) was used to estimate mass transfer resistances, the continuous side resistance was 2%, and the droplet side was 5%. The remaining resistance for the interface was 93%. This is a high value when the mass transfer kinetics was assumed to be diffusion controlled (Feiser, 1988). However, using the same chemical system, Ferreira et al. (2010) determined similar resistances. For the continuous phase, resistances were between 2 and 10%, for the droplet phase between 2 and 4%, and for the interface between 85 and 96%.

It was recognized that the calculation mesh near the droplet interface has to be dense enough to compensate for the numerical error produced by modeling a simultaneous convection and crosswind diffusion. The cell Peclet number used to characterize the solution stability was

$$\text{Pe}_{\text{cell}} = \frac{u_{\text{cell}} L_{\text{cell}}}{\mathcal{D}}, \quad (5.10)$$

where u_{cell} is velocity in the cell, L_{cell} is the cell dimension, and \mathcal{D} is diffusivity. Without special numerical stabilization procedures, the solution is oscillatory when $\text{Pe}_{\text{cell}} > 1$ (Zienkiewicz et al., 2005, p. 32). In this study, the ratio $u_{\text{cell}}/\mathcal{D}$ had a magnitude of 10^8 , and the minimum L_{cell} was $0.8 \mu\text{m}$. The Pe_{cell} in the vicinity of the phase interface had a magnitude of 10^2 . Even with the $\text{Pe}_{\text{cell}} \gg 1$, the solution is convergent and was no longer sensitive to mesh density (see Table 6, Publication III).

Also, the requirement for dense mesh can be physically justified based on the droplet Schmidt number, which was more than 1,000. When the Schmidt number is large, it means the viscous forces are dominating in the boundary layer and the physical mass transfer layer becomes very thin, which requires a dense mesh to be accurately modeled.

Mass transfer during droplet coalescence

6.1 Coalescence experiments

A special coalescence cell (see Figure 6.1) was constructed where droplets were formed on the tips of two opposite needles. Droplets were allowed to coalesce, and the process was recorded by a video camera. The video was analyzed to determine the concentrations of droplets before, during, and after coalescence.

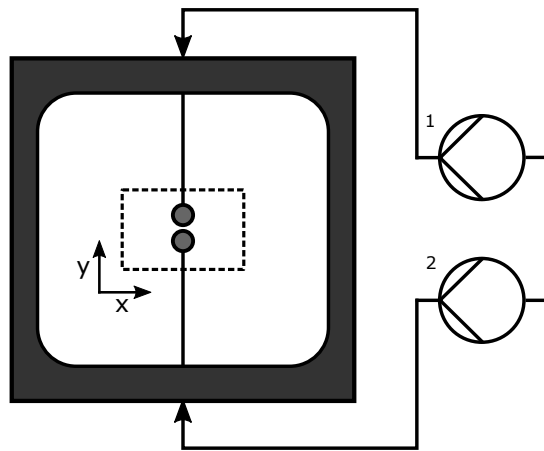


Figure 6.1: Experimental setup for the coalescence experiments. A camera and a LED panel for back-illumination were placed on opposite sides of the cell. The pendant and sessile droplets were formed on the needle tips using syringe pumps (marked 1 and 2). Inner dimensions of the cell were $50 \times 50 \times 40$ mm. The dashed line indicates the approximate field of view of the camera. The x - and y -axes are marked, and the z -axis is perpendicular to the image plane.

Two sets of coalescence experiments were performed. The chemical system was the same as in the single droplet experiments (Chapters 4 and 5). The first set consisted

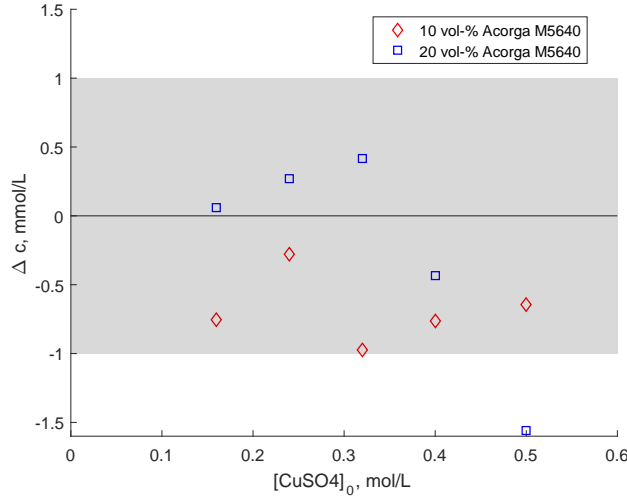


Figure 6.2: Concentration difference Δc (mmol/L) in the droplet coalescence experiments with varying CuSO_4 concentrations in the aqueous continuous phase. 10 vol % and 20 vol % reagent concentrations were used in droplets. The shaded area shows the reproducibility of the analysis method (Tamminen et al., 2017).

of experiments without mass transfer between the droplets and continuous phases. The purpose was to provide a reference set to be compared with the coalescence having mass transfer. The continuous aqueous phase was an $(\text{NH}_4)_2\text{SO}_4$ solution. In the second set, with mass transfer, the continuous aqueous phase was a CuSO_4 solution.

6.1.1 Mass transfer during droplet coalescence

Coalescence experiments were performed using two different organic droplet concentrations: 10 vol % and 20 vol % Acorga M5640. The aqueous continuous phase CuSO_4 concentration was varied between 0.16 and 0.5 mol/L. Droplet copper concentrations were measured just before and after coalescence. For each coalescence experiment, the concentration difference Δc was calculated from the measurements using the following formula:

$$\Delta c = c_{\text{coal}} - \frac{n_S + n_P}{V_S + V_P}, \quad (6.1)$$

where c_{coal} is the coalesced droplet concentration, n_S and n_P are moles of copper in the sessile and pendant droplets, respectively, and V_P and V_S corresponded to droplet volumes. Concentration difference Δc was used as a criteria for evaluating the amount of mass transfer during the coalescence process.

Concentration differences are shown in Figure 6.2. Based on these results, coalescence does not have any enhancing effect on the coalescence. The change in concentrations

was even smaller than the detection limit.

6.1.2 Droplet rest time distribution

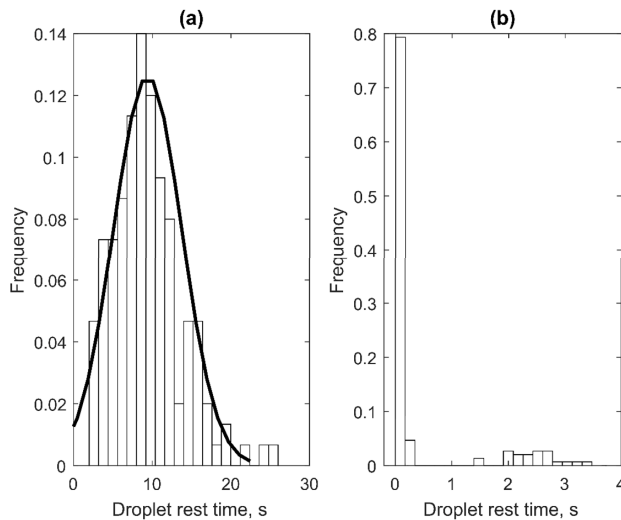


Figure 6.3: The experimental binary organic droplet rest time distributions. The continuous phase ($c_c = 0.16$ mol/L) was aqueous $(\text{NH}_4)_2\text{SO}_4$ (a) or CuSO_4 solution (b). $x_{\text{HA}} = 20$ vol% Acorga M5640. For (a), the rest time distribution obeys normal distribution. For (b), there are two distributions having short and long rest times. The average rest time for short was ≈ 0.5 s and for long, ≈ 3 s. The number of measurements was 150.

Droplet rest time t_r is the time passed after two droplets contact and before the coalescence occurs. The observed rest time distributions are plotted in Figure 6.3. On the left, (a), is the distribution without mass transfer, and on the right, (b), is the distribution when there was mass transfer. It can be seen that mass transfer has an effect by decreasing the rest time. In addition, when mass transfer takes place, there were two distributions for the observed rest times. The longer rest times, ≈ 2.3 s, were in the experiments where no surface flows were recognized. The shorter rest times, ≈ 0.5 s, were observed when there was surface flow. In Figure 6.4 shows an example of recognized surface flow. The surface flow effect was recognized by following the moving boundary on the droplet surface.

There was no observable effect of droplet formation time on the droplet rest time (see Figure 6.5).

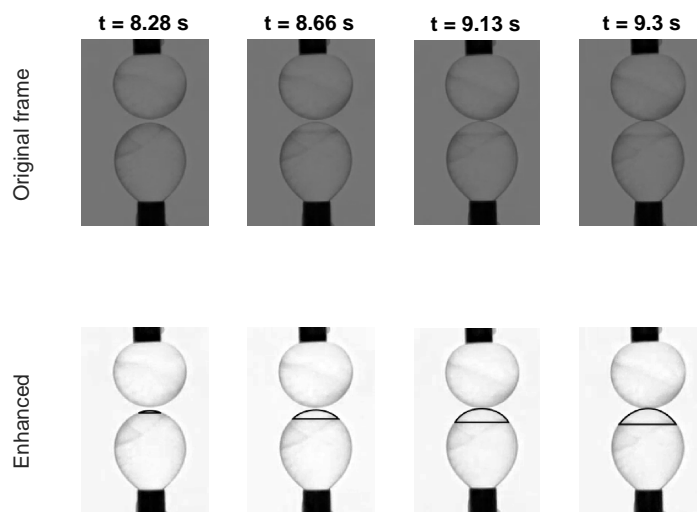


Figure 6.4: The surface flow effect leading to droplet coalescence with a short rest time ($t_r = 0.2$ s). The droplet phase concentration was 20 vol% Acorga M5640, and the continuous phase was 0.85 mol/L CuSO_4 solution. Sessile droplet formation time $t_{FS} = 3.1$ s, pendant droplet formation time $t_{FS} = 3.4$ s. The last frame of the sequence was recorded just before the coalescence. First row images show the green channel of the cropped video frame. Horizontal lines were drawn on second row images to mark the surface flow effect.

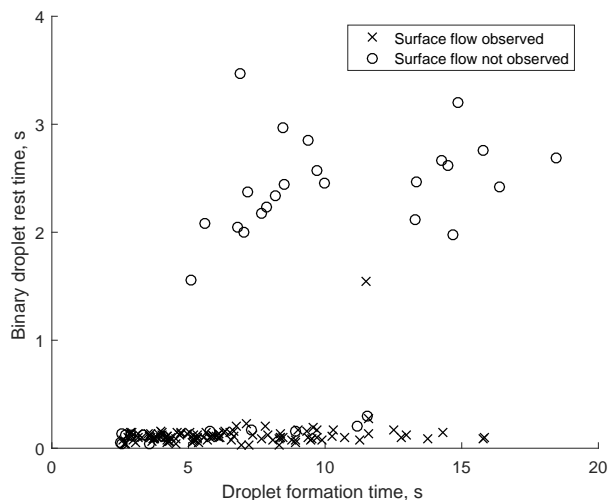


Figure 6.5: The surface flow observations. The presence of surface flow leads to shorter rest times, meaning more rapid droplet coalescence. The surface flow was made visible by the copper complex movements at the droplet interface. The surface flows were observed in pendant droplets, sessile droplets, or both droplets simultaneously. Droplet phase concentration was 20 vol % Acorga M5640, and continuous phase 0.16 mol/L CuSO_4 .

6.2 Modeling of the coalescence process

A CFD model was formulated to simulate droplet coalescence. By assuming axial symmetry, the coalescence of two droplets with equal diameters was modeled using 2D axial symmetric geometry. At the initial stage, droplets were allowed to touch each other. The geometry calculation domain and boundary conditions for the LS solver are shown in Figure 6.6.

In the model, droplet rest times were ignored, and only the actual coalescence was simulated. In the experiments, the predefined volumetric amount of solution was fed to generate the required droplet size so they would touch each other. In the model, feed was not stopped. This was observed to stabilize the calculation; without a small feed, the calculation had a tendency to diverge. The inlet feed rate was so small that it did not have any noticeable effect on the size of the droplets due to a short coalescence time.

Figure 6.7 shows the experiments and simulations. In all cases, the process was very similar, and the coalescence time was approximately 30 ms.

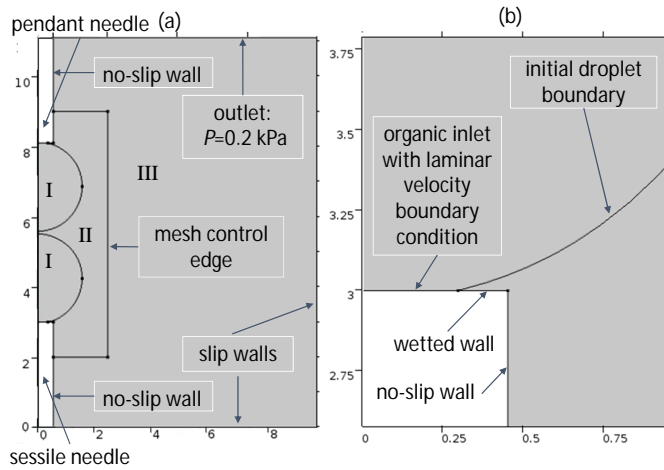


Figure 6.6: 2D axial symmetric CFD geometry and the boundary conditions. (a) shows the whole calculation domain, and (b) shows details of the needle tip. The calculation domain had a width of 10 mm and height of 11 mm. The domain bottom and side walls had free slip boundary conditions. The needle vertical sides were set to no-slip wall conditions, and the needle tip was a wetted wall. The domain top was the outlet, and the pressure was set to the hydrostatic pressure generated by the aqueous phase column on top of the calculation domain. The pressure was 0.2 kPa. The inlet flow was laminar.

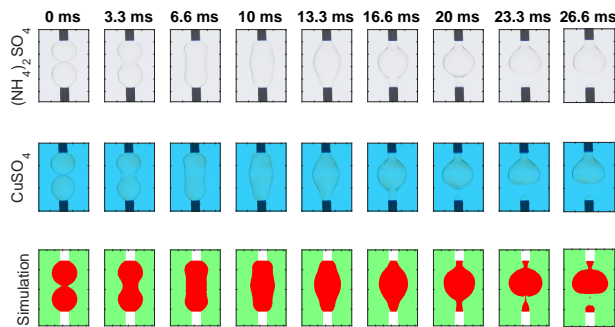


Figure 6.7: The coalescence of pendant and sessile droplets. The coalescence and combination of the droplets started from the film rupture, where the droplet interfaces of the film break. At the same time, the droplet volumes were merging together, eventually forming a new combined droplet. The images show the comparison of coalescence measurements when the continuous phase was aqueous ammonium sulfate solution (first row), and aqueous copper sulfate solution (second row) to the simulation results (third row). Droplet phase concentration was 20 vol % Acorga M5640, and continuous phase 0.16 mol/L CuSO_4 .

6.3 Discussion

6.3.1 Experimental results

Due to a short coalescence time, the mass transfer during the coalescence was not long enough to be enhanced even though vigorous mixing of the droplet and its contents were expected to take place. This is probably due to the stabilizing effect of the Agorca M5640 reagent, which is known to be a surfactant, and the stabilizing effect can be substantial. Already in the column model for single droplet experiment (see Chapter 5), a fast interfacial reaction became slower due to the different hydrodynamic conditions during single droplet experiments. In the coalescence experiments, the conditions were very similar, and it is a likely explanation for the small mass transfer rate during the coalescence step.

There was also a rest time distribution (Figure 6.3) that can be explained by the surface flow generated by the Marangoni convection. The droplet formation time seemed to have no effect on this.

Eiswirth (2014) has published results concerning mixing of droplet contents during coalescence. He observed that when the droplets were of an equal size, there was no mixing, but with varying pendant and sessile sizes, contents of the droplets were mixed. In this work, the pendant and sessile droplet sizes were equal, and no noticeable mixing was observed.

6.3.2 Modeling results

The LS method based CFD model is able to simulate the coalescence hydrodynamics. A comparison of the model with the experiments (Figure 6.7) shows that there were no significant discrepancies between the calculated and experimental droplet outlines. In addition, the time span of $\simeq 30$ ms for the total coalescence process matches well between the model and the experiments.

Conclusions and suggestions for future work

7.1 Conclusions

In this thesis, new mechanistic and empirical models were derived with the aim of describing the interfacial mass transfer process. The models can be used for product and process design related with the mass transfer phenomena in dissolution and in reactive extraction. The theoretical models were used to investigate two cases, specifically the dissolution of coated salt particles and reactive extraction using single droplet experiments.

The controlled dissolution of certain substances is an essential property of many industrial and commodity products, for example, in certain pharmaceutical and agricultural applications. Often, the controlled dissolution rate is achieved by using a suitable coating over the dissolving substance.

In this work, KCl particles were coated with two different materials, native starch and lignin. Three mechanistic models, (1) the gel model, (2) the active surface model, and (3) the active surface model assuming $Sh_p = 2$, were constructed on the basis of the mass transfer film model. The gel model was presented for dissolving the KCl particles coated with a gel layer. The active surface model using $Sh_p = 2$ was used to describe the dissolution of the KCl particles partially coated with lignin. The experimental results indicate that both models worked well in these study cases. Therefore, the models suggest a robust theoretical method for predicting mass transfer in the dissolution of coated salt particles.

Liquid-liquid extraction and, in particular, reactive extraction are important unit operations in the mineral and hydrometallurgical industries where the efficiency of separation is of crucial importance. Therefore, understanding mass transfer between phases forms a good basis for unit design. A key parameter for unit design is the determination of the mass transfer coefficient between the phases.

In this work, a new image analysis method was developed that can be used to determine changes in the droplet concentration over time. The experimental data are the basis for constructing new models to describe the mass transfer in extraction process. Reactive extraction was studied experimentally following a single droplet in a continuous phase. Using the experimental data, new models were derived with the aim of

characterizing mass transfer to a single droplet during droplet formation and rise. Furthermore, the coalescence of droplets was investigated experimentally together with a simulation model.

For the droplet formation, a new numerical model was developed to predict the velocity distribution in the droplet. The modeling result was validated by the empirical model published in the literature. Based on this velocity distribution, a new empirical model was formulated to describe the mass transfer process. The experimental results show that the model presented in the work is more accurate than one of the models published in the literature.

For the droplet rise, a new numerical model was formulated where the mass transfer and velocity field were solved by the conservation of momentum and mass. The modeling results combined with experimental results were used to predict the mass transfer coefficient for reactive extraction. The study results revealed that in reactive extraction, the mass transfer resistance is located mainly at the phase interface. The model provides a new way to design the reactive extraction process.

Mass transfer during droplet coalescence were studied experimentally using the developed image analysis method. Accordingly, the coalescence hydrodynamics and mass transfer was studied. Experimental results show that mass transfer is not enhanced due to droplet coalescence. Meanwhile, the coalescence hydrodynamics is not affected by the mass transfer. A new numerical model for the hydrodynamics of two-droplet coalescence was also formulated and validated with the experiments.

7.2 Future work

In this research, pure empirical or semi-empirical models were used to model the dissolution of coated particles. To gain a deeper understanding of the mechanism of dissolution, CFD can be applied, and as an example, the study by Kaunisto et al. (2009) could be useful for this. However, the focus in their work was the dissolution of pure particles, and the effect of coating on the dissolution should be included.

Mass transfer during droplet formation and droplet coalescence was not modeled using the conservation of mass, energy, and momentum. Instead, an empirical correlation was used to model the mass transfer during formation and droplet coalescence. Droplet formation hydrodynamics was simulated using an LS interface resolving method. In addition, a logical next step is to combine mass transfer with an interface resolving model. The same approach could be used with droplet coalescence.

Marangoni convection is an important phenomenon, but it was not separately modeled. It is assumed that the effect is lumped into the surface mobility parameters applied in the models for droplet formation and rise, together with other interface phenomena. However, Marangoni convection creates a substantial effect on the droplet surface. Inclusion of this phenomenon with numerical models requires that the concentration dependence on the interface tension is known, so there is a need for additional experimental work.

The model used during droplet rise was based on the assumption of a droplet with fixed geometry. In practice, this is not true: the droplet geometry changes after it is released from the needle and during the rise period when it is accelerating to the terminal velocity. Therefore, this will require the usage of the interface resolving method in order to catch the droplet shape.

References

- Altunok, M. Y., Kalem, M., and Pfennig, A. Investigation of mass transfer on single droplets for the reactive extraction of zinc with D2EHPA. *AIChE Journal*, 58(5): 1346–1355, 2012.
- Azeem, B., Kushaari, K., Man, Z. B., Basit, A., and Thanh, T. H. Review on materials & methods to produce controlled release coated urea fertilizer. *Journal of Controlled Release*, 181(1):11–21, 2014.
- Babaei, M., Mu, J., and Masters, A. J. Impact of variation in multicomponent diffusion coefficients and salinity in CO₂-EOR: A numerical study using molecular dynamics simulation. *Journal of Petroleum Science and Engineering*, 162:685–696, 2018.
- Ban, T., Kawaizumi, F., Nii, S., and Takahashi, K. Study of drop coalescence behavior for liquid-liquid extraction operation. *Chemical Engineering Science*, 55:5385–5391, 2000.
- Bart, H. J. and Stevens, G. W. Reactive solvent extraction. In *Ion Exchange and Solvent Extraction*, volume 17 of *A Series of Advances*, pages 37–83. CRC Press, 2004.
- Baumann, K.-H. and Mühlfriedel, K. Mass transfer studies with laser-induced fluorescence across liquid/liquid phase boundaries. *Chemical Engineering and Technology*, 25(7):697–700, 2002.
- Bird, R. B. Five decades of transport phenomena. *AIChE Journal*, 50(2):273–287, 2004.
- Biswas, R. K., Hanif, M. A., and Bari, M. F. Kinetics of forward extraction of manganese(II) from acidic chloride medium by D2EHPA in kerosene using the single drop technique. *Hydrometallurgy*, 42(3):399–409, 1996.
- Biswas, R. K., Habib, M. A., and Bari, M. F. Kinetics of backward extraction of Mn(II) from Mn-D2EHP complex in kerosene to hydrochloric acid medium using single drop technique. *Hydrometallurgy*, 46(3):349–362, 1997.
- Brunner, E. Reaktionsgeschwindigkeit in heterogenen systemen. *Z. Physik. Chem.*, 47: 56–102, 1904.
- Cardellini, A., Fasano, M., Bigdeli, M. B., Chiavazzo, E., and Asinari, P. Thermal transport phenomena in nanoparticle suspensions. *Journal of Physics Condensed Matter*, 28(48), 2016.
- Chaudhari, A. R., Gujarathi, N. A., Rane, B. R., Pawar, S. P., and Bakliwal, S. P. Novel sustained release drug delivery system: A review. *Pharma Research*, 8(1):80–97, 2012.

- Chevaillier, J.-P., Klaseboer, E., Masbernat, O., and Gourdon, C. Effect of mass transfer on the film drainage between colliding drops. *Journal of Colloid and Interface Science*, 299(1):472–485, 2006.
- Clift, R., Grace, J. R., and Weber, M. E. *Bubbles, Drops, and Particles*. Mineola, New York, USA, 2013.
- COMSOL. COMSOL Multiphysics v5.2. <http://www.comsol.com>, COMSOL AB, Stockholm, Sweden, 2017.
- Costa, P. and Lobo, J. M. S. Influence of dissolution medium agitation on release profiles of sustained-release tablets. *Drug development and industrial pharmacy*, 27(8): 811–817, 2001a.
- Costa, P. and Lobo, J. M. S. Modeling and comparison of dissolution profiles. *European Journal of Pharmaceutical Sciences*, 13(2):123–133, 2001b.
- Cussler, E. L. *Diffusion Mass Transfer in Fluid Systems*. Cambridge University Press, Cambridge, UK, 2nd edition, 1999.
- Darmana, D., Deen, N. G., and Kuipers, J. A. M. Detailed modeling of hydrodynamics, mass transfer and chemical reactions in a bubble column using a discrete bubble model. *Chemical Engineering Science*, 60(12):3383–3404, 2005.
- Darmana, D., Deen, N. G., and Kuipers, J. A. M. Detailed 3D modeling of mass transfer processes in two-phase flows with dynamic interfaces. *Chemical Engineering and Technology*, 29(9):1027–1033, 2006.
- Darmana, D., Henket, R. L. B., Deen, N. G., and Kuipers, J. A. M. Detailed modelling of hydrodynamics, mass transfer and chemical reactions in a bubble column using a discrete bubble model: Chemisorption of CO₂ into NaOH solution, numerical and experimental study. *Chemical Engineering Science*, 62(9):2556–2575, 2007.
- Darmana, D. *On the multiscale modelling of hydrodynamics, mass transfer and chemical reactions in bubble columns*. PhD thesis, University of Twente, Netherlands, 2006.
- Deen, N. G., van Sint Annaland, M., and Kuipers, J. A. M. Multi-scale modeling of dispersed gas-liquid two-phase flow. *Chemical Engineering Science*, 59(8-9): 1853–1861, 2004.
- Deshpande, K. B. and Zimmerman, W. B. Simulation of interfacial mass transfer by droplet dynamics using the level set method. *Chemical Engineering Science*, 61(19): 6486–6498, 2006.
- Di Colo, G., Baggiani, A., Zambito, Y., Mollica, G., Geppi, M., and Serafini, M. F. A new hydrogel for the extended and complete prednisolone release in the GI tract. *International Journal of Pharmaceutics*, 310(1-2):154–161, 2006.
- Eiswirth, R. T. *Binary Droplet Coalescence of Free Rising Droplets*. PhD thesis, Technischen Universität Kaiserslautern, Kaiserslautern, Germany, 2014.
- Eiswirth, R. T., Bart, H.-J., Atmakidis, T., and Kenig, E. Y. Experimental and numerical

- investigation of a free rising droplet. *Chemical Engineering and Processing: Process Intensification*, 50(7):718–727, 2011.
- Ferreira, A. E., Agarwal, S., Machado, R. M., Gameiro, M. L., Santos, S., Reis, M. T., Ismael, M. R., Correia, M. J., and Carvalho, J. M. R. Extraction of copper from acidic leach solution with Acorga M5640 using a pulsed sieve plate column. *Hydrometallurgy*, 104(1):66–75, 2010.
- Freiser, H. Role of the interface in solvent extraction processes. *Bulletin of the Chemical Society of Japan*, 61(1):39–45, 1988.
- Han, X., Chen, S., and Hu, X. Controlled-release fertilizer encapsulated by starch/polyvinyl alcohol coating. *Desalination*, 240(1–3):21–26, 2009.
- Hanafi, M. M., Eltaib, S. M., and Ahmad, M. B. Physical and chemical characteristics of controlled release compound fertiliser. *European Polymer Journal*, 36(10): 2081–2088, 2000.
- Handlos, A. E. and Baron, T. Mass and heat transfer from drops in liquid-liquid extraction. *AIChE Journal*, 3(1):127–136, 1957.
- Heideger, W. J. and Wright, M. W. Liquid extraction during drop formation: Effect of formation time. *AIChE Journal*, 32(8):1372–1376, 1986.
- Henschke, M. and Pfennig, A. Mass-transfer enhancement in single-drop extraction experiments. *AIChE Journal*, 45(10):2079–2086, 1999.
- Higuchi, T. Mechanism of sustained-action medication. Theoretical analysis of rate of release of solid drugs dispersed in solid matrices. *Journal of Pharmaceutical Sciences*, 52(12):1145–1149, 1963.
- Higuchi, T. Rate of release of medicaments from ointment bases containing drugs in suspension. *Journal of Pharmaceutical Sciences*, 50(10):874–875, 1961.
- Higuchi, W. I. and Hiestand, E. N. Dissolution rates of finely divided drug powders I. Effect of a distribution of particle sizes in a diffusion-controlled process. *Journal of Pharmaceutical Sciences*, 52(1):67–71, 1963.
- Hixson, A. W. and Crowell, J. H. Dependence of Reaction Velocity upon Surface and Agitation: I—Theoretical Consideration. *Industrial and Engineering Chemistry*, 23(8): 923–931, 1931.
- Hu, Y., Liu, Z., Yuan, X., and Zhang, X. Molecular mechanism for liquid-liquid extraction: Two-film theory revisited. *AIChE Journal*, 63(6):2464–2470, 2017.
- Jeon, S. J., Pawelski, A., Kraume, M., and Hong, W. H. Mass transfer enhancement by the alkaline hydrolysis of ethyl acetate in a single droplet system. *Journal of Industrial and Engineering Chemistry*, 17(4):782–787, 2011.
- Kamp, J. and Kraume, M. Influence of drop size and superimposed mass transfer on coalescence in liquid/liquid dispersions – Test cell design for single drop investigations. *Chemical Engineering Research and Design*, 92:635–643, 2014.

- Kaunisto, E., Nilsson, B., and Axelsson, A. Drug dissolution rate measurements evaluation of the rotating disc method. *Pharmaceutical development and technology*, 14 (4):400–408, 2009.
- Kenig, E. Y., Ganguli, A. A., Atmakidis, T., and Chasanis, P. A novel method to capture mass transfer phenomena at free fluid-fluid interfaces. *Chemical Engineering and Processing: Process Intensification*, 50(1):68–76, 2011.
- Kola, R. and Kumar, B. P. A detailed description of synthetic and natural polymers which are used in the formulation of sustained release drug delivery system: A review. *Journal of Chemical and Pharmaceutical Sciences*, 6(3):161–169, 2013.
- Korsmeyer, R. W., Gurny, R., Doelker, E., Buri, P., and Peppas, N. A. Mechanisms of solute release from porous hydrophilic polymers. *International Journal of Pharmaceutics*, 15(1):25–35, 1983.
- Krishna, R. and Taylor, R. Multicomponent mass transfer: Theory and applications. volume 2 of *Handbook of Heat And Mass Transfer. Volume 2: Mass transfer and reactor design*, pages 259–432. Gulf Publishing Company, Houston, Texas, USA, 1986.
- Kronig, R. and Brink, J. C. On the theory of extraction from falling droplets. *Applied Scientific Research*, 2(1):142–154, 1951.
- Kumar, A. and Hartland, S. Correlations for Prediction of Mass Transfer Coefficients in Single Drop Systems and Liquid-Liquid Extraction Columns. *Chemical Engineering Research and Design*, 77(5):372–384, 1999.
- Lee, J., Sung, S., Kim, Y., Park, J. D., and Ahn, K. H. A new paradigm of materials processing—heterogeneity control. *Current Opinion in Chemical Engineering*, 16: 16–22, 2017.
- Levenspiel, O. *Chemical Reaction Engineering*. John Wiley & Sons, USA, 3rd edition, 1999.
- Liang, T.-B. and Slater, M. J. Liquid-liquid extraction drop formation: mass transfer and the influence of surfactant. *Chemical Engineering Science*, 45(1):97–105, 1990.
- Licht, W. and Conway, J. B. Mechanism of Solute Transfer in Spray Towers. *Industrial and Engineering Chemistry*, 42(6):1151–1157, 1950.
- Licht, W. and Pansing, W. F. Solute Transfer from Single Drops in Liquid-Liquid Extraction. *Industrial and Engineering Chemistry*, 45(9):1885–1896, 1953.
- Lohner, H., Czisch, C., Lehmann, P., and Bauckhage, K. Mass transfer processes in liquid-liquid systems with surfactants. *Chemical Engineering and Technology*, 24(11): 1157–1163, 2001.
- Lu, P., Wang, Z., Yang, C., and Mao, Z.-S. Experimental investigation and numerical simulation of mass transfer during drop formation. *Chemical Engineering Science*, 65 (20):5517–5526, 2010.
- Mahapatra, A. K., Murthy, P. N., Swain, R. P., Sravani, Y., and Sagar, G. Sustained

- release products: A review on formulation technologies and regulatory aspects. *Research Journal of Pharmacy and Technology*, 6(12):1415–1425, 2013.
- Mitra, T. and Ghosh, P. Binary coalescence of water drops in organic media in presence of ionic surfactants and salts. *Journal of Dispersion Science and Technology*, 28:785–792, 2007.
- MörTERS, M. and Bart, H.-J. Fluorescence-indicated mass transfer in reactive extraction. *Chemical Engineering and Technology*, 23(4):353–359, 2000.
- Newman, A. B. The drying of porous solids: diffusion and surface emission equations. *AIChE Journal*, 27:203–220, 1931.
- Niebergall, P., Milosovich, G., and Goyan, J. Dissolution rate studies II. Dissolution of particles under conditions of rapid agitation. *Journal of Pharmaceutical Sciences*, 52(3):236–241, 1963.
- Noyes, A. A. and Whitney, W. R. The rate of solution of solid substances in their own solutions. *Journal of the American Chemical Society*, 19(12):930–934, 1897.
- Olsson, E. and Kreiss, G. A conservative level set method for two phase flow. *Journal of Computational Physics*, 210(1):225–246, 2005.
- Pawelski, A., Paschedag, A. R., and Kraume, M. Beschreibung des Stofftransports am Einzeltropfen in Anwesenheit einer schnellen chemischen Reaktion mittels CFD-Simulation. *Chemie-Ingenieur-Technik*, 77(7):874–880, 2005.
- Pawelski, A., Jeon, S. J., Hong, W. H., Paschedag, A. R., and Kraume, M. Interaction of a homogeneous chemical reaction and mass transfer in a single moving droplet. *Chemical Engineering Science*, 104:260–268, 2013.
- Peters, C., Wolff, L., Haase, S., Thien, J., Brands, T., Koß, H. J., and Bardow, A. Multicomponent diffusion coefficients from microfluidics using Raman microspectroscopy. *Lab on a Chip*, 17(16):2768–2776, 2017.
- Piarah, W. H., Paschedag, A. R., and Kraume, M. Numerical simulation of mass transfer between a single drop and an ambient flow. *AIChE Journal*, 47(7):1701–1704, 2001.
- Popovich, A. T., Jervis, R. E., and Trass, O. Mass transfer during single drop formation. *Chemical Engineering Science*, 19(5):357–365, 1964.
- Ritger, P. L. and Peppas, N. A. A simple equation for description of solute release I. Fickian and non-fickian release from non-swellable devices in the form of slabs, spheres, cylinders or discs. *Journal of Controlled Release*, 5(1):23–36, 1987a.
- Ritger, P. L. and Peppas, N. A. A simple equation for description of solute release II. Fickian and anomalous release from swellable devices. *Journal of Controlled Release*, 5(1):37–42, 1987b.
- Safari, V., Arzpeyma, G., Rashchi, F., and Mostoufi, N. A shrinking particle-shrinking core model for leaching of a zinc ore containing silica. *International Journal of Mineral Processing*, 93(1):79–83, 2009.

- Savic, P. Circulation and distortion of liquid drops falling through a viscous medium. Technical Report MT-22, National Research Council Canada, 1953.
- Schulze, K. *Stoffaustausch und Fluidodynamik am bewegten Einzeltropfen unter dem Einfluss von Marangonikonvektion*. PhD thesis, Technische Universität Berlin, 2007.
- Sherwood, T. K., Evans, J. E., and Longcor, J. V. A. Extraction in Spray and Packed Columns. *Industrial and Engineering Chemistry*, 31(9):1144–1150, 1939.
- Slater, M. J. A combined model of mass transfer coefficients for contaminated drop liquid-liquid systems. *The Canadian Journal of Chemical Engineering*, 73(4):462–469, 1995.
- Slattery, J. C., Sagis, L., and Oh, E.-S. *Interfacial transport phenomena*. Springer, New York, 2. ed. edition, 2007. ISBN 9780387384382.
- Soleymani, A., Laari, A., and Turunen, I. Simulation of drop formation in a single hole in solvent extraction using the volume-of-fluid method. *Chemical Engineering Research and Design; ECCE-6*, 86(7):731–738, 2008.
- Tamminen, J., Sainio, T., and Paatero, E. Intensification of metal extraction with high-shear mixing. *Chemical Engineering and Processing*, 73:119–128, 2013.
- Tamminen, J., Lahdenperä, E., Koironen, T., Kuronen, T., Eerola, T., Lensu, L., and Kälviäinen, H. Determination of single droplet sizes, velocities and concentrations with image analysis for reactive extraction of copper. *Chemical Engineering Science*, 167:54–65, 2017.
- Villwock, J., Gebauer, F., Kamp, J., Bart, H.-J., and Kraume, M. Systematic analysis of single droplet coalescence. *Chemical Engineering & Technology*, 37(7):1103–1111, 2014.
- Walia, D. S. and Vir, D. Extraction from single forming drops. *The Chemical Engineering Journal*, 12(2):133–141, 1976a.
- Walia, D. S. and Vir, D. Interphase mass transfer during drop or bubble formation. *Chemical Engineering Science*, 31(7):525–533, 1976b.
- Wang, J. and Flanagan, D. R. General solution for diffusion-controlled dissolution of spherical particles. 1. Theory. *Journal of Pharmaceutical Sciences*, 88(7):731–738, 1999.
- Wang, J. and Flanagan, D. R. General solution for diffusion-controlled dissolution of spherical particles. 2. Evaluation of experimental data. *Journal of Pharmaceutical Sciences*, 91(2):534–542, 2002.
- Wang, Y., Abrahamsson, B., Lindfors, L., and Brasseur, J. G. Comparison and analysis of theoretical models for diffusion-controlled dissolution. *Molecular Pharmaceutics*, 9(5):1052–1066, 2012.
- Wang, Z., Lu, P., Wang, Y., Yang, C., and Mao, Z. Experimental investigation and numerical simulation of Marangoni effect induced by mass transfer during drop formation. *AIChE Journal*, 59(11):4424–4439, 2013.
- Wegener, M., Paschedag, A. R., and Kraume, M. Mass transfer enhancement through

- Marangoni instabilities during single drop formation. *International Journal of Heat and Mass Transfer*, 52(11):2673–2677, 2009.
- Wegener, M., Paul, N., and Kraume, M. Fluid dynamics and mass transfer at single droplets in liquid/liquid systems. *International Journal of Heat and Mass Transfer*, 71: 475–495, 2014.
- Wörner, M. Numerical modeling of multiphase flows in microfluidics and micro process engineering: A review of methods and applications. *Microfluidics and Nanofluidics*, 12(6):841–886, 2012.
- Wu, L. and Liu, M. Preparation and properties of chitosan-coated NPK compound fertilizer with controlled-release and water-retention. *Carbohydrate Polymers*, 72(2): 240–247, 2008.
- Yagi, S. and Kunii, D. Studies on combustion of carbon particles in flames and fluidized beds. *International Symposium on Combustion*, 5(1):231–244, 1955.
- Yang, C. and Mao, Z.-S. Numerical simulation of interphase mass transfer with the level set approach. *Chemical Engineering Science*, 60(10):2643–2660, 2005.
- Zhan, F., Liu, M., Guo, M., and Wu, L. Preparation of superabsorbent polymer with slow-release phosphate fertilizer. *Journal of Applied Polymer Science*, 92(5):3417–3421, 2004.
- Zienkiewicz, O. C., Taylor, R. L., and Nithiarasu, P. *The finite element method for fluid dynamics*. Elsevier Butterworth-Heinemann, Amsterdam ; Boston, 6th ed edition, 2005.

Publication I

E. Lahdenperä and T. Koiranen

**A Novel Manufacturing Method for Sustained Release Products and Modelling
Dissolution**

Reprinted from *Journal of Thermodynamics & Catalysis*, 7(1), 2016, DOI:
10.4172/2157-7544.1000159



A Novel Manufacturing Method for Sustained Release Products and Modelling Dissolution

Lahdenperä E* and Koiranen T

LUT School of Engineering Sciences, Lappeenranta University of Technology, Lappeenranta, Finland

Abstract

A novel processing method for the manufacturing of slow-release particles is proposed. The method is based on the wet milling of active compounds and the selected biodegradable polymers combined with subsequent drying. In the proposed method the dissolution barrier is processed in one step compared to traditional methods consisting of several steps. The experimental dissolution curves of natural polymer (native potato starch and lignin) coated salts were compared with unmilled and milled salts. The dissolution process model was developed in order to characterize and to design sustained release particles. Models were verified with the existing dissolution data. Verified models combined with SEM-images could support the proposed dissolution mechanisms for different polymers. Estimates of effective surface area and diffusion layer thickness (active surface model) and effective diffusivity and gelling layer thickness (constant gel radius model) is achieved.

Keywords: Sustained release; Wet milling; Dissolution model

Introduction

In chemical industry there is a trend to increase process efficiencies and to reduce substantially equipment size, energy consumption and amount of produced waste thus aiming at sustainable processes. These developments share a common focus named as Process Intensification. The increase in efficiency can be achieved, for example, by accelerating chemical reactions or creating high mass and energy transfer rates. Efficiency can be also increased by combining several unit operations in one equipment thus reducing the amount of required processing steps and reducing throughput times [1]. On the other hand, also the reduction of speed of rate-based processes like slow-release dissolution enables to achieve products that use less material, are cheaper and safer and environmentally friendly. Recent reviews of slow-release technologies have been published by Azeem *et al.*, Wu and Liu, Zhan *et al.*, Han *et al.*, Hanafi *et al.*, Swarbrick, Wolny *et al.*, Ching *et al.*, Madene *et al.*, Lu *et al.* to name a few [2-11]. In pharmaceuticals the goal is to minimize the number of drug uptakes and to keep a controlled amount of pharmaceutical ingredients in the body system using sustained release products. In case of foods and nutrients the active compound is covered with a protective wall material to impart valuable compounds against evaporation, reaction or migration. In addition, *e.g.*, vitamins can be masked to hide bad taste. In cosmetics, the extra skin irritation can be eliminated using slow-release particles in ointments and in creams [12].

Production of slow-release particles is typically based on coating, spray-drying or melt extrusion. Those methods include either separate dissolution, heating or granulation processes [2]. In the chemical processing polymer derivatization and crosslinking are involved [4,13]. So there is a potential to increase efficiency by reducing amount of processing steps and by utilizing as barrier material biodegradable cheap polymers achieve the goal of sustainability as well.

To allow design of slow release products a model of dissolution is required. These models can be divided roughly into two groups: empirical models implemented as empirical or semi-empirical equations describing dissolved amount as function of time and mechanistic models based on material balance between dissolving spherical particle and solution and where the dissolution rate is determined by solute diffusion [14]. Several type of dissolution models,

both empirical and mechanistic models, are introduced in literature [14-18] and details of the models depends on the mechanism of the dissolution process and how the model will be applied. Mechanism of dissolution process consists of two steps: the first is surface reaction of molecules from solid into liquid at solid-liquid interface and the second step is diffusion across a thin diffusion layer from solid-liquid interface into bulk solution. It is assumed that the detachment of solute molecules from crystal is fast compared to diffusion step which is the rate determining step [19]. Also it is assumed that concentration at solid-liquid interface is saturation concentration and concentration in bulk is small compared to saturation concentration (=sink condition).

An example of the mechanistic model is the general solution of diffusion layer model for a mono dispersed spherical particle by Wang and Flanagan [19]. They have solved the mass balance expression for a spherical particle by applying pseudo steady state diffusion over constant thickness diffusion layer. Diffusion layer thickness is assumed to prevail during the whole dissolution. According to their study Wang and Flanagan [20] reached the conclusion that this is a valid assumption if mixing conditions do not change during the dissolution.

The general diffusion model assumes spherical particles and dissolution rate is homogeneous over the whole particle area and that the dissolving particle is in direct contact with solvent via the stagnant diffusion layer. In practice the dissolution may be hindered by a fully coating layer of another material or material attached on particle surface thus partly blanking the area and the general model has to be modified in order to take into account these inhibiting effects. Two common mechanisms for coated particles are the shrinking core-

*Corresponding author: Lahdenperä E, LUT School of Engineering Sciences, Lappeenranta University of Technology, Lappeenranta, F-53851, Finland, Tel: 358294462111; E-mail: Esko.Lahdenpera@lut.fi

Received January 23, 2016; Accepted February 09, 2016; Published February 15, 2016

Citation: Lahdenperä E, Koiranen T (2016) A Novel Manufacturing Method for Sustained Release Products and Modelling Dissolution. J Thermodyn Catal 7: 159. doi:10.4172/2159-7544.1000159

Copyright: © 2016 Lahdenperä E, et al. This is an open-access article distributed under the terms of the Creative Commons Attribution License, which permits unrestricted use, distribution, and reproduction in any medium, provided the original author and source are credited.

constant particle size model and the shrinking core-shrinking particle size model [17,18]. In the constant particle size model it is assumed that the coating layer diameter stays constant meanwhile the core inside shrinks. In the shrinking particle size model the particle size decreases and the coating layer thickness stays constant [18]. Safari *et al.* [18] have studied leaching of zinc ore containing silica and they have verified by experiments the validity of constant thickness gel layer model in their application. Partly blanked model, also named as active surface model, is the plain general diffusion model where the dissolution area is a fraction of full particle area.

Equations of empirical models are mostly n-th order reaction kinetic type functions, either analytical functions (like zero order, first order, Weibull) or a certain release parameter is used to characterize dissolution [14]. Costa and Lobo have evaluated several empirical equations with drug dissolution experiment data [14,15].

In this study the novel one step processing method based on wet milling and subsequent drying for the manufacturing sustained release particles is presented. The product particles have been manufactured as well as the dissolution tests have been done in lab-scale to demonstrate the method feasibility. The dissolution rates of the product particles were compared using the dissolution times for equal amounts of the dissolved salt. The dissolution was modelled by using three different mass transfer kinetics, and the models were fitted with the experimental data in order to verify dissolution mechanism. SEM=(scanning electronic microscope) image of coated and dried particles were taken and used to verify mechanism. Estimates of the effective surface area and diffusion layer thickness for the active surface model and effective diffusivity and gelling layer thickness for the constant gel radius model were determined for extracting coating parameters.

Governing equations

Three dissolution models were selected to fit experimental results: first order model, active surface model and constant gel radius model.

First order model: Here it is assumed that dissolution rate dc/dt is analogous compared to first order reaction:

$$dc/dt = -k_p c_p \quad (1)$$

where c_p is particle concentration in solution and k_p apparent dissolution rate constant. When (1) is solved and particle concentration changed into liquid concentration the expression is

$$(c_f - c)/(c_f - c_0) = \exp(k_p t) \quad (2)$$

where c is liquid concentration, c_f final concentration and c_0 initial concentration.

Active surface model: It is assumed that only a certain part of the surface is active and rest is covered by the coating material. Dissolution model is based on general diffusion model [19]. Liquid phase concentration change due to diffusion across layer having thickness h is

$$dc/dt = (Z/V) A k_c \Delta c \quad (3)$$

where, Z/V is particle number concentration, A sphere area, k_c mass transfer coefficient and Δc concentration difference over the layer. Concentration at the layer inner boundary is saturated concentration c_s and it is assumed that $c_s \gg c$ so $\Delta c \approx c_s$. Expression for concentration can be found also by integrating concentration gradient over the layer [19] and the result is

$$dc/dt = A(Z/V) D_{ab} c_s (1/r+1/h) \quad (4)$$

Equating (3) and (4), the expression of mass transfer coefficient is

$$k_c = D_{ab} (1/r+1/h) \quad (5)$$

Solution concentration change is

$$dc/dt = -dc_p/dt = -(Z/V) \rho_p A dr/dt \quad (6)$$

where ρ_p is particle density. It is assumed that the amount of particles does not change during dissolution so the number concentration Z/V can be calculated using initial particle concentration

$$Z/V = c_{p,0} / (\rho_p 4/3\pi r_0^3) \quad (7)$$

where, $c_{p,0}$ is initial particle concentration and r_0 initial particle diameter. Because only a certain fraction of particle surface is active solution concentration change is

$$dc/dt = a(Z/V) A k_c c_s \quad (8)$$

where a is surface activity factor between 0 and 1.

Constant gel radius model: Here it is assumed that there is a constant radius gel layer over the particle which slows down diffusion. A model for mass transfer coefficient is [17]

$$k_c = D_{eff} / (R_0 - r) = e D_{AB} / (R_0 - r) \quad (9)$$

where $D_{eff} = e D_{AB}$ is effective diffusion coefficient, e is effectiveness factor related to KCl diffusivity and it has values from 0 to 1 and R_0 constant gel radius. Otherwise concentration change is modelled using equations (4) and (6).

Experimental

Materials

Model compound was potassium chloride KCl (Riedel-Haën, CAS 7447-40-7). Non-toxic, relatively inexpensive and biodegradable coating materials in this study were neutral unmodified potato starch (ChemGate Oy, CAS 9005-25-8) and Kraft lignin (Sigma-Aldrich, CAS 8068-05-01). De-ionized water and ethanol (purity >99.5 w%) were the solvents.

Experimental set-up

Potassium chloride, polymer and solvent were milled in the mortar. The compositions of the polymer mixes in the experiments are shown in Table 1. In case of potato starch the mix was preheated to 65°C due to starch swelling [21] before milling, and in case of lignin the mix was heated to 40°C for the partial lignin dissolution [22]. The grinding time was 10 minutes in each experiment during which the solvent was evaporated. The drying completion was assured by weighing the material before and after the processing.

The dissolution of product particles were measured in a well-mixed laboratory-size vessel (200 ml volume, mixer speed 0.8 m/s) at constant temperature 25°C. The initial KCl liquid concentration in the dissolution experiments was 0.27 mol/L. The electric conductivity (Consort C3310) was calibrated to molar KCl concentrations in advance, as well as the electric conductivity effect of polymers were also measured. According to the pure polymer measurements, the measurement error was max 2% to the electric conductivity.

Results

Experimental results

SEM images of the particles (Figures 1 and 2) and the particle size

Test number	Initial KCl concentration (mol/L)	KCl amount (g)	Polymer	Amount of polymer (g)	Solvent	Amount of solvent (g)
1	0.27	7.7	-	0		0
2	0.27	7.7	-	0	30	0
3	0.27	7.7	Starch	0.77		0.77
4	0.27	7.7	Starch	1.54	4.1	1.54
5	0.27	7.7	Lignin	0.77	1.9	0.77
6	0.27	7.7	Lignin	1.54		1.54

Table 1: Composition of biodegradable polymer mixes. Polymer amounts 10% and 20% of the salt. Tests 1 and 2: grinded and ungrinded KCl samples.

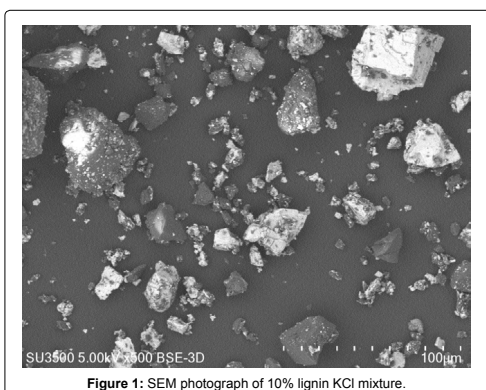


Figure 1: SEM photograph of 10% lignin KCl mixture.

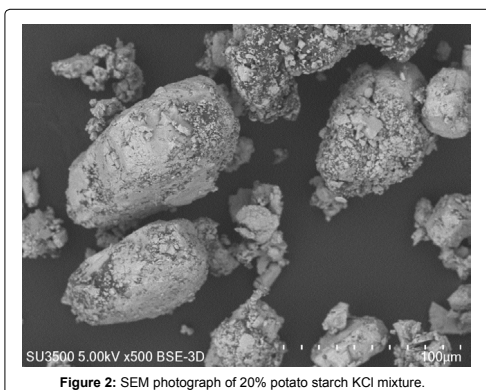


Figure 2: SEM photograph of 20% potato starch KCl mixture.

distributions (Figure 3) for the highest polymer loadings are presented. The crystallinity and the purity of KCl in starch coated particles were verified by X-ray powder diffraction (Figure 4). The dissolution times and profiles for 10 w% and 20 w% load of polymers are presented in Table 2 and in Figures 5 and 6.

Dissolution modeling

Three dissolution models were used to fit experimental data: first order reaction model, active surface model and constant gel radius

model. KCl physical properties used in the models are shown in Table 3. Models were implemented and solved with MATLAB [25].

Calculated model parameters for each case are in Table 4. Goodness of fit was evaluated by calculating coefficient of determination R^2 :

$$R^2 = 1 - SSR/SST \quad (10)$$

$$SSR = \sum (c_i - c_{i,est})^2 \quad (11)$$

$$c = \sum c_i / n \quad (12)$$

$$\bar{c} = \sum c_i / n \quad (13)$$

Where, c_i is measured value, $c_{i,est}$ value estimated from model and n amount of experiment points. R^2 values are shown in Table 5. For three different models experimental and fitted dissolution curves for each test is shown in Figures 7-9.

Discussion

The novel and straightforward manufacturing method was developed which comprised of: charging of starting materials, heating, wet milling and product drying. The lignin and the potato starch were selected due to their biodegradability and the low harmfulness in the environment/health issues. The reference particles were ungrinded and grinded salt, and the KCl was selected for the salt due to the easy correlation and validation of electric conductivity values to molar concentrations. The dissolution tests were done under a vigorous mixing in order to obtain maximum homogenous suspension.

According to the SEM photographs the surface is covered with separate lignin particles (Figure 1), but the coverage of the starch on the KCl surface is more thorough due to the starch swelling during particle processing (Figure 2). With equal amounts of polymers the particle size distributions were similar and comparable to the grinded KCl particles (Figure 3). According to the dissolution data the dissolution time (90% dissolved) was doubled with the lignin coated particles and was 5.5 times longer with the starch coated particles (Table 2 and Figure 6) compared to the reference KCl particles.

Experimental first order model was successful in approximating dissolution and the model parameter k_R can be used in comparisons between dissolution rates of different spheres. This is also reflected in Table 2, where to different particles are tabulated from smallest to largest 90% dissolution times which is same order if sorting were done from largest to smallest k_R (Table 4).

The dissolution of the ungrinded and grinded particles was unexpectedly best modelled by the gel radius model. The effective diffusivities were 19.2% and 100% for the pure KCl particles (grinded and ungrinded). The poor wettability may have been the cause for the small diffusivity for the grinded KCl particles. During the dissolution tests the pure KCl particles may have formed aggregates, which may

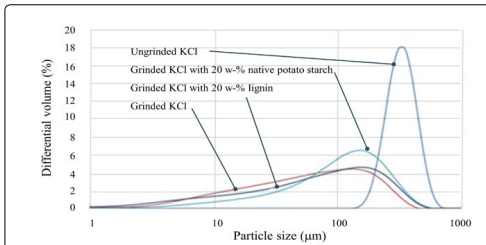


Figure 3: Particle size distributions of KCl with 20 w% polymer particles and ungrinded KCl as a reference.

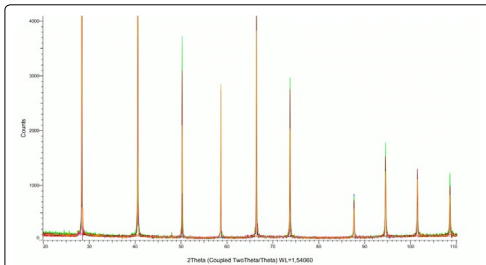


Figure 4: XRPD of the 20% potato starch-KCl particles, and the ungrinded KCl as a reference.

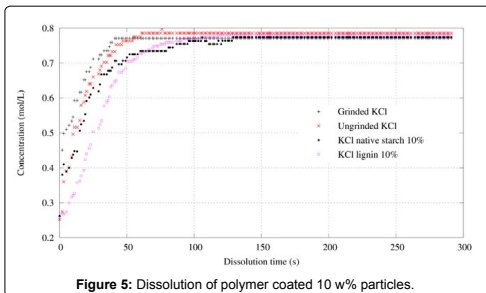


Figure 5: Dissolution of polymer coated 10 w% particles.

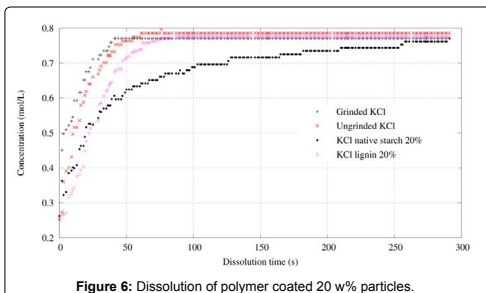


Figure 6: Dissolution of polymer coated 20 w% particles.

	Dissolution times, s					
	G	U	NS10	L10	L20	NS20
10% dissolved	1	2	1	7	9	3
50% dissolved	7	1	16	23	30	20
90% dissolved	30	39	52	52	61	164

Table 2: Dissolution times for 10%, 50% and 90% dissolutions from dissolution measurements (Figures 5 and 6). G=Grinded KCl, U=Ungrinded KCl, NS10=Native Starch 10%, L10=Lignin 10%, L20=Lignin 20%, NS20=Native Starch 20%.

Property	Value	Source
Density ρ_p	1998 kg/m ³	[23]
solubility c_s	355 kg/m ³	[23]
diffusivity D_{AB}	1.99×10^{-9} m ² /s	[24]

Table 3: KCl physical properties.

Model	Experiments					
	G	U	NS10	L10	L20	NS20
First order model						
$k_p/10^{-3} \text{ s}^{-1}$	89	57	44	34	30	21
Active surface model						
$\alpha/\%$	4.0	4.0	5.4	5.7	5.1	4.0
$z=hr/r_0$	0.38	0.027	0.50	3.6	3.6	0.97
Gel layer model						
$e/\%$	19.2	100	26.9	32.3	30.3	12.9
$D_0/\mu\text{m}$	96	530	170	222	222	141

Table 4: Estimated model parameters. G=Grinded KCl; U=Ungrinded KCl; NS10=Native Starch 10%; L10=Lignin 10%; L20=Lignin 20%; NS20=Native Starch 20%.

Model	Experiments					
	G	U	NS10	L10	L20	NS20
First order model	0.9165	0.9916	0.9768	0.9451	0.9547	0.9093
Active surface model	0.8313	0.9873	0.9363	0.9859	0.9841	0.7710
Gel layer model	0.9660	0.9905	0.9779	0.9542	0.9621	0.9844

Table 5: Goodness of fit: R^2 value. G=Grinded KCl; U=Ungrinded KCl; NS10=Native Starch 10%; L10=Lignin 10%; L20=Lignin 20%; NS20=Native Starch 20%.

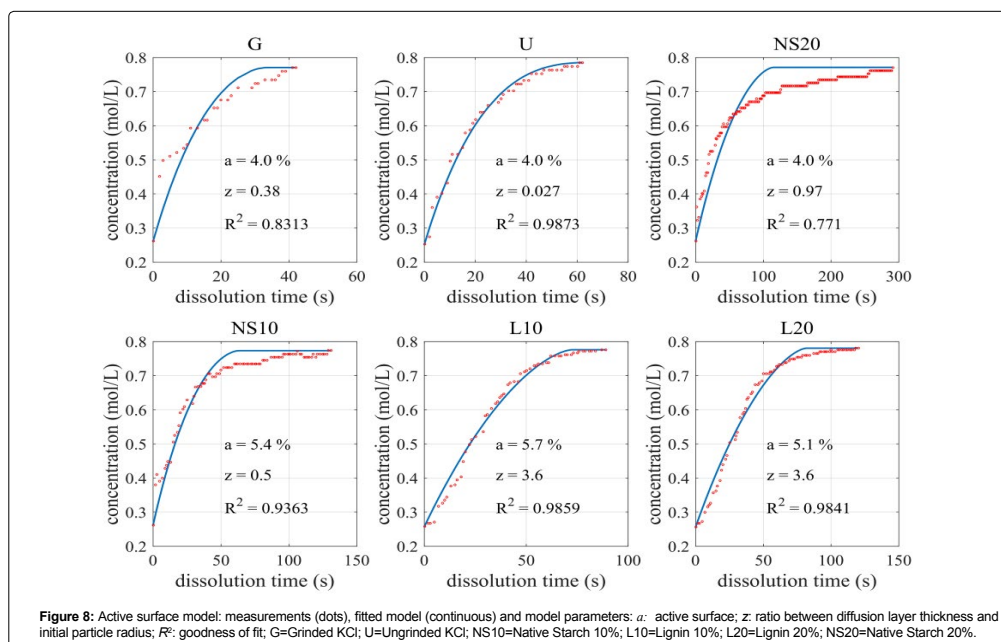
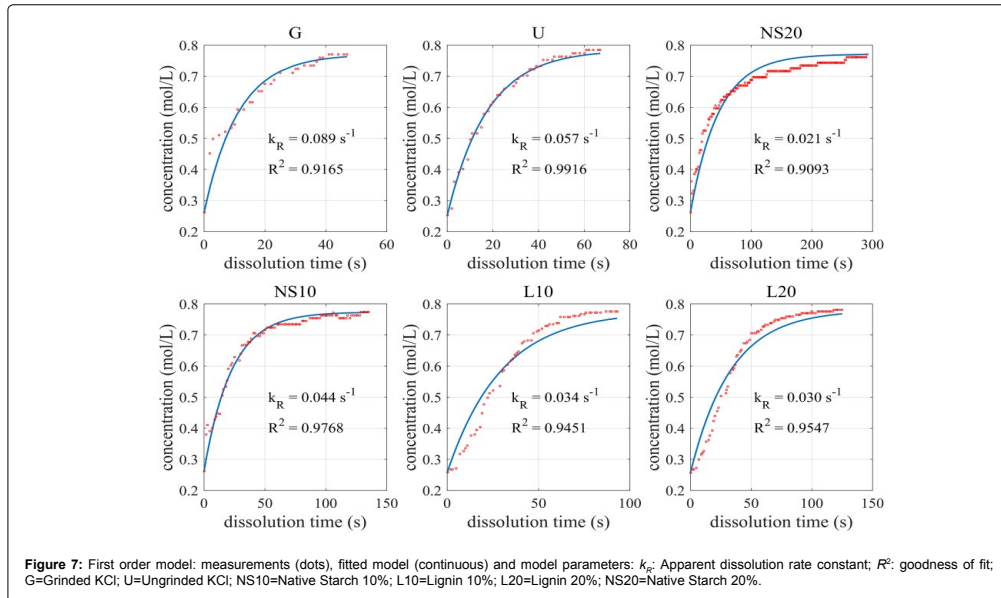
explain the gel radius model suitability.

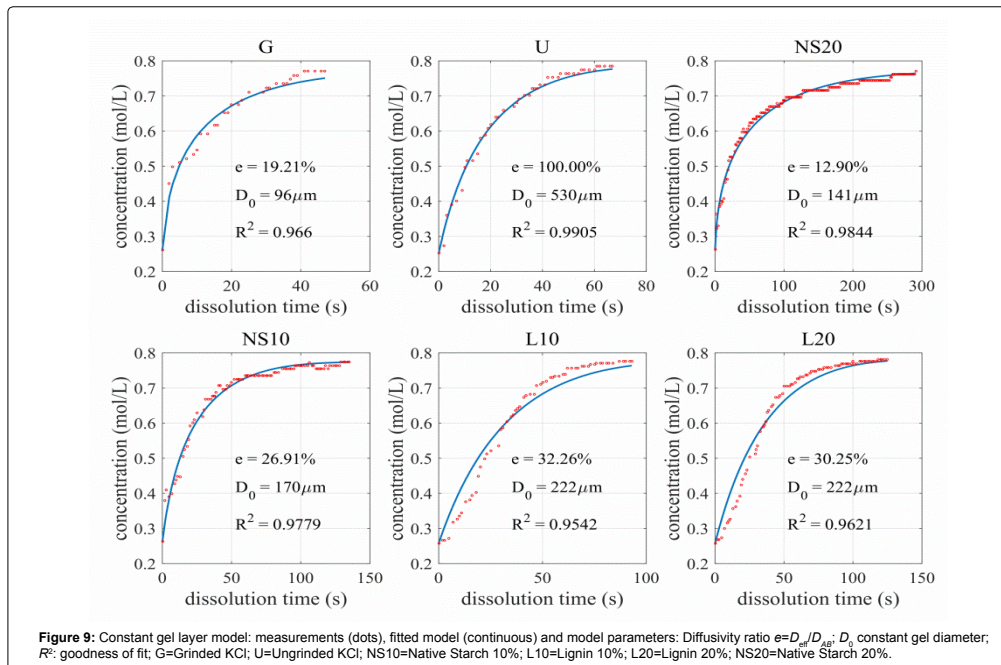
The dissolution data of lignin coated particles was best fitted for the effective surface model, although the data fit to the gel radius model was also good. The effective surface areas for the 10% and 20% lignin loadings were 5.7% and 5.1%. According to the SEM photographs (Figure 2) the lignin was partly coating the KCl particle surfaces which explains the suitability of this model. Additionally, the lignin is not dissolved into water and therefore gelling surface is not formed.

According to the results the gel radius model can also be used to model predicts especially well the dissolution from the data of the starch coated particles. The estimated effective diffusivity ratios e were 26.9% and 12.9% in the case of 10% and 20% starch coated KCl particles which correspond to the starch loadings. Estimated gel diameters D_0 were 170 and 141 μm .

Conclusions

Dissolution data of polymer coated KCl particles has been presented. Particles were manufactured by wet milling salt and polymers. They were dried during the milling stage which can be considered an energy efficient solution due to the fact that milling energy turns itself into





heat. The produced polymer coated particles had almost six time longer dissolution times compared to the pure KCl particles under vigorous mixing conditions. The dissolution profiles were simulated using the traditional first order reaction kinetics model, the active surface model, and the constant gel radius model. The active surface model was well suited for the lignin coated particles due to the active surface reduction of the attached lignin particles. On the other hand, a very good data fit was obtained for the starch coated particles using the constant gel radius model. This result was expected because of the gelling nature of the native starch.

The potential of the wet grinding and the simultaneous drying of particles as a manufacturing method in coating of dissolvable compounds has been demonstrated. In the production of different coatings the developed models were used for explaining gel formation or active surface of particles in dissolution processes.

Notations

α	Surface activity factor in active surface model, 0...1
A	Particle area, m^2
c	KCl concentration, mol/L
c_0	KCl initial concentration, mol/L
c_f	KCl final concentration, mol/L
c_i	i th experimental concentration
$c_{i,est}$	i th estimated concentration
c_p	KCl particle concentration, g/L
c_s	KCl solubility in water, kg/m^3

D_{eff}	Effective diffusivity in gel layer model, m^2/s
D_{AB}	KCl diffusivity in water, m^2/s
D_0	Constant gel diameter in gel layer model, m
e	Diffusivity effectiveness factor in gel layer model, 0...1
h	Diffusion layer thickness, m
k_c	Mass transfer coefficient, m/s
k_R	First order model apparent dissolution rate constant, 1/s
n	Amount of experimental points
r	Particle radius, m
r_0	Particle initial radius, m
R_0	Gel radius in gel layer model, m
t	Time, s
V	Liquid volume, L
Z	KCl particle count
Z/V	Particle number concentration, 1/L

Greek alphabet

ρ_p	KCl particle density, kg/m^3
----------	--

Acknowledgements

The authors gratefully acknowledge the Academy of Finland for financial support. Special thanks go to laboratory technician Mr. Toni Väkiparta for performing SEM, XPRD and particle size analyses.

References

1. Stankiewicz A, Moulijn JA (2003) Re-Engineering the Chemical Processing Plants: Process Intensification. Chemical Industries-Series, Marcel-Dekker, USA.

2. Azeem B, KuShaari K, Man ZB, Basit A, Thanh TH (2014) Review on materials & methods to produce controlled release coated urea fertilizer. J Control Release 181: 11-21.
3. Wu L, Liu M (2008) Preparation and properties of chitosan-coated NPK compound fertilizer with controlled-release and water-retention. Carbohydrate Polymers 72: 240-247.
4. Zhan F, Liu M, Guo M, Wu L (2004) Preparation of superabsorbent polymer with slow-release phosphate fertilizer. J Appl Polym Sci 92: 3417-3421.
5. Han X, Chan S, Hu X (2009) Controlled-release fertilizer encapsulated by starch/polyvinyl alcohol coating. Desalination 240: 21-26.
6. Hanafi MM, Eltaib SM, Ahmad MB (2000) Physical and chemical characteristics of controlled release compound fertilizer. European Polymer Journal 36: 2081-2088.
7. Swarbrick J, Boylan JC (ed) (2002) Encyclopedia of Pharmaceutical Technology. 2nd edn. Marcel-Dekker, USA.
8. Wolny D, Gruchlik A, Chodurek E, Szara M, Dzierzewicz Z (2012) Comparison of dissolution profiles of theophylline extended-release dosage forms. Acta Pol Pharm 69: 1384-1386.
9. Ching SH, Bansal N, Bhandari BB (2015) Alginate gel particles-a review of production techniques and physical properties. Critical Reviews in Food Science and Nutrition.
10. Madene A, Jacquot M, Scher J, Desobry S (2006) Flavour encapsulation and controlled release – A review. Int J Food Sci Technol 41: 1-21.
11. Lu DR, Xiao CM, Xu SJ (2009) Starch-based completely biodegradable polymer materials. eXPRESS Polymer Letters 3: 366-375.
12. Ammala A (2013) Biodegradable polymers as encapsulation materials for cosmetics and personal care markets. Int J Cosmet Sci 35: 113-124.
13. Chen L, Xie Z, Zhuang X, Chen X, Jing X, et al. (2008) Controlled release of urea encapsulated by starch-g-poly(L-lactide). Carbohydrate Polymers 72: 342-348.
14. Costa P, Sousa Lobo JM (2001) Modeling and comparison of dissolution profiles. Eur J Pharm Sci 13: 123-133.
15. Paulo C, Sousa Lobo JM (2001) Influence of dissolution medium agitation on release profiles of sustained-release tablets. Drug Dev Ind Pharm 27: 811-817.
16. Di Colo G, Baggiani A, Zambito Y, Mollica G, Geppi M, et al. (2006) A new hydrogel for the extended and complete prednisolone release in the GI tract. Int J Pharm 310: 154-161.
17. Cussler EL (1997) Diffusion mass transfer in fluid systems. 2nd edn. Cambridge University Press.
18. Safari V, Arzpeyma G, Rashchi F, Mostoufi N (2009) A shrinking particle-shrinking core model for leaching of a zinc ore containing silica. Int J Miner Process 93: 79-83.
19. Wang J, Flanagan DR (1999) General solution for diffusion-controlled dissolution of spherical particles. 1. Theory. J Pharm Sci 88:731-738.
20. Wang J, Flanagan DR (2002) General solution for diffusion-controlled dissolution of spherical particles. 2. Evaluation of experimental data. J Pharm Sci 91: 534-542.
21. Tester R, Morrison WR (1990) Swelling and gelatinization of cereal starches. I. Effects of amylopectin, amylose and lipids. Cereal Chemistry 67: 551-557.
22. Schuerch C (1952) The Solvent Properties of Liquids and Their Relation to the Solubility, Swelling, Isolation and Fractionation of Lignin. J Am Chem Soc 74: 5061-5067.
23. Haynes WM (2015) CRC Handbook of Chemistry and Physics. 96th edn. CRC Press.
24. Reid CR, Prausnitz JM, Poling BE (1987) The properties of gases and liquids. 4th edn. McGraw-Hill, USA.
25. MATLAB 8.3.0.532 (2014) Optimization Toolbox 7.0, The MathWorks Inc., Natick, Massachusetts, United States of America.

Citation: Lahdenperä E, Koironen T (2016) A Novel Manufacturing Method for Sustained Release Products and Modelling Dissolution. J Thermodyn Catal 7: 159. doi:10.4172/2159-7544.1000159

**Submit your next manuscript and get advantages of OMICS
Group submissions**

Unique features:

- User friendly/feasible website-translation of your paper to 50 world's leading languages
- Audio Version of published paper
- Digital articles to share and explore

Special features:

- 400 Open Access Journals
- 30,000 editorial team
- 21 days rapid review process
- Quality and quick editorial, review and publication processing
- Indexing at PubMed (partial), Scopus, EBSCO, Index Copernicus and Google Scholar etc
- Sharing Option: Social Networking Enabled
- Authors, Reviewers and Editors rewarded with online Scientific Credits
- Better discount for your subsequent articles

Submit your manuscript at: <http://www.editorialmanager.com/biochem>

Publication II

J. Tamminen, E. Lahdenperä, T. Koiranen, T. Kuronen, T. Eerola, L. Lensu,
H. Kälviäinen

**Determination of single droplet sizes, velocities and concentrations with image
analysis for reactive extraction of copper**

Reprinted from *Chemical Engineering Science*, 167, pp. 54–69, 2017,
DOI: 10.1016/j.ces.2017.03.048



Determination of single droplet sizes, velocities and concentrations with image analysis for reactive extraction of copper



Jussi Tamminen*, Esko Lahdenperä, Tuomas Koiranen, Toni Kuronen, Tuomas Eerola, Lasse Lensu, Heikki Kälviäinen

School of Engineering Science, Lappeenranta University of Technology, P.O. Box 20, FIN-53851 Lappeenranta, Finland

HIGHLIGHTS

- Single organic droplet copper extraction was measured using funnel and imaging.
- Droplet inner concentrations were determined from analysis of video frames.
- Results include concentration profiles and average concentrations in droplet.
- Funnel measurement leads to higher mass transfer due to indirect measurement.
- Dynamic droplet analysis is enabled using velocity, shape and concentration.

ARTICLE INFO

Article history:

Received 3 January 2017
Received in revised form 4 March 2017
Accepted 21 March 2017
Available online 23 March 2017

Keywords:

Copper extraction
Single droplet extraction
Image analysis
Video analysis
Photometric concentration analysis

ABSTRACT

The proposed image analysis method allows the measurement of organic phase droplet sizes, velocities, and copper concentrations in single droplet column copper extraction using hydroxyoxime complexation. The method uses image acquisition sequences from video, detection of moving droplets, binarization of background subtracted images, and noise reduction from images. The image analysis method enabled characterizing the shape of droplets, by determining the droplet minor and major axis lengths. The method can detect droplet concentration directly inside the column wherever the droplet is visible. Image based method was validated against reference samples which were analyzed using spectrophotometry. The traditional concentration measurement using the spectrophotometric analysis of column outlet sample collection was performed for comparison purposes. The direct image analysis showed smaller variation in mass transfer results because of longer and non-uniform residence times when using sample collection. However, separately collected sample analysis together with the image analysis enables determination of the copper mass transfer during all the three steps of column experiment. Image analysis can also be used to reveal concentration profiles inside the droplet. This method is not limited to extractants, but it can be applied to systems where a suitable color change is present depending on camera sensor technology.

© 2017 The Authors. Published by Elsevier Ltd. This is an open access article under the CC BY license (<http://creativecommons.org/licenses/by/4.0/>).

1. Introduction

Mass transfer is an important phenomenon affecting the design of liquid-liquid contactor units utilizing reactive extraction. To properly design the units, it is important to understand and quantitatively evaluate the effect of different mass-transfer phenomena in the whole process. These phenomena are solute transfer from bulk to the interface, interfacial reaction, and transport from interface to bulk. The mass transfer in solvent extraction depends on, among other variables, droplet sizes, velocities, and concentrations.

When the size, velocity, and inner concentration of a single droplet are determined, mass transfer into the droplet is defined.

The presence of suitable reagents enhances mass transfer between the continuous and droplet phases in the reactive extraction. Especially in industrial hydrometallurgical processes, metal extraction with complex forming extractants is in common use. Also substantial application areas of reactive extraction can be found among environmental, petrochemical, chemical, and biochemical applications (Bart and Stevens, 2004).

To experimentally investigate combined interfacial kinetics and mass transfer, different experimental methods are available (Hanna and Noble, 1985). Among these methods, single droplet measurements are widely applied in mass transfer experiments

* Corresponding author.

E-mail address: jussi.v.tamminen@lut.fi (J. Tamminen).

Nomenclature

<i>A</i>	absorbance, [-]
<i>A, B, C, D, E, F</i>	parameters of quadratic formula
<i>c</i>	concentration, [mol/L, mmol/L]
<i>d</i>	diameter [mm]
<i>E</i>	droplet aspect ratio [-]
<i>g</i>	earth gravitational acceleration [9.81 ms ⁻²]
<i>I</i>	light intensity, [-]
<i>L</i>	optical path length, [mm]
<i>l</i>	length or distance, [mm]
<i>n</i>	amount of copper, [mol, mmol]
<i>p</i>	pixel value, [-]
<i>u</i>	droplet velocity, [mm/s]
<i>V</i>	volume, [mL]
\dot{V}	droplet phase feed flow rate, [mL/min]
<i>X</i>	conversion ($X = 1 - c/c_0$), [-]

Greek alphabet

$\Delta\rho$	density difference ($\rho_c - \rho_d$), [kg/m ³]
Δc	concentration difference, [mmol/L]
ρ	density, [kg/m ³]
γ	interfacial tension, [mN/m]
ϵ	molar absorptivity, [L/(mmol mm)]
μ	dynamic viscosity [Pa s]

Subscripts, indices

0	initial value
aq	aqueous phase
bg	background
BOT	column bottom part
c	continuous phase
ch	chord length
cr	critical value
d	droplet or droplet phase
e	equivalent
<i>i, j</i>	pixel location indices
major, minor	major and minor axis of a droplet image
org	organic phase
<i>p</i>	value for pixel
Rise	rise
Sample	analysis from sample
<i>t</i>	terminal velocity
TOP	column top part

Dimensionless numbers

<i>Eo</i>	Eötvös number, $Eo = g\Delta\rho d^2/\gamma$
<i>Mo</i>	Morton number, $Mo = g\mu_c^4\Delta\rho/(\rho_c^2\gamma^3)$

of liquid-liquid systems to determine the mass transfer coefficients, interfacial kinetics and extraction efficiencies (for example, Whewell et al., 1975; Henschke and Pfennig, 1999; Kumar and Hartland, 1999; Biswas et al., 1996, 1997; Wegener et al., 2009).

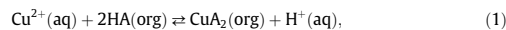
In single droplet systems, a droplet is rising or settling in an ambient continuous liquid. Droplets are collected from a funnel at the column outlet and concentrations are analyzed. Reaction kinetics and mass transfer rates can be determined from this data.

Already in the 1950s, Licht and Conway (1950) and Licht and Pansing (1953) verified that the mass transfer in single droplet extraction is divided into three stages: mass transfer during droplet formation, mass transfer in free rising/settling, and mass transfer during droplet coalescence. Experimental arrangements should be made so that contribution of each phenomena to the extraction process can be determined. It is commonly agreed, that the contribution of droplet formation time to the mass transfer can be substantial, and the related error should be taken into account in the formation of mass transfer correlations (Wegener et al., 2014; Liang and Slater, 1990; Licht and Conway, 1950; Licht and Pansing, 1953). By contrast, the effect of droplet coalescence in the column outlet collector is assumed to be negligible, which has not been clearly shown.

Traditional single droplet experiments do not provide any information on the conditions inside the droplet during its rise. For example, mass transfer leads to concentration changes inside the droplet and at the interface. These changes can generate interfacial tension gradients which in turn lead to the Marangoni convection (Wegener et al., 2009, 2014). The effect of Marangoni convection cannot be directly observed in pure concentration measurements. Because of this, it would be beneficial also to be able to follow droplet velocities and concentration profiles within the droplet, at the interface and in the near vicinity of the droplet in the ambient phase. Flow pattern and concentration front visualization inside a droplet using decolorization with pH indicator have been made by Schulze (2007) and Pawelski et al. (2005) but the concentration profiles have not been measured. Decolorization, however, has

been used to reveal Marangoni convection. MörTERS and Bart (2000) and Baumann and Mühlfriedel (2002) have determined indirectly concentration profiles near the phase boundary using a laser induced fluorescence to track tracer concentrations. Baumann and Mühlfriedel measured time-dependent average tracer concentration profiles on the flat interface between two immiscible liquids. MörTERS and Bart (2000), using D2EHPA system, determined time-dependent tracer concentration profiles inside a droplet to investigate diffusion inside and outside droplets in reactive extraction. Measured tracer concentration profiles were used as a basis to determine organic complex diffusion coefficient. The determination the effect of continuous phase flow on the droplet internal circulation was not successful due to experimental arrangements. In further studies by MörTERS and Bart (2003), the measured concentration profiles were a basis for a Stefan-Maxwell based diffusion model for the mass transfer. Diffusion model was applied to zinc-D2EHPA single droplet experiments but the model was not able to describe experimental results satisfactorily and this is probably due to convective effect not included in the model.

In this work, the problems in single droplet extraction experiments are approached with a direct nonintrusive measurement system where the droplet velocity, droplet diameter, and concentration inside the droplet are determined by using digital imaging and subsequent image analysis. In this research, copper extraction from the aqueous solution to the organic solvent using Acorga M5640 extractant is analyzed. The interfacial reaction,



where the reactant HA (Acorga M5640) exchanges Cu-ions from the aqueous phase and the Cu-complex CuA₂ can be followed directly and visually due to color change.

In experiments, concentrations, droplet velocities, and diameters are determined as averages from several droplets to minimize the effect of experimental variability. This direct droplet concentration analysis allows exact determination of mass transfer rates during the three stages in the single droplet experiment. In tradi-

The effect of rise on the mass transfer into the droplet could be determined by comparing the measured concentrations in the column bottom and top.

2.4. Image analysis

The first step in the image-based droplet analysis was to acquire image sequences using the setup described in Section 2.2. The AVT Oscar F-510C FireWire camera was used to obtain the image sequences (stored as uncompressed image files) for the concentration analysis and droplet size measurements. The Canon Legria HF R47 camera was used to obtain videos for the droplet size, velocity, and acceleration measurements. The second step was to detect moving droplets in the videos. Since the background (the column with the continuous phase) was static except for the moving droplets, the detection problem was solved using a background subtraction method. The background subtraction was performed by subtracting the previous frame in the image sequence from the input frame. This way the regions, where the subsequent frames differ due to the movement of droplets, were separated from the background (Cheung and Kamath, 2005).

The background subtracted image was then binarized by selecting an appropriate threshold value for the red color channel. The red channel was selected based on preliminary experiments where it was found to provide the most robust information for the task. The threshold value was automatically selected by using Otsu's method (Otsu, 1979) that assumes that the image contains foreground (object) and background pixels, and calculates an optimal threshold so that the intra-class variance is minimal.

The resulting binary image typically contains noise. To eliminate the noise, connected components (connected regions of the foreground pixels) were determined and the components smaller than 10% of the predefined minimum droplet area were removed. The resulting binary images were further processed with morphological erosion using a small structuring element to remove small irregularities in the droplet edge regions. The structuring element is a binary area where black pixels (0 pixels) are excluded, and white pixels (1 pixels) are included in the morphological computation. After this step, the binary images contained at least fragments of the droplet edges.

Depending on the concentration, some of the detected regions contained holes. Moreover, with some concentrations the droplet edges were only partly visible.

To obtain full contours of the droplets, fitting an ellipse to the binary image data was used. The ellipse fitting was selected based on an assumption that the shape of droplets is oblate spheroid which causes the droplets to have an elliptical shape in the images. The ellipse fitting provides a good estimate for the true contours of the droplets and produces more reliable droplet shape parameters than using only binary descriptors of the droplet region (Szpak et al., 2012). The limits for the ellipse parameters were used to control the droplets, which were processed further and the ones which were discarded if they did not meet the limits. The full image analysis pipeline is presented in Fig. 2. The image at the top left corner shows the region of interest (ROI) (the blue rectangle) used for processing. ROI was manually selected after visual inspection of the videos to contain all the droplets moving with minimum processing area.

The basic image processing pipeline from the beginning to the ellipse fitting step was the same for the both imaging sources. After this, different feature extraction operations were performed for the Canon Legria HF R47 videos (size, velocity, and acceleration measurements) and the AVT Oscar videos (size and concentration analysis). Velocity and acceleration of the droplets were not determined from AVT Oscar videos since the lower frame rate, only 3 or 4 captured images from one moving droplet, did not allow

accurate measurements. Features extracted from the Canon Legria HF R47 videos included the minor and major axis lengths, orientation, velocity, and acceleration of the droplet. The ellipse minor and major axis lengths are

$$d_{\text{minor}}|d_{\text{major}} = \left[\frac{2(AE^2 - BDE + CD^2) - 4ACF + FB^2}{(4AC - B^2)(A + C) \pm \sqrt{(A - C)^2 + B^2}} \right]^{\frac{1}{2}} \quad (2)$$

where $|$ denotes the logical or (disjunction) operator (the greater of the two values given by the equation is the major axis) and $A, B, C, D, E,$ and F are the parameters of the general quadratic curve,

$$Ax^2 + Bxy + Cy^2 + Dx + Ey + F = 0, \quad (3)$$

(Weisstein, 2016). These parameters were obtained using the ellipse fitting. The velocity was calculated from the movement of the droplet center point between the consecutive frames and the acceleration as the difference in velocities between the consecutive frames.

In order to convert the pixel values of the features into the real world values (millimeters), the cameras were geometrically calibrated. To calibrate the camera, a sequence of images with a 5 mm grid was captured to provide the points of reference. The calibration was performed using the methods presented in (Heikkila and Silvén, 1997; Zhang, 2000). The process included detecting the grid from the image sequence and calculating the pairwise distances of grid lines. The collected information was used to form corrected, distortion free images. The pixel size in mm was obtained by dividing the real world grid size (5 mm) with the average distance for adjacent grid lines in images.

The concentration calculations were performed using the absorbance in the red color channel as explained in Section 2.5. The droplet geometry was taken into account by making chord length calculations assuming that the shape of droplets was oblate spheroid. This geometry was calculated from the parameters of the fitted ellipse. 15% of the droplet image area, the outer edge region of the droplet, was excluded from the concentration analysis since the light scattering at the droplet phase boundary caused problems when calculating the concentrations. Simplified process flow of the concentration analysis is shown in Fig. 3. Image analysis steps were implemented using MATLAB (2016a). The concentration analysis is described in more detail in Section 2.5.

2.5. Concentration analysis

The concentration analysis inside a droplet is based on the observation of image intensity change inside the sample. The concentration analysis is possible with imaging because of color change, which takes place when copper is complexed with hydroxyoxime. This color change is observed from the video recording of moving droplets by a digital camera.

The spectra recorded with the spectrophotometer revealed that free hydroxyoxime and its copper complex absorb light at different wavelengths (Fig. 4). The highest wavelength at which the free extractant absorbs light is approximately 400 nm whereas the copper complex absorbs also at longer wavelengths. The complex has a wide absorption peak with the absorption maximum at approximately 680 nm. The concentration analysis of organic phase samples with the UV/VIS-spectrophotometer (Agilent 8543) was made at the wavelength of 600 nm. The wavelength of 811 nm was used for the aqueous copper sulfate solution concentration analysis.

The concentration analysis with both the spectrophotometer and the cameras are based on the Lambert-Beer law. The Lambert-Beer or Bouguer-Beer law describes how, in a transmission measurement, the light intensity decreases as a function of the sample concentration and light path length. Each recorded

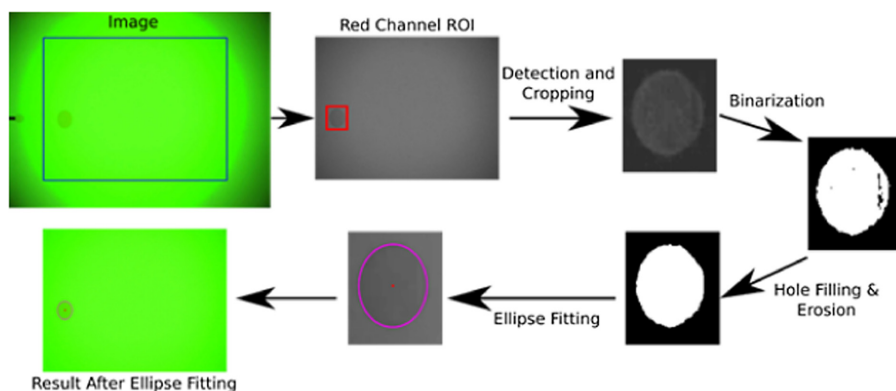


Fig. 2. Image analysis steps for determining the droplet movement, size and concentration. Contrast of the color images on the top row and the difference image has been enhanced for visualization purposes.

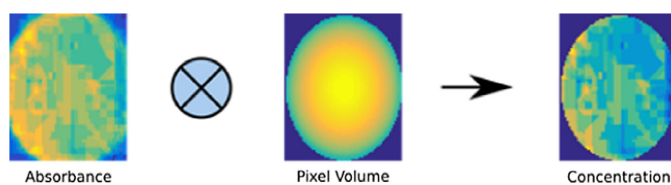


Fig. 3. Simplified process flow of the concentration analysis. The 'logical and'-symbol is used to represent the major contributing factors (absorbance and volume) to the concentration determination in simplified form.

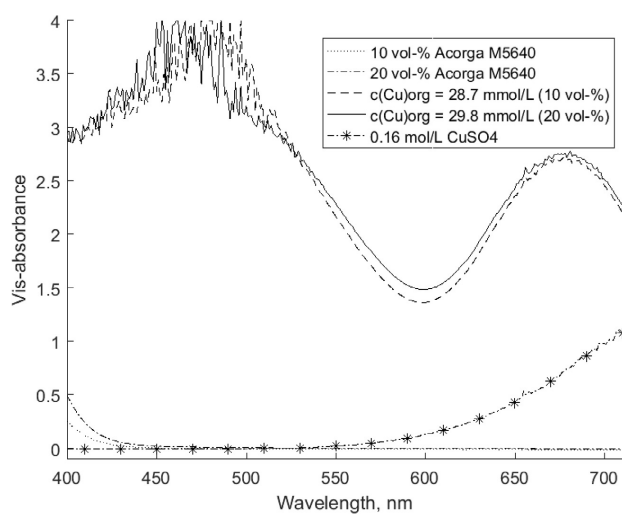


Fig. 4. The basis for detecting the copper complex. The red channel of camera is most sensitive for wavelengths from 550 nm to 700 nm. The visible-range spectra of organic Acorga M5640 solutions dissolved into Exxsol D80 and aqueous copper sulfate solution.

pixel of the droplet image represents a part of droplet. These droplet parts have a volume, here called as the pixel volume. The concentration in the pixel volume may not be uniform along the droplet chord (perpendicular to the image plane) as droplets were imaged only from a single direction. Uniform concentration was assumed for each pixel volume. The Lambert-Beer law and its derivation are presented and discussed by Berberan-Santos (1990), Goldstein and Day (1954) and Liebhaftsky and Pfeiffer (1953) and Denney and Sinclair (1987). The Lambert-Beer equation is presented as

$$A = \varepsilon Lc \quad (4)$$

where ε is molar absorptivity, L the optical path length, c is concentration and A is the absorbance:

$$A = \log_{10}(I_0/I) \quad (5)$$

that is, the logarithmic ratio of light intensity transmitted through the sample (I) and incoming light intensity (I_0).

The camera used for the concentration analysis (AVT Oscar F-510C) is a RGB camera with 8-bit channels. The approximate range, where red channel of the camera detects light, is 550–700 nm (Fig. 4). The red channel was found to be specific only for the copper complex of extractant, and not for the uncomplexed extractant. It is also noted that copper sulfate absorbs light at the wavelength range of the red channel. The red channel background is assumed to be constant, as the continuous phase volume is much higher compared to the droplet volume and thus the amount of copper and the copper concentration in the continuous phase remains practically constant during an experiment.

The camera records incoming light intensity and encodes the intensities as pixel values in the range of 0–255 (8 bits). The pixel values are assumed to be linearly dependent on the incoming light intensity within the usable dynamic range of the camera. Analogous to Eq. (5), absorbance is determined by:

$$A = \log_{10}(p_0/p), \quad (6)$$

where the incoming light intensity is represented by the pixel value p_0 and the light transmitted through the sample with the pixel value p (compare to Eq. (5)).

The camera records a droplet as it moves through the column. The spatial uniformity of the light source is even, and the pixels of the camera are assumed to be identical. Both droplet and background are visible simultaneously in recorded images, and thus the situation is similar to the double-beam spectrophotometer where the light beam is divided into two beams, and one travels through the sample and another through the solvent (i.e., background) (Mann et al., 1974). As the background of the image, i.e., the continuous phase, absorbs light also in the red channel used for the concentration analysis, the background is corrected by subtracting the background absorbance (A_{bg}) from the absorbance of the droplet image (A_d):

$$A = A_d - A_{bg}. \quad (7)$$

The droplet concentration can be calculated from absorbances, when droplet geometry is taken into account. The optical path length, i.e., the distance which light travels in a sample effects absorbance as it can be seen from the Lambert-Beer law (Eq. (4)). The chord lengths of the droplet at each pixel position were calculated by assuming that the droplet was oblate spheroid and that the axis normal to the image plane is equal to the measured major axis length.

The effect of light scattering was determined by calculating molar absorptivities (ε) for each pixel of single droplet image using the Lambert-Beer law (Eq. (4)). The absorptivities are shown as a function of calculated chord lengths in Fig. 5b. The edge of a droplet is darker than the rest of the droplet, which is due to light

refraction and scattering. The apparent absorptivity increases towards the droplet edge and it includes both the effect of light absorption due to the copper complex and the effect of scattering. While there are correlations for the light intensity changes due to scattering (Gumprecht and Sliepcevich, 1953), the use of apparent absorptivity was chosen for this work, as the present camera detects a wide range of wavelengths. The applied interpolation function for the apparent absorptivity was

$$\varepsilon = 3.786 \times 10^{-3} / \ln(l_{ch} + 1) + 0.8977 \times 10^{-3}, \quad (8)$$

where l_{ch} is the chord length. The function parameters were fitted to the droplet data and the function was used in the calculation of concentration profiles and the average concentrations of the droplets.

When the optical path length of the Lambert-Beer law (L in Eq. (4)) is set equal to the calculated chord length and the absorptivities are calculated with Eq. (8), the concentrations at the positions of the pixels (c_p) can be calculated from the image data based absorbances and the Lambert-Beer law (Eq. (4)):

$$c_p = A / \varepsilon l_{ch} \quad (9)$$

The calculated chord lengths (l_{ch}) together with the image scale, i.e., the distance per pixel (l_p), are used when the representative volume of each pixel is calculated:

$$V_p = l_p^2 l_{ch}, \quad (10)$$

where l_p is the distance per pixel. The amount of copper (n_p) at the position of each pixel, can be calculated from the volume and the measured concentration of the pixel:

$$n_p = c_p V_p \quad (11)$$

When the sum of the values of n_p of the whole droplet image is determined, the amount of copper transferred into the droplet can be calculated with

$$n = \sum_{i=0}^{d_{major}} \sum_{j=0}^{d_{minor}} n_p(i, j) \quad (12)$$

where i and j are indices of pixel location along the droplet image axes.

The average concentration of copper transferred into the droplet is

$$c = n / V_d, \quad (13)$$

where V_d is the droplet volume. The organic phase copper concentration is presented as a conversion of extractant, as organic feed solution includes the extractant and no copper.

The conversion (X) of extractant (HA) is calculated (Levenspiel, 1999) by:

$$X_{HA} = 1 - c_{HA} / c_{HA,0} \quad (14)$$

The extractant concentration is calculated using the extractant mass balance:

$$c_{HA} = c_{HA,0} - 2c \quad (15)$$

Copper reacts with two extractant molecules to form the complex, as also it can be seen from the reaction (Eq. (1)).

The calibration standards (see Fig. 5a) for the single droplet experiments were imaged as droplets in the column. The apparent molar absorptivity was calculated for each pixel of a one droplet image ($c_{Cu_{org}} = 25.4$ mmol/L). The interpolation function (continuous line) and ε obtained from droplet center data (dotted line) in Fig. 5b are also shown. The continuous line represents the interpolation function of apparent molar absorptivity and the dotted line denotes the value of ε obtained from the fit. The scattering is at minimum at droplet center, as can be seen from Fig. 5b.

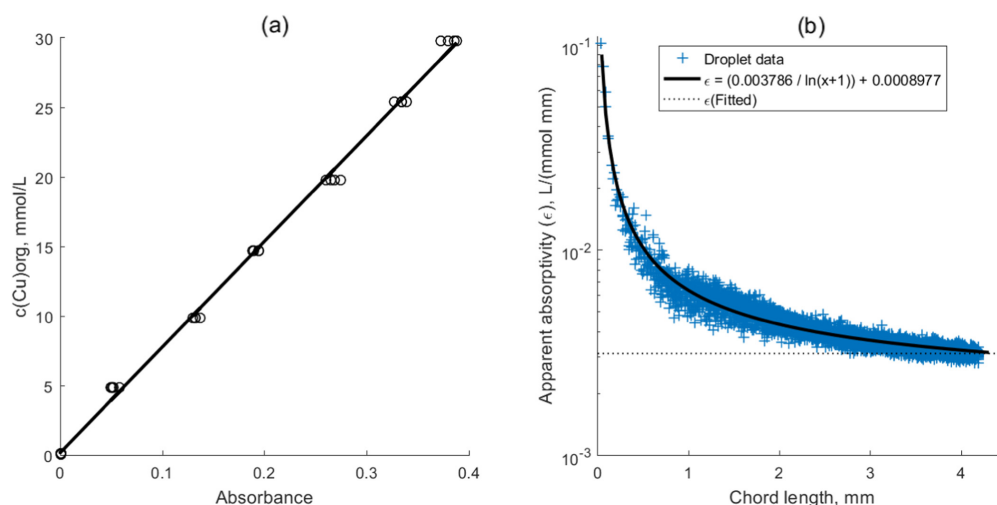


Fig. 5. The calibration of copper complex concentration for organic phase droplet image analysis with the AVT Oscar F-510C camera. (a) The fitted calibration line for droplet center data and (b) the effect of light scattering due to droplet interface curvature on molar absorptivity.

The calibration standard solutions of 20 vol% Acorga M5640 containing different copper concentrations were measured from the 0.8 mm needle tip using the aqueous copper sulfate solution (0.16 mol/L) as the continuous phase. The calibration line (Fig. 5a) was computed based on the center region of the droplets where the effect of light scattering is minimized. The copper complex standard solutions of 10 vol% Acorga M5640 in 0.06 M CuSO_4 continuous phase were measured for the comparison and verification purposes. The organic standard solutions were pumped ($\dot{V} = 1.5$ mL/min) through the needle into the column filled with the copper sulfate solution. The copper concentration in organic standard solution was varied between 0 and 30 mmol/L. The standard solution analysis with the spectrophotometer revealed that calibration lines of the both extractant concentrations were essentially the same.

The similar observations can be seen in Fig. 6, where samples with known copper concentrations were analyzed. The concentration in the droplets was analyzed using the same method and the calibration line as in the actual column experiments. The results at two different extractant concentrations are overlapping, indicating that also in the image analysis the calibration lines are practically the same.

Each droplet was detected several times from the subsequent video frames. The median value of these separate detections was used as the representative value for the droplet. The subsequent droplets are here considered as repetitive measurements. The χ^2 goodness of fit test for the normality was performed. The χ^2 test was passed in the case of elliptical droplet major and minor axis lengths, velocity, and concentration, that is, the data is normally distributed. Standard deviation of each dataset was chosen as the basis for quantifying variation in the measurement data. The measure for the error in this work is three times dataset standard deviation. The errors are approximately 1% for the droplet minor and major axis lengths, approximately 3% for the droplet velocity and approximately 22% for the droplet concentration in mmol/L (Fig. 7). The measured data is shown as frequency histograms and the calculated normal distributions as lines. The parameters

of the normal distribution were estimated based on the data. The data analysis was performed using MATLAB (2016a).

The theoretical detection limit for the proposed method is estimated by assuming that copper complex concentration in the droplet is uniform. The smallest possible detectable concentration change corresponds to pixel value p change from 255 to 254. Then the absorbance is 1.7×10^{-3} . The concentration can be calculated from this using the calibration line (Fig. 5). Thus, the smallest detectable concentration is approximately 0.15 mmol/L. The method accuracy and reproducibility are presented in Fig. 6. The method reproducibility (i.e., the distribution width of the measured data at each standard solution concentration) is approximately 2 mmol/L. The accuracy of method is defined as the difference between the average of the measured data and the nominal standard solution value. The accuracy of method may be possible to improve since there are some differences between the measured and nominal concentrations (the line in Fig. 6). The method standard line is linear in the concentration range 0–30 mmol/L (Fig. 5a).

The instrument bandwidth affects recorded absorbance values (Denney and Sinclair, 1987). In case of the spectrophotometer, the spectra was recorded with interval of 1 nm. The absorbance peak of complex is at least 150 nm wide (see Fig. 4) and the ratio of instrument and sample spectral bandwidths are below 0.01 in case of the spectrophotometer. The bandwidth of the red channel of the camera is close to 150 nm. The ratio of the instrument and sample spectral bandwidths is thus approximately 1.

3. Results and discussion

3.1. Analysis method

The camera calibration line forms a straight line (see Fig. 5a). Thus the Lambert-Beer law is obeyed also in determining the concentration from the droplet image data. The molar absorptivity coefficients obtained for the 10 vol% and 20 vol% Acorga standard

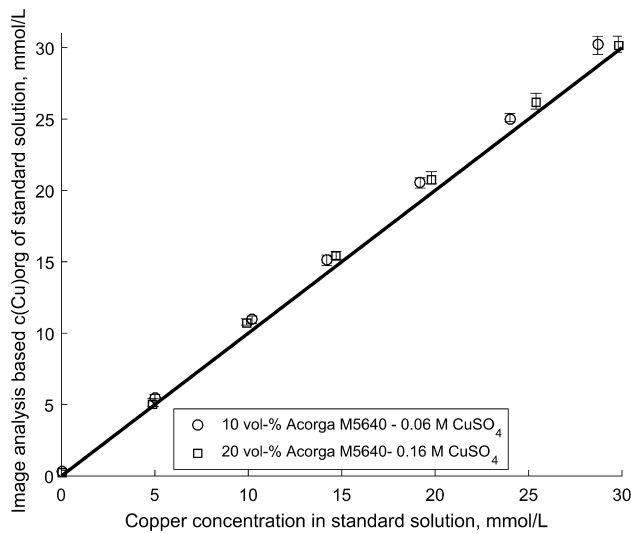


Fig. 6. Comparison of known standard solution concentrations and concentrations from image analysis. Mean of measured data (symbols) and variation of data (error bars) are shown. Nominal values (line) are shown for comparison purposes.

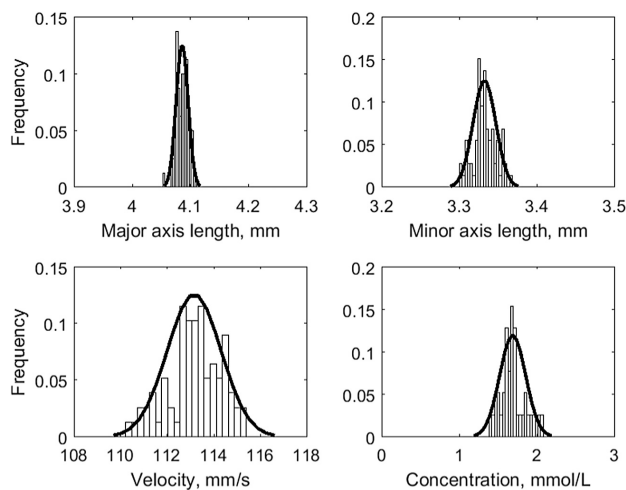


Fig. 7. The example distributions of measured droplet sizes, velocities, and concentrations. The histograms represent the measured data distributions and the lines denote normal distributions whose parameters are estimated from the data. The width of normal distribution is ± 3 standard deviations. The average and standard deviation were estimated from data.

solutions using the spectrophotometer at the wavelength of 677 nm, are 9.62×10^{-3} and 9.43×10^{-3} L/(mmol mm), respectively ($L = 10$ mm). The coefficients are nearly identical. For that reason, the only species present, which absorbs light at 677 nm, is the copper complex. The corresponding estimated absorptivities

at the droplet center for the camera (AVT Oscar F-510C) were $3.4 \times 10^{-3} \pm 0.2 \times 10^{-3}$ L/(mmol mm) for the 10 vol% Acorga solutions and $3.2 \times 10^{-3} \pm 0.2 \times 10^{-3}$ L/(mmol mm) for the 20 vol% Acorga solutions. The optical path length (L) was taken to be equal to the droplet major axis length in the calculations. The measured

major axis lengths were 4.2 ± 0.1 mm in the case of 10 vol% Acorga standards and 4.1 ± 0.2 mm in the case of 20 vol% Acorga standard solutions (see also Fig. 10).

The observed absorptivities of the 10 and 20 vol% standard solutions are almost identical also in the case of droplet image analysis. The complex absorbs light at the wavelength range of the red channel. The background was constant in each case and was subtracted from the images. The observed absorptivities were lower for the camera due to the wider spectral bandwidth. The similarity of absorptivities implies that the mass transfer during droplet formation was indeed minimal.

The effect of scattering due to droplet interface curvature was taken into account by calculating molar absorptivities for each pixel of standard solution droplet (Fig. 5b). The apparent molar absorptivity includes both the effect of copper complex light absorption and the effect of light scattering. The apparent absorptivity was assumed to depend only on the chord length, but the variation in the droplet data is notable. The interpolation function was fitted to the droplet data and it was used in the calculation of droplet copper concentrations. The interpolation function gives apparent absorptivity of 3.2×10^{-3} L/(mmol mm) at the droplet center ($L = 4.1$ mm), which is identical to the absorptivity obtained by fitting to all different concentrations. The difference between the continuous and dotted line in Fig. 5b indicates the effect of scattering. Scattering is minimal at the droplet center and increases towards the droplet edge.

It is acknowledged that copper can be transferred into the standard solution during droplet formation in the calibration experiment. The average formation time of droplets was estimated to be approximately 1.3 s. Due to the short formation time, the effect of mass transfer during the droplet formation with the standard solution is estimated to be approximately 0.3 mmol/L. This is within the variation in the analyzed concentrations of standard solutions. The estimation was made by extrapolating measured data from column bottom experiments, which contain mass transfer from droplet formation (see Fig. 8 and Table 1). The fitted extrapolation power function was used to calculate concentration at flow rate of 1.5 mL/min.

3.2. Concentration analysis

The present method determines organic phase copper complex concentration in the droplet. The results are presented as an extractant conversion and they are shown in Fig. 8. The conversion based on sample analysis (C_{sample}) taken from the column outlet funnel are clearly higher than based on the droplets imaged at the top (C_{TOP}) and bottom of the column (C_{BOT}) (see Table 1). Results from bottom of column show mass transfer during droplet formation, while results from column top include also mass transfer during droplet rise. The difference between column top and bottom analyses, reveal mass transfer during droplet rise (see also Fig. 8b). Samples include mass transfer during droplet formation, rise and column outlet funnel.

The high concentrations in the analyzed samples are due to long residence times at the column outlet. The average sample residence times at column outlet varied from 60 s to 420 s. It is acknowledged, that the sample concentrations are high and that sampling can be optimized. However, the purpose of this work is to present direct method for determining droplet inner concentrations and sample concentrations were determined for comparison purposes. Also noteworthy is the variation between the samples at high feed flow rates (over 0.3 mL/min) compared to the variation from direct droplet analysis.

The imaging of a droplet at the column top was made just prior it enters the column outlet funnel and imaging at the column bot-

Table 1
Measured average droplet concentrations at column top and bottom (C_{TOP} and C_{BOT}), concentration change during rise (ΔC_{Rise}) and collected sample direct analysis (C_{Sample}).

\dot{V} mL/min	C_{TOP} mmol/L	C_{BOT} mmol/L	ΔC_{Rise} mmol/L	C_{Sample} mmol/L
0.1	5.3	5.3	0.0	29.9
0.3	2.4	1.7	0.6	21.5
0.5	2.1	1.0	1.1	24.5
0.7	2.1	0.7	1.4	28.5
1	2.3	n.d.	2.3	24.9

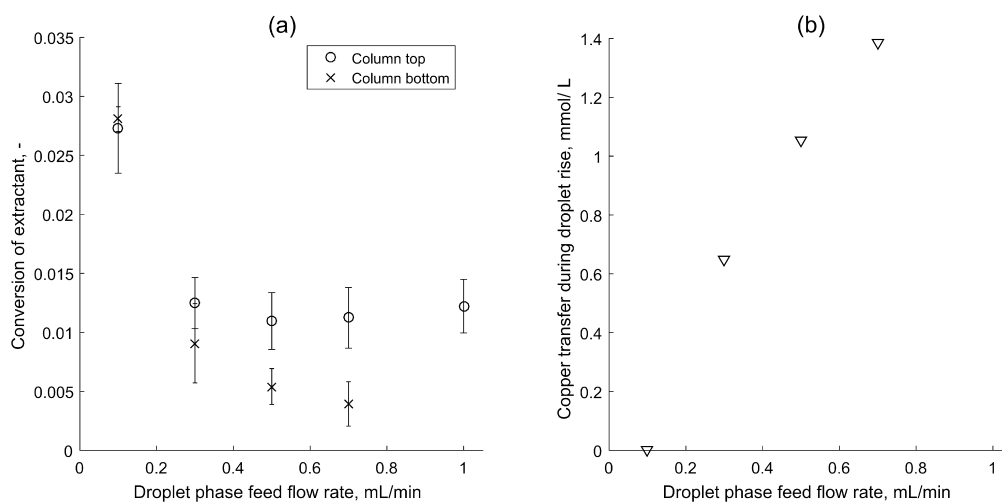


Fig. 8. Copper complex concentration change in column experiments. (a) Conversion of extractant to copper complex. (b) Copper complex concentration change during droplet rise.

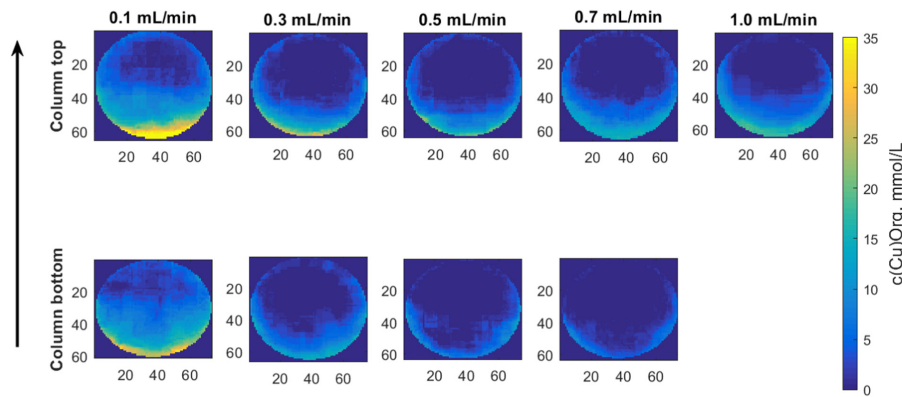


Fig. 9. Examples of determined copper organic phase concentration profiles inside droplets. Separate measurements were made for moving droplets at the column top (top row) and column bottom (bottom row). The arrow indicates the direction of droplet movement. Axis units are pixels.

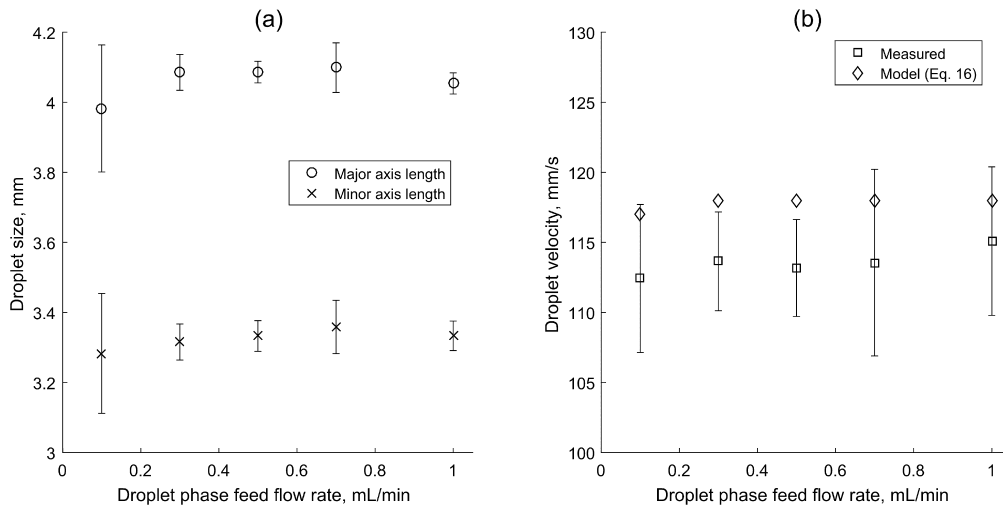


Fig. 10. The droplet sizes and velocities measured at the top of the column with organic feed flow rates 0.1–1.0 mL/min. Data is from Canon Legria HF R47. (a) The measured droplet minor and major axis lengths, (b) The measured and estimated terminal velocities of droplets.

tom was made just after a droplet detached from the needle tip. These two positions were measured in separate experiments. Comparison of the column bottom and column top measurements reveals that the majority of copper is transferred during the droplet formation. When the flow rate increases, copper transfer during the droplet formation decreases rapidly as the droplet formation time decreases. The droplet formation time is approximately 17 s at 0.1 mL/min and it decreases below 2 s when the flow rate is 1.0 mL/min.

The copper mass transfer during the rise increases as the droplet feed flow rate increases (see Fig. 8b). The droplet sizes and the measured velocities of droplets are approximately constant (see Figs. 9 and 10) and the rise time does not vary significantly

and cannot explain the difference because the rise length remains constant. Possible explanation is that, the concentration difference between droplet and continuous phase increases as a function of flow rate, due to decreasing mass transfer during droplet formation (see Fig. 8 and Table 1). This leads to observed increased mass transfer during droplet rise.

For determining droplet concentration profiles, droplets were imaged at the bottom and the top of the column, and the concentrations were calculated from the recorded video images (see Fig. 9). The shown droplet images represent examples of droplets at the top and bottom positions of the camera. The highest copper concentrations are found near the droplet interface, which is due to interfacial complexation of copper and limited interaction time for

mass transfer. The concentrations at the droplet bottom tend to be higher than at the top. The explanation for this is not clear, but a possible reason is the density difference between the extractant and copper complex because the loaded extractant is heavier. Another possible reason is the circulatory flows at both sides of the droplet phase boundary. One possible explanation for the observed concentration distribution inside the droplets is the uneven distribution of surfactants. According to Slater (1995), surfactants have a tendency to concentrate in the droplet lower part and to stop internal circulation. In this stagnant cap model the droplet upper part, having lower surfactant concentration, has a mobile interface leading to circulation and reducing concentration differences.

The effect of decreasing the formation time can be observed in Fig. 9 as the concentrations decrease from left to right. The effect is especially clear in the case of observations from the column bottom. The effect of mass transfer during the droplet rise can be seen by comparing images taken at the top and the bottom of the column with the same flow rate. The images recorded at the top of the column show higher concentrations. Comparison of the images is straightforward, as the droplet sizes are approximately equal.

3.3. Droplet sizes and velocities

Fig. 10 shows measured droplet sizes and measured and estimated droplet velocities. Terminal velocities were calculated by using Eq. (16). Data was obtained by image analysis of videos recorded by Canon Legria HF R47.

The droplet sizes are similar in all experiments (Figs. 9 and 10), which is due to identical solution properties and the same needle gauge used in the droplet formation. The increase in feed flow rate of the droplet phase from 0.1 to 1.0 mL/min had no significant effect in the drop sizes.

Droplet velocities were determined at the top of the column and like droplet sizes, velocities are also close to each other. They varied between 112 and 115 mm/s (Fig. 10b). To validate the velocity measurement, correlation by Grace et al. (1976) was used. This correlation is for systems where, for example, surfactants are present as contaminants and correlations for pure systems are not usable. Their correlation for droplet terminal velocity is

$$u_t = \mu_c / (\rho_c d_c) \text{Mo}^{-0.149} (J - 0.857) \quad (16)$$

with

$$J = 0.94H^{0.757}, \quad 2 < H \leq 59.3 \quad (17)$$

and

$$J = 3.42H^{0.441}, \quad H > 59.3 \quad (18)$$

and H defined as

$$H = 4/3\text{EoMo}^{-0.149} (\mu_c/\mu_w)^{-0.14}, \quad \mu_w = 0.9 \text{ mPa s} \quad (19)$$

where μ_c and ρ_c are continuous phase viscosity and density, d_c volume equivalent sphere diameter, Mo is Morton number and Eo is Eötvös number. The property values for the 20 vol% Acorga and 0.16 mol/L CuSO_4 -solution pair at room temperature were $\rho_c = 1025 \text{ kg/m}^3$, $\rho_d = 834 \text{ kg/m}^3$ and $\gamma = 22 \text{ mN/m}$. Copper sulfate solution density was interpolated from literature values (Lobo, 1981) and interfacial tension was measured using the drop weight method (Adamson, 1990). Using average droplet major and minor axis lengths $\bar{d}_{\text{major}} = 4.0 \text{ mm}$ or 4.1 mm and $\bar{d}_{\text{minor}} = 3.3 \text{ mm}$ (see Fig 10a), volume equivalent sphere diameters d_e are 3.76 and 3.81 mm. With given physical property values Mo and Eo numbers are $0.242 \cdot 10^{-9}$ and 1.36 and terminal velocities u_t , using Eqs. (16)–(19) are 117 and 118 mm/s, which agree well with the measured droplet velocities.

Based on the measurements, the droplet aspect ratio $E = \bar{d}_{\text{minor}}/\bar{d}_{\text{major}}$ is between 0.80 and 0.83. Grace et al. (1976) have presented a correlation for the droplet aspect ratio

$$E = 1/(1 + 0.163\text{Eo}^{0.757}), \quad \text{Mo} < 10^{-6}, \quad \text{Eo} < 40 \quad (20)$$

Using $\text{Eo} = 1.36$, the estimated aspect ratio is 0.83 which corresponds well with the observed aspect ratios. To determine the droplet shape region, diagram presented by Grace et al. (1976) is used. With droplet Eötvös number 1.34 and Morton number $0.242 \cdot 10^{-9}$ the shape region is ellipsoidal which is confirmed from droplet observations.

In addition to surfactants, the droplet size and form have an effect on the terminal velocities. The droplet size defines the mass transfer area, and the droplet velocity affects internal circulation in the droplet and the diffusion layer thickness. The changes in velocity lead to differences in the diffusion layer thickness and wake outside the droplet. The properties of the diffusion layer and circulation both inside and outside the droplet, have an effect on the mass transfer during extraction. The velocity of the droplet affects the rise time of the droplet. Both the droplet size and velocity are measured in order to differentiate between the mass transfer during droplet formation and rise.

4. Conclusions

The presented method was developed for direct monitoring of single organic phase droplets and their reactive copper extraction in a glass column. The developed method is based on the observation of droplet color change, which is due to the formation of strongly light absorbing copper-hydroxyoxime complex. It was verified against reference samples which were analyzed using spectrophotometry. The method can be used to detect droplet concentration directly inside the column from any position where the droplet is visible. This enables monitoring of mass transfer into a single rising droplet in the column, which can be done in separate experiments or in a single one using several cameras.

In this paper the problematic concentration analysis using the traditional sample collection has been performed for comparison purposes, and the advantages of the direct image analysis based method has been presented. The method enabled the determination of individual effect of droplet formation, droplet rise and sample collection on copper mass transfer. The effect of sample collection is most notable due to the long residence time of the droplet phase at the column outlet. The droplet formation has a notable effect on copper mass transfer at low feed flow rates, due to long droplet formation times. The image analysis method also enabled characterizing the shape of droplets, by determining the droplet minor and major axis lengths. There was a good agreement with measured and estimated droplet velocities.

The developed method can be improved in several ways. For example, when a more sensitive camera with a wide dynamic range and improved conversion to digital intensity values is used, a wider range of concentrations can be measured and with better signal-to-noise ratio. Calculation of optical paths and modeling the light scattering at the outer edge region of the droplet would possibly allow inclusion of the edge region into the concentration analysis. One possible way could be to add additional camera(s) at different angle(s) to determine the light scattering and optical properties of the edge region. Different light sources could also be considered, when determining the effects of the light scattering at the outer edge region of the droplet. While the present work is designed for copper solvent extraction, the same method can be used in any metal-extractant pair, where the color change in extraction is large enough for the imaging. This method is by no means limited to metal extraction substances, but it can be applied

also to other systems, where a suitable color change is present. It is also possible to limit the observation bandwidth by installing special filters onto the camera optics. The camera red channel was used here, but present method is not limited to specific color channel. Depending on application, it may be possible to use different channels in detection of different reactive species. On the other hand, it is also possible to change the spectral characteristics of the illumination used and even use laser illumination. The method is not limited to the visible light, assuming that the camera sensor is sensitive to and the optics is suitable for other wavelengths, such as ultraviolet light or infra-red.

Acknowledgements

The authors gratefully acknowledge the Academy of Finland (project "Analysis of polydispersity in reactive liquid-liquid systems") for financial support.

References

- Adamson, A.W., 1990. *Physical Chemistry of Surfaces*. Wiley, New York, USA.
- Bart, H.-J., Stevens, G.W., 2004. Reactive solvent extraction. In *Ion exchange and solvent extraction. A Series of Advances* 17, 37–83. CRC Press.
- Baumann, K.-H., Mühlfriedel, K., 2002. Mass transfer studies with laser-induced fluorescence across liquid/liquid phase boundaries. *Chem. Eng. Technol.* 25 (7), 697–700.
- Berberan-Santos, M., 1990. Beer's law revisited. *J. Chem. Educ.* 67 (9), 757–759.
- Biswas, R.K., Haniif, M.A., Bari, M.A., 1996. Kinetics of forward extraction of manganese(II) from acidic chloride medium by D2EHPA in kerosene using the single drop technique. *Hydrometallurgy* 42 (3), 399–409.
- Biswas, R.K., Habib, M.A., Bari, M.F., 1997. Kinetics of backward extraction of Mn(II) from Mn-D2EHPA complex in kerosene to hydrochloric acid medium using single drop technique. *Hydrometallurgy* 46 (3), 349–362.
- Cheung, S.-C.S., Kamath, C., 2005. Robust background subtraction with foreground validation for urban traffic video. *Eurasip J. Appl. Signal Process.* 2005 (14), 2330–2340.
- Denney, R.C., Sinclair, C., 1987. *Visible and Ultraviolet Spectroscopy*. John Wiley & Sons, Chichester.
- Goldstein, J.H., Day Jr., R.A., 1954. A kinetic interpretation of the Bouguer-Beer law. *J. Chem. Educ.* 31 (8), 417–418.
- Grace, J.R., Wairegi, T., Nguyen, T.H., 1976. Shapes and velocities of single drops and bubbles moving freely through immiscible liquids. *Trans. Inst. Chem. Eng.* 54 (3), 167–173.
- Gumprecht, R.O., Slipecevic, C.M., 1953. Scattering of light by large spherical particles. *J. Phys. Chem.* 57 (1), 90–95.
- Hanna, G.J., Noble, R.D., 1985. Measurement of liquid-liquid interfacial kinetics. *Chem. Rev.* 85 (6), 583–598.
- Heikkilä, J., Silván, O., 1997. Four-step camera calibration procedure with implicit image correction. *IEEE International Conference on Computer Vision and Pattern Recognition*.
- Henschke, M., Pfennig, A., 1999. Mass-transfer enhancement in single-drop extraction experiments. *AIChE J.* 45 (10), 2079–2086.
- Kumar, A., Hartland, S., 1999. Correlations for prediction of mass transfer coefficients in single drop systems and liquid-liquid extraction columns. *Chem. Eng. Res. Des.* 77 (5), 372–384.
- Levenspiel, O., 1999. *Chemical Reaction Engineering*, vol. 3. John Wiley & Sons, New York, USA.
- Liang, T.-B., Slater, M.J., 1990. Liquid-liquid extraction drop formation: mass transfer and the influence of surfactant. *Chem. Eng. Sci.* 45 (1), 97–105.
- Licht, W., Conway, J.B., 1950. Mechanism of solute transfer in spray towers. *Ind. Eng. Chem.* 42 (6), 1151–1157.
- Licht, W., Pansing, W.F., 1953. Solute transfer from single drops in liquid-liquid extraction. *Ind. Eng. Chem.* 45 (9), 1885–1896.
- Liebhaufsky, H.A., Pfeiffer, H.G., 1953. Beer's law in analytical chemistry. *J. Chem. Educ.* 30 (9), 450–452.
- Lobo, V.M.M., 1981. *Electrolyte Solutions: Literature Data on Thermodynamic and Transport Properties*, vol. 1. University of Coimbra, Coimbra, Portugal.
- Mann, C.K., Vickers, T.J., Gulick, W.M., 1974. *Instrumental Analysis*. Harper & Row, USA.
- MATLAB Release 2016a. The MathWorks, Inc., Natick, Massachusetts, United States.
- Mörters, M., Bart, H.-J., 2000. Fluorescence-indicated mass transfer in reactive extraction. *Chem. Eng. Technol.* 23 (4), 353–359.
- Mörters, M., Bart, H.-J., 2003. Mass transfer into droplets undergoing reactive extraction. *Chem. Eng. Process.* 42 (10), 801–809.
- Otsu, N., 1979. A threshold selection method from gray-level histograms. *IEEE Trans. Syst. Man Cybern.* 9 (1), 62–66.
- Pawelski, A., Paschedag, A.R., Kraume, M., 2005. Beschreibung des Stofftransports am Einzeltröpfchen in Anwesenheit einer schnellen chemischen Reaktion mittels CFD-Simulation. *Chem.-Ing.-Tech.* 77 (7), 874–880.
- Schulze, K., 2007. *Stoffaustausch und Fluidodynamik am bewegten Einzeltröpfchen unter dem Einfluss von Marangonikonvektion* PhD Thesis. Technische Universität Berlin.
- Slater, M.J., 1995. A combined model of mass transfer coefficients for contaminated drop liquid-liquid systems. *The Can. J. Chem. Eng.* 73 (4), 462–469.
- Szpak, Z.L., Chojnacki, W., van den Hengel, A., 2012. Guaranteed ellipse fitting with the Sampson distance. Paper presented at *Computer Vision – ECCV 2012: 12th European Conference on Computer Vision, Florence, Italy*.
- Wegener, M., Paschedag, A.R., Kraume, M., 2009. Mass transfer enhancement through Marangoni instabilities during single drop formation. *Int. J. Heat Mass Transf.* 52 (11), 2673–2677.
- Wegener, M., Paul, N., Kraume, M., 2014. Fluid dynamics and mass transfer at single droplets in liquid/liquid systems. *Int. J. Heat Mass Transf.* 71, 475–495.
- Weisstein, E.W., *Ellipse*. From *MathWorld-A Wolfram Web Resource*. <<http://mathworld.wolfram.com/Ellipse.html>> (16. Dec. 2016)
- Whewell, R.J., Hughes, M.A., Hanson, C., 1975. The kinetics of the solvent extraction of copper(II) with LIX reagents—I single drop experiments. *J. Inorg. Nucl. Chem.* 37 (11), 2303–2307.
- Zhang, Z., 2000. A flexible new technique for camera calibration. *IEEE Trans. Pattern Anal. Mach. Intell.* 22 (11), 1330–1334.

Publication III

E. Lahdenperä, J. Tamminen, T. Koiranen, T. Kuronen, T. Eerola, L. Lensu,
H. Kälviäinen

Modeling mass transfer during single organic droplet formation and rise

Reprinted from *Journal of Chemical Engineering & Process Technology*, 9(2), 2018, DOI:
10.4172/2157-7048.1000378



Modeling Mass Transfer During Single Organic Droplet Formation and Rise

Esko Lahdenperä*, Jussi Tamminen, Tuomas Koironen, Toni Kuronen, Tuomas Eerola, Lasse Lensu and Heikki Kälviäinen

School of Engineering Science, Lappeenranta University of Technology, Lappeenranta, Finland

Abstract

Copper reactive extraction from ambient aqueous solution to organic droplets using single droplet experiments was performed. Extractant was Agorca M5640 hydroxyoxime in Exxsol D80. An image analysis based method was used to determine droplet concentration directly after droplet formation and rise. Mass transfer during formation is correlated using literature. Level Set interface tracking method was used to find formation hydrodynamics and as a result the assumption of non-circular velocity field could be validated. This was also supported by the circulation criteria based on needle Reynolds number. A model to estimate extraction rate as function of droplet Fourier number was based on a literature correlation and it was found that a model where the interface effect was described using interface mobility parameter was able to predict satisfactorily mass transfer. For a rising droplet stagnant cap model was used. Stagnant cap volumes were estimated from droplet images. A CFD model of a non-deforming rising droplet with rigid interface was used to fit interfacial reaction kinetic constant. Fitted value was much lower than experimentally determined by high a shear reactor. Mass transfer coefficients calculated from CFD model and estimated using literature correlations agreed well. By applying a two-film model it was shown that major part of the resistance is located at the interface between the phases.

Keywords: Mass transfer; Copper extraction; Liquid-liquid extraction; Mathematical model; CFD

Introduction

Single droplet experiment is a common method to determine mass transfer rates between the feeds in liquid-liquid extraction (LLE). During a single droplet experiment three stages are identified: (1) droplet formation, detachment and acceleration, (2) droplet rise/fall and (3) droplet coalescence [1]. In traditional experiments a droplet concentration are measured before formation and after coalescence and this provides an overall mass transfer rates for all stages. By using suitable experimental arrangements the effect of coalescence can be minimized but the droplet formation stage is often substantial [2-5] and by using several different droplet rise times the effect of formation is found by extrapolation of results into zero rise time.

This indirect method to determine the amount mass transfer during formation has some drawbacks. Application of the method requires several experimental points in order to get statistically relevant results. In this work this problem is avoided by using an image analysis based direct measurement method developed by Tamminen et al. [6] to measure concentrations directly from the column. This also simplifies experimental setup as there are no strict limitations for the coalescence stage arrangements.

Mass transfer correlations during droplet formation correlate the amount of extracted Δn or the extraction ratio E as a function of Fourier number $FO_d = 4D_m t_f / d_d^2$ [7-10]. Diameter d_d is volume equivalent sphere diameter after droplet formation. Those correlations assume that mass transfer inside the droplet is purely diffusion based. To take into account the intensifying effect of internal circulation and the hindering effect of surfactants, Liang and Slater [4] formulated overall effective diffusivity $D_{F,eff} = k_{H,E}(D_m + D_{E,F})$ where $D_{E,E}$ is time dependent diffusivity due to circulation. The empirical parameter $k_{H,F}$ takes into account the effect of surfactants. Depending on the interface properties, $k_{H,F}$ varies between 0 and 1. Liang and Slater [4] also propose a criterion based on the needle Reynolds number, whether there is circulation during droplet formation.

Kumar and Hartland [11] have published a collection of mass transfer correlations for a rising droplet. For the continuous phase correlations are expressed in form $Sh_c = f(Re, Sc_c, K)$ where K is viscosity ratio between dispersed and continuous phase. Droplet side correlations are based on Newman [12] model, which assumes no circulation. The intensifying effect of droplet internal circulation is taken into account by (1) using the effective diffusion coefficient D_{eff} which is D_m multiplied with a constant [12,13], (2) using eddy diffusivity D_e [14] or (3) combining eddy and molecular diffusivities into an effective diffusivity D_{eff} [15-17]. To take into account the effect of surfactants, Slater [18] applied the stagnant cap model where a droplet is divided into a circulating and stagnant regions. Effect of surfactants on interface mobility is implemented by using a similar experimental parameter $k_{H,R}$ as was used in droplet formation.

DNS (=Direct Numerical Simulation) method to solve transport equations can, in principle, provide parameters for the constitutive equations, like mass transfer coefficients. During droplet rise, if a droplet is smaller than the critical diameter then it maintains sphericity and it can be modelled as a sphere with constant shape and diameter. This approach has been used by Piarah et al. [19], Wegener et al. [20], Jeon et al. [21] and Pawelski et al. [22]. When a droplet is deformed due to diameter being larger than critical diameter, interface tracking offers a method to model the combined effect of hydrodynamics and interface evolution on mass transfer. A rising droplet interface tracking has been applied by, for example, Deshpande and Zimmerman [23],

*Corresponding author: Esko Lahdenperä, School of Engineering Science, Lappeenranta University of Technology, Lappeenranta, Finland, Tel: +35850553425; E-mail: Esko.Lahdenperä@lut.fi

Received March 27, 2018; Accepted April 02, 2018; Published April 20, 2018

Citation: Lahdenperä E, Tamminen J, Koironen T, Kuronen T, Eerola T, et al. (2018) Modeling Mass Transfer During Single Organic Droplet Formation and Rise. J Chem Eng Process Technol 9: 378. doi: [10.4172/2157-7048.1000378](https://doi.org/10.4172/2157-7048.1000378)

Copyright: © 2018 Lahdenperä E, et al. This is an open-access article distributed under the terms of the Creative Commons Attribution License, which permits unrestricted use, distribution, and reproduction in any medium, provided the original author and source are credited.

Yang and Mao [24], Kenig et al. [25] and Wang et al. [26] who all have used Level Set (LS) method. For the droplet formation, LS method is used by Lu et al. and Soleymani et al. [27,28]. Soleymani et al. however, model only droplet hydrodynamics during formation and rise and they do not calculate mass transfer.

When the classical two-film theory is used to describe mass transfer between two feeds LLE, it is assumed that two films having finite thickness is formed between the phases. The interface itself is assumed to have infinitely small width thus providing negligible mass transfer resistance [29]. However, the assumption of negligible interface thickness and resistance is questionable [30]. Hu et al. [31] modelled mass transfer in LLE using molecular simulation and according to their result, as a contrary to assumption used in two-film theory, the effect of the interface on the mass transfer cannot be neglected. Hu et al. also claim that the surfactants restructure the interface and the mass transfer mechanism is modified. An additional component to be considered is an interface reaction which in two-film theory is assumed to be a surface phenomenon and proceeding with the kinetics of its own. But according to Hu et al. the interface structure is complex and it can be assumed that the empirical parameters for reaction kinetic models determined, for example, in high shear mixers, are not usable because of missing interface effects.

In this study the focus is on mass transfer from continuous phase to organic droplet. Models of copper reactive extraction from aqueous phase into an organic droplet during droplet formation and droplet rise were formulated. Droplets were formed using 0.4 and 0.8 mm needles with several different feed rates. Droplet concentrations, diameters and velocities after the formation and in the end of the rise were measured with an image analysis method. The method is documented in the previous work by Tamminen et al. [6]. An empirical model of mass transfer in droplet formation is based on a methodology proposed by Walia and Vir [9] enhanced by Liang and Slater [4]. Results are compared with Popovich [7] model. The droplet formation hydrodynamics is simulated with CFD using LS method to provide support for the selected velocity profile during droplet formation.

Copper transport from aqueous continuous phase to the organic droplet during droplet rise was modelled with CFD using a stationary spherical droplet with non-deforming interface. The ambient aqueous phase is moving with the measured droplet terminal velocity. Stagnant cap model was implemented by dividing the droplet interface into two domains. Velocity boundary condition was used to adapt corresponding interface mobility to reflect stagnant cap properties. By assuming a fully rigid interface ($k_{HR}=0$) the reaction kinetic coefficient and extraction rate were estimated. Fractional mass transfer resistances were calculated from the film model.

Materials and Methods

Experiments

Experiments were made using same feeds, setup and method as in previous work by Tamminen et al. [6]. Results of previous work were extended here by using a smaller diameter needle (0.4 mm) in drop formation.

The droplet formation flow rates were 0.041, 0.21, and 0.29 mL/min in case of 0.4 mm needle and 0.10, 0.30, 0.50, 0.70 mL/min, when 0.8 mm needle was used. Needle Reynolds number Re_N was between 1-10. Droplet formation times were not explicitly measured. They were calculated based on feed rate and measured droplet volume.

Contact angles were measured from sessile droplets with 20 vol-% Acorga M5640 in Exxsol D80 (by Exxon). The aqueous phase was 0.16 M copper sulfate solution. The size of droplet and the height (h) of a sessile droplet from needle tip to droplet apex were measured. Contact angle is calculated from $\tan(\theta/2) = h/r_d$ [32]. Droplet image axes measured in x - and y -directions confirmed spherical droplet assumption. Estimated contact angle θ is 120° . Measured physical properties of 20 vol-% Acorga solution are shown in Tables 1 and 2.

Details of feed solution preparation, experimental arrangement, droplet imaging and analysis method are documented [6]. Local droplet concentrations were measured at the end of the droplet rise and just after the droplet detachment.

Mass transfer in droplet formation

Popovich [7] has presented a model to describe the total mass transfer during droplet formation:

$$\Delta n = a_1(c'_d - c_{d,0})\sqrt{\pi D_m t_f d_e^2} = a_1(c'_d - c_{d,0})\frac{de}{2}\sqrt{\pi Fo_d d_e^2} \quad (1)$$

Where c'_d is equilibrium concentration, $c_{d,0}$ is initial concentration and t_f is the formation time of a spherical droplet having volume equivalent diameter d_e . The model is based on assumption that the mass transfer process is diffusion controlled so interfacial instabilities and internal circulation is not taken into account. The constant a_1 varies between 0.857 and 3.43 [5].

In the model by Liang and Slater [4] the extraction ratio E is calculated with the model developed by Walia and Vir [8,9]

$$E = E_d - (7/8)E_d^2 + (49/72)E_d^3 - 0.476E_d^4 \quad (2)$$

Liang and Slater [4] define the term E_d as a function of modified Fourier number Fo'_d

$$E_d = \frac{36}{\sqrt{21\pi}} \frac{1}{2} \sqrt{Fo'_d} \left(1 + \frac{1}{2} \sqrt{\pi Fo'_d}\right) \quad (3)$$

Modified Fourier number Fo'_d uses overall effective diffusivity $D_{F,eff}$ instead of molecular diffusivity D_m . The overall effective diffusivity is defined as:

$$D_{F,eff} = k_{H,F}(D_m + D_{F,E}) \quad (4)$$

Where $k_{H,F}$ describes the effect of surfactant and has values between 0 to 1, and $D_{F,E}$ is pseudo-eddy diffusivity to take into account the effect of droplet internal circulation. Liang and Slater [4] propose a method to judge if system is (1) diffusion controlled $Re_N < 10$, or (2) circulation enhanced diffusion: $10 < Re_N < 34$, or (3) circulation controlled: $10 < Re_N > 34$. In a system with pure diffusion control, the diffusivity D_m is to be used. In cases 2 and 3 the enhancing effect of circulation on the mass transfer is taken into account using $D_{F,E}$.

Liang and Slater [4] considered only interfacial effects to be included in the constant $k_{H,F}$ but also other effects like the resistance generated by interfacial reaction can also taken into account [33,34].

Mass transfer during droplet rise

When a droplet is rising the mass transfer is affected by diffusion and internal circulation and also the outside convection as well. Depending on the interface mobility, the interface can be rigid or mobile and this has an effect on droplet internal circulation strength.

Correlations provided by the literature are mostly for systems without contaminations and surfactants [11]. Slater [18] has formulated

a model to take into account decrease of mass transfer rates due to surface effects and defines a correction factor $K_{H,R}$:

$$k_{H,R} = \bar{U}_i / U_t \quad (5)$$

Where \bar{U}_i is the average interfacial velocity and is U_t droplet terminal velocity.

The stagnant cap model for a rising droplet by Slater [18] is applied. The model is based on the concept of two zones, where one zone is stagnant and another zone is circulatory (Figure 1). Surfactants and other contaminants act against circulation and as a result the interface becomes more rigid [18].

A droplet is divided into two zones having relative sizes f_v and $1-f_v$, where f_v is size of the stagnant zone. An overall effective diffusivity is calculated based on f_v , molecular diffusivity D_m and eddy diffusivity $D_{R,E}$:

$$D_{R,eff} = f_v D_m + (1-f_v) (D_m + D_{R,E}) \quad (6)$$

Eddy diffusivity describes the effect of internal circulation on mass transfer and is calculated using Handlos and Baron Method [14]:

$$D_{R,E} = \frac{k_{H,R} U_i d_e}{2048(1 + \mu_o / \mu_c)} \quad (7)$$

It can be assumed that in this system the interface is rigid so $k_{H,R} = 0$. Droplet phase mass transfer coefficient is calculated using the model by Newman [12]. The overall effective diffusivity defined in eq. (7) is used here:

$$k_{CuA_2} = -\frac{d_e}{6t_R} \ln \left(\frac{6}{\pi^2} \sum_{z=1}^{\infty} \frac{1}{Z^2} \exp \left(-\frac{4z^2 \pi^2 D_{R,eff} t_R}{d_e^2} \right) \right) \quad (8)$$

This equation is valid for a case where the main mass transfer resistance is on the droplet side [18].

Stagnant zone size was estimated from droplet concentration distribution images. An example of concentration profiles in a rising droplet is shown in Figure 2. The average overall mass transfer coefficient K_d during droplet rise is:

$$K_d = -\ln \left(\frac{c_d^* - c_d}{c_d^* - c_{d,0}} \right) \frac{d_e}{6t_R} \quad (9)$$

Where t_p is droplet rise time and $c_{d,0}$ is droplet concentration after formation. This equation can be used as well to calculate mass transfer coefficient during formation. The time to use, then, is the droplet formation time t_f and $c_{d,0}$ is feed concentration which in most cases is zero [35].

CFD model for droplet formation

Droplet coalescence simulations were performed with Comsol Multiphysics v.5.2 [36] using LS method for two-phase laminar flows. A 2-d axisymmetric geometry was used. Geometry and boundary conditions are shown in Figures 3a and 3b. Two needle diameters were used: 0.8 mm o.d./0.51 mm i.d and 0.41 mm o.d and inner diameter 0.21 mm. Calculation domain dimensions were 3.8 mm width and height 10.2 mm. Same domain size was used for both needles.

A hemisphere having diameter of needle inlet was formed before calculations (Figure 3b). Initially both phase velocities and pressures were set to 0. The Comsol LS solver performs a steady state calculation at time $t=0$ to get consistent initial state for the transient calculation.

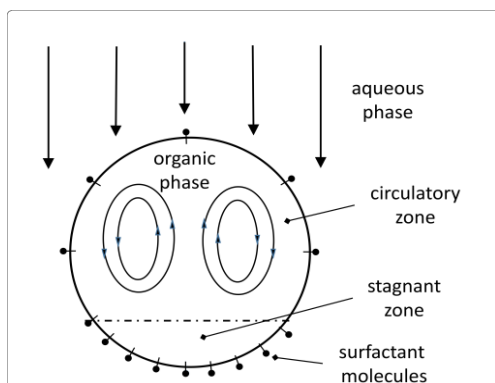


Figure 1: Description of the stagnant cap model of a rising droplet. Arrows describe the flow relative to a droplet.

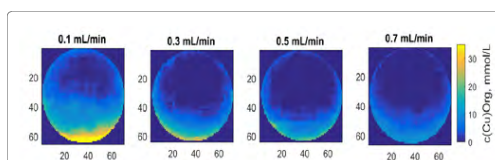


Figure 2: An example of measured concentration profiles of a rising droplet with different feed rates. Droplets are moving upwards (compare with Figure 1). The complex CuA_2 concentrations are higher in the droplet lower part thus supporting the stagnant cap assumption.

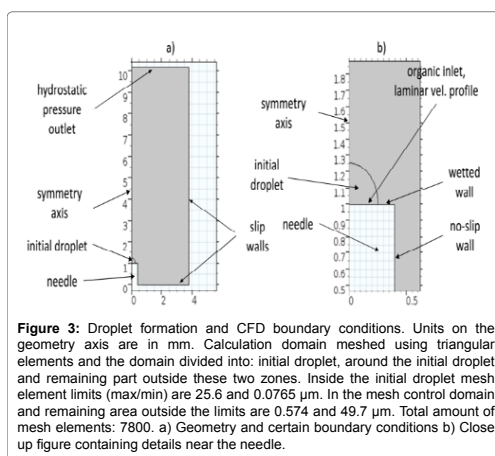


Figure 3: Droplet formation and CFD boundary conditions. Units on the geometry axis are in mm. Calculation domain meshed using triangular elements and the domain divided into: initial droplet, around the initial droplet and remaining part outside these two zones. Inside the initial droplet mesh element limits (max/min) are 25.6 and 0.0765 μm . In the mesh control domain and remaining area outside the limits are 0.574 and 49.7 μm . Total amount of mesh elements: 7800. a) Geometry and certain boundary conditions b) Close up figure containing details near the needle.

The default LS solver was used. Two user controllable LS parameters, reinitialization parameter and interface thickness parameter were adjusted to reach convergence. Reinitialization parameter was set to 0.1 ms^{-1} and interface thickness was half of the maximum element size.

CFD model for droplet rise

Mass transfer between the continuous phase and droplet was calculated with a CFD-model using Comsol Multiphysics v.5.2 [36]. The surface velocity correction factor $k_{H,R}$ was determined with this model to take into account the drag increasing effect of surface active agents, local mass transfer coefficients K_{cu} and k_{CuA_2} of Cu transfer in continuous phase and in droplet (eqs. 12b, 12c) and the overall mass transfer coefficient K_D (eq. 12a).

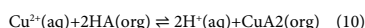
The system is modeled as a stationary spherical droplet and the continuous aqueous phase is moving with a measured terminal velocity. Both phases are separate calculation domains. The following assumptions are used: 2-d axisymmetric geometry, the spherical droplet, laminar velocity fields, steady and constant droplet volume.

Droplet was divided into two domains: stagnant cap zone having volume fraction of f_c and circulating zone with $1-f_c$ volume fraction.

The rectangular continuous phase domain width and height were set to 3 and 10 times the droplet diameter, respectively. Unstructured triangular mesh was used for the droplet and continuous phase domains. The fine grid resolution along the interface was created by specifying the amount of cells at the interface. Mesh sensitivity was tested by refining the grid near the interface. Variation of mass transfer coefficient was used as criteria for grid independence. Calculation was performed in two stages. In the first stage, laminar Navier-Stokes equation was solved to provide flow field. Boundary conditions for the continuous phase were: uniform velocity U_i at inlet, which is the experimentally determined droplet terminal velocity; sliding wall at calculation domain vertical sides; uniform velocity U_i at outlet. At droplet side $p=0$ as a pressure constraint; sliding wall with tangential velocity set to average interface velocity $\bar{U}_i = k_{H,R}U_i$ at droplet interphase; full rigid interface is simulated by setting $K_{H,R}$ to 0.

Boundary conditions for the droplet phase were: moving wall with radial velocity $u_d = u_r$ and axial velocity $w_d = w_c$ at droplet and continuous phase interface pressure is equal to pressure on the continuous side as pressure constraint. Species diffusivities presented in Table 2.

Boundary condition between organic and droplet phases is set by the interfacial reaction rate. The extraction of copper with a hydroxyoxime HA at the phase interface [37-39] is:



and the reaction rate equation is:

$$R_A(t) = k_{R,A} \frac{[Cu^{2+}(i)][HA(i)]^2}{[H^+(i)]} + \frac{k_{R,A}}{K_E} [CuA_2(i)][H^+(i)] \quad (11)$$

Where R_A is area based reaction rate, $k_{R,A}$ kinetic constant, K_E equilibrium constant and $[Cu^{2+}(i)]$, $[HA(i)]$, $[H^+(i)]$ and $[CuA_2(i)]$ are concentrations at the interface. Tamminen et al. [38] determined kinetic constant in a high shear reactor: $k_{R,A}^0 = 1.4 \times 10^{-3} \text{ dm}^4 / (\text{mol} \cdot \text{s})$. Equilibrium constant k_E is 8 at hydroxyoxime concentration 20vol-%=0.38 M [39]. In this work due to very mild hydrodynamic conditions, the expected kinetic constant will be lower than determined in the high shear experiments.

Overall mass transfer coefficient, K_D and local mass transfer coefficients on droplet and continuous phase side k_{CuA_2} and k_{cu} are determined from:

$$K_D = \frac{V_d ([CuA_2](t_R) - [CuA_2]_F)}{A_d \int_0^{t_R} \{ [CuA_2] - [CuA_2](t) \} dt} \quad (12a)$$

$$k_{cu} = \frac{V_d ([CuA_2](t_R) - [CuA_2]_F)}{A_d \int_0^{t_R} \{ [Cu^{2+}] - [Cu^{2+}(i)](t) \} dt} \quad (12b)$$

$$k_{d} = k_{CuA_2} = \frac{V_d ([CuA_2](t_R) - [CuA_2]_F)}{A_d \int_0^{t_R} \{ [CuA_2(i)](t) - [CuA_2] \} dt} \quad (12c)$$

$\overline{[CuA_2(i)]}$ and $\overline{[Cu^{2+}(i)]}$ are average concentrations at the phase interface.

Results and Discussion

The estimation and application of mass transfer models are described in Figure 4.

Droplet formation

In Table 3 is shown droplet experiment results. Droplet volumes were calculated using formula:

$$V_d = (\pi/6) d_{Maj}^2 d_{Min} \quad (13)$$

Average droplet volumes were 29 mm³ for the 0.8 mm needle and 10 mm³ for the 0.4 mm needle and corresponding average volume equivalent diameters d_v were 3.8 and 2.7 mm. Droplet average formation times t_f were estimated by dividing the average droplet volume with a feed rate: for the 0.8 mm needle 16, 5, 3 and 2 seconds and for the 0.4 mm needle 21, 4 and 3 seconds.

In Figure 5 is plotted the cumulative mass transfer Δn against the Fourier number and the and the cumulative transfer model by Popovich (eq. 1). The estimated value of the coefficient a_1 is 0.35. This is smaller than the minimum 0.857 noted by Wegener et al. [5] which confirms that in addition to diffusion there are other phenomena

X _{HA}	C _{HA}	ρ	μ	γ	Θ
vol-%	M	kg/m ³	mPas	mN/m	degrees
20	0.38	834	3	21.6	120

Table 1: The measured physical properties of Acorga M5640 solutions dissolved in Exxsol D80. Measurements at room temperature (22-24°C). Interfacial tension measured in 0.16 M CuSO₄ solution. pH of copper sulphate solution was adjusted to 3.1 with concentrated sulphuric acid.

Species	Cu ²⁺	H ⁺	HA	CuA ₂
D _m /10 ⁻⁹ m ² /s	0.72	9.4	0.46	0.3

Table 2: Species molecular diffusivities in 25°C, Cu²⁺ and H⁺ diffusivities are from Haynes [33], CuA₂ diffusivity and hydroxyoxime HA were estimated by Wilke-Chang method [34,35].

d _N	Q	d _{Maj}	D _{Min}	V _d	c _{F,m}	Re _N
mm	mL/min	mm	mm	mm ³	Mmol ⁻¹	
0.8 ^a	0.1	3.9	3.3	26	5.3	1.2
	0.3	3.9	3.4	27	1.7	3.4
	0.5	3.9	3.3	26	1	5.7
	0.7	3.8	3.2	24	0.8	8
0.4 ^b	0.04	3.1	2.7	14	6.1	1.1
	0.21	3	2.6	12	1.8	5.7
	0.29	3.3	20.8	16	1.3	8.0

Table 3: Measured droplet dimensions and concentrations with different feed rates Q after droplet formation. Symbols: d_N, needle diameter, d_{Maj}, d_{Min}, droplet major and minor axes lengths, V_d, droplet volume c_{F,m}, measured droplet concentration, Re_N, Reynolds number in needle outlet.

(interfacial reaction combined with effect of surfactants) and Popovich model does not follow experimental points.

In Figure 6 is plotted extraction ratio E versus square root of droplet modified Fourier number Fo_d using Walia and Vir model (eq. 2) with the overall effective diffusivity $D_{F,eff}$ using eq. (4). The fitted values of the surface mobility correction factor $k_{H,R}$ are 0.070 ($R^2=0.76$) for the 3.8 mm and 0.071 ($R^2=0.90$) for the 2.7 mm droplets and they are practically equal. The needle Reynolds numbers (Table 3) are less than 10 and according to the criteria proposed by Liang and Slater [4], droplet internal mass transfer is diffusion controlled. Therefore the eddy diffusivity was set to zero and the molecular diffusivity was used in calculation of the overall effective diffusivity. Compared to Popovich model Walia-Vir model combined with effective diffusivity model by Liang and Slater [4] is able to better describe mass transfer during droplet formation.

LS simulation and non-circular assumption

The non-circulatory assumption and the effect of contact angle on the formation hydrodynamics was examined by simulation of droplet formation with three different contact angles using LS method for the studied chemical system. Angles in simulations were 1, 120 and 179 degrees. Based on the simulation results shown in Figure 7 the velocity streamline profile is non-circulatory with the measured $\theta=120^\circ$. When the contact angle approaches 0° , the velocity profile becomes circulatory. Similar non-circulatory droplet formation hydrodynamics was recognized by Lu et al. [27]. Simulated and experimental formation times are shown in Table 4. For both needles experimental formation times $t_{F,m}$ are somewhat larger compared to the simulated times $T_{F,LS}$. Experimental formation time was determined by dividing droplet feed rate with average droplet volume. The experimental error in formation time determination is 10%, for the 0.8 mm needle formation time is between 1.5 to 1.7 seconds and for the 0.4 mm needle between 1.2 to 1.6 seconds. Interfacial tension is affected by copper extraction [40,41]. When the interfacial tension is 25.5 mNm^{-1} the simulated formation times equals the experimental value for the 0.8 mm needle.

Droplet rise

Based on concentration measurements during a droplet rise (Figure 2) it was recognized that reacted copper complex has a tendency stay at the droplet bottom zone. This supports the assumption of stagnant cap model. Terminal velocity measurements Tamminen et al. [6] gave substantially smaller values than determined from correlations for pure systems which is due to the presence of surfactants i.e., extractant, reducing the interface mobility. Low value of the measured terminal velocity (113 mm/s) corresponds well with the correlation given by Grace et al. [40] for contaminated systems. Based on this it is assumed that the interface is rigid thus signaling a very low value of interface mobility parameter $k_{H,R}$.

Two coefficients are to be determined experimentally when stagnant cap model is combined with effective diffusivity: stagnant volume fraction f_v and contamination coefficient $k_{H,R}$. In this work f_v is determined with image analysis. $k_{H,R}$ was set to zero based on the rigid interface assumption.

Volume fractions of stagnant cap were estimated by measuring droplet major and minor axis lengths and height of stagnant cap from the droplet image. Cap boundary was visually recognized and can also be seen in concentration profiles (Figure 2). Determination was repeated at least 15 times in order to estimate the variation. Fractions are shown in Table 5.

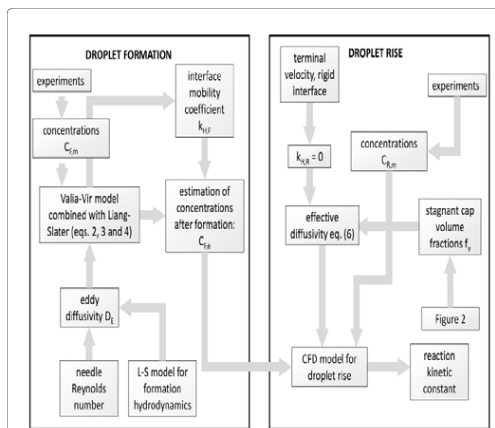


Figure 4: Flow diagram describing the calculation and application mass transfer models.

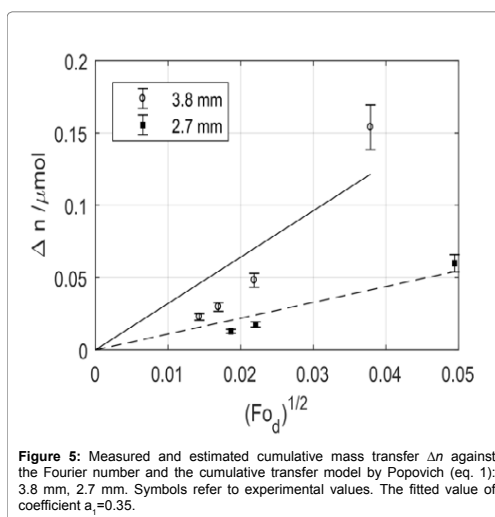


Figure 5: Measured and estimated cumulative mass transfer Δn against the Fourier number and the cumulative transfer model by Popovich (eq. 1): 3.8 mm, 2.7 mm. Symbols refer to experimental values. The fitted value of coefficient $a_1=0.35$.

Mass transfer simulation using CFD was performed for 0.8 mm needle. It was assumed that $k_{H,R}$ does not depend on the feed rate Q . Droplet concentration $C_{E,e}$ after formation was estimated using the model presented in the section *Mass transfer in droplet formation*. Droplet terminal velocity U_t was set to experimental value 113 mm/s. Droplet diameter was 3.8 mm and rise time 2.3 s. Droplet acceleration to terminal speed was neglected because of a very short acceleration time.

Value for the kinetic constant $k_{R,A}$ was found by fitting with the CFD model. The sum of squared difference between the estimated and measured concentrations was minimized:

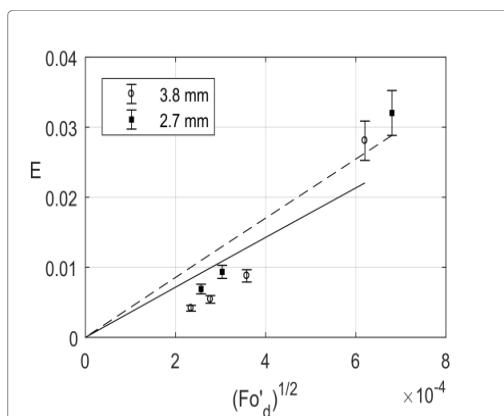


Figure 6: Measured and estimated extraction ratio E vs. square root of droplet modified Fourier number Fo'_d (eqs 2 and 4): 3.8 mm, 2.7 mm. Symbols refer to experimental values. Correction factor $k_{v,F}$ due to surface mobility is approximately 0.07 for both droplet sizes.

$$SSQ = \min \left(\sum_{j=1}^4 (c_{R,m,j} - c_{R,e,j})^2 \right) \quad (14)$$

$C_{R,m,j}$ is measured concentration in j :th feed flow and $C_{R,e,j}$ is the estimated concentration calculated with the CFD model.

Fitted value of $k_{R,A}$ is $0.13 \times 10^{-6} \text{ dm}^4/(\text{mol s})$. This is substantially smaller than reported by Tamminen et al. [38]. It is obviously due to different hydrodynamic conditions and smaller droplet size compared to this work. Estimated concentration after formation, and measured and estimated droplet concentrations after rise are shown in Table 5.

CFD model was used to calculate mass transfer coefficients using eqs. 12a-c. The most dense mesh (Table 6) was used. Mass transfer coefficients are $K_d=0.7 \times 10^{-6} \text{ m/s}$, $k_{CuA2}=13 \times 10^{-6} \text{ m/s}$ and $k_{Cu}=34 \times 10^{-6} \text{ m/s}$. Average K_d estimated from experiments is $2 \times 10^{-6} \text{ m/s}$. k_{CuA2} calculated from Newman model (eq. 8) with eddy diffusivity $D_{R,LS}=0$ (rigid interface) is $13 \times 10^{-6} \text{ m/s}$ which is same magnitude compared to value provided by the CFD model. Cu mass transfer coefficient k_{Cu} in continuous phase is estimated with a correlation proposed by Clift et al. [1].

$$Sh_c = 1 + Re^{0.48} Sc_c^{1/3} \quad (15)$$

With $U_i=113 \text{ mm/s}$, $d_c=3.8 \text{ mm}$, $\rho_c=1020 \text{ kg/m}^3$, $\mu_c=1.1 \text{ mPas}$ and $D_{Cu}=0.72 \times 10^{-9} \text{ m}^2/\text{s}$, Re is 388, $Sc_c=1498$, $Sh_c=146$ and $k_{Cu}=Sh_c D_{Cu}/d_c=28 \times 10^{-6} \text{ m/s}$. This is slightly smaller than the value 34×10^{-6} calculated from CFD model.

Fractional mass transfer resistances for continuous phase (m/k_{Cu})/(1/ K_d) is 2% and for droplet (1/ k_{CuA2}) / (1/ K_d) is 5%. Copper distribution ratio m between aqueous and droplet phase is 1.2. The reaction fractional resistance is 100%-7%=93% which is a substantial proportion of the total resistance. Similar results were also reported by Ferreira et al. [34].

Solution sensitivity for the selected mesh was tested by simulating using six meshes and calculating mass transfer coefficients (Table 6). Mass transfer coefficients are nearly constant when more than 1×10^6 mesh elements were used. Newman model assumes that mass transfer resistance is totally on the droplet side. Continuous side resistance is 2.5 times smaller than the droplet side but the reaction provides the

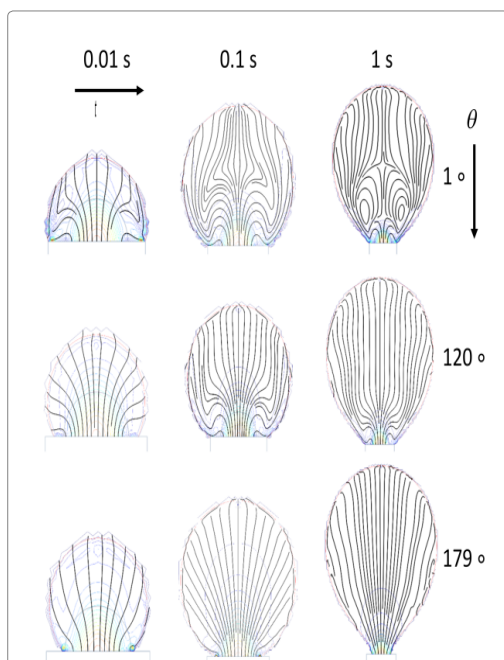


Figure 7: Simulated velocity profiles during droplet formation with different contact angles θ and different times. Feed rate Q is 1 ml/min and needle diameter 0.8 mm.

d_n mm	Q mL/min	$t_{F,LS}$ s	$t_{F,m}$ s	V_m mm ³	$V(t_{F,LS})$ mm ³	$V_{F,LS}$ mm ³
0.8	1	1.3	1.7	26	22	19.4
0.4	0.41	1.1	1.4	9.5	8.3	7.8

Table 4: Comparison of calculated and experimental formation times and volumes for both needles with maximum feed rate Q. $t_{F,LS}$: droplet formation time in simulation, $t_{F,m}$: experimental droplet formation time, V_m : experimental droplet volume, $V(t_{F,LS})=t_{F,LS} \times Q$ droplet volume at simulated formation time, $V_{F,LS}$: LS-method based droplet volume at the simulated droplet formation time $t_{F,LS}$.

Q mL/min	f_v	$C_{F,e}$ mmol/dm ³	$C_{R,m}$ mmol/dm ³	$C_{R,e}$ mmol/dm ³
0.1	0.39	4.1	5.1	4.6
0.3	0.25	2.3	2.5	2.8
0.5	0.23	1.8	2.1	2.3
0.7	0.25	1.5	2.1	2

Table 5: Stagnant cap fractions and estimated initial and measured and estimated final droplet copper complex concentrations. $K_{H,R}=0$ (=Rigid interface), estimated $k_{R,A}=0.13 \times 10^{-6} \text{ dm}^4/(\text{mol s})$. Symbols: Q feed rate, f_v stagnant cap fraction, $C_{F,e}$ estimated concentration after formation, eqs. (2 and 3), $C_{R,m}$ measured average concentration after the rise, $C_{R,e}$ estimated average droplet concentration after the rise.

N_{elem}	K_d 10^{-6} m/s	k_{CUIA2} 10^{-6} m/s	k_{Cu} 10^{-6} m/s
475000	0.6	15	50
670000	0.71	15	45
1060000	0.71	14	41
1300000	0.71	14	39
1580000	0.71	14	36
2240000	0.7	13	34

Table 6: Mass transfer coefficients using the CFD model with six meshes. Feed rate is 0.1 ml/min.

most of the resistance so validity to use only Newman model is not justified.

Conclusion

Based on simulation of a rising droplet using stagnant cap assumption and estimating an interfacial reaction kinetic constant it was found that value of measured kinetic constant with high shear reactors is much larger than estimated by simulation. This supports the hypothesis that in this case the interface provides a substantial mass transfer resistance which decreases the overall mass transfer coefficient. The effect is assumed to be due to the structure of the interface which is affected by the hydrodynamic conditions and in this case due to surfactants which probably is been adsorbed into the interface thus making it rigid and on the other hand slowing the reaction reactant's and product's mobility to and away the interface. For the formation stage as well it was found that an empirical model combined with effective diffusivity using interface mobility parameter to describe effect of surfactants is able to predict mass transfer in droplet formation better than a model assuming no explicit interfacial effects.

Acknowledgements

Authors gratefully acknowledge financial support from the Academy of Finland (Project "Analysis of polydispersity in reactive liquid-liquid systems").

Notations

a_i	Coefficient in eq (1)
c	Concentration, M
D	Diffusion coefficient, m^2/s
d	Diameter, m
d_e	Volume equivalent sphere diameter,
E	Extraction ratio
E_c	Extraction ratio assuming constant concentration,
f_v	Fraction of droplet stagnant zone
g	Gravitational acceleration, m/s^2
h	Height of droplet, mm
i	Species label
K	Overall mass transfer coefficient, m/s
K_E	Equilibrium constant in extraction reaction rate equation
k	Local mass transfer coefficient, m/s
k_E	Empirical coefficient in pseudo-eddy diffusivity equation
k_H	Interface mobility parameter
k_{RA}	Reaction kinetic constant, $\text{dm}^3/(\text{mol s})$
k_{RA}^0	Experimental kinetic constant determined in high shear reactor, $\text{dm}^3/(\text{mol s})$

m	Partition coefficient, distribution ratio between the phases
n	Molar amount, mol
N_{elem}	Number of elements in CFD mesh
p	Pressure, pa
Q	Feed rate, ml/min
R_A	Reaction rate, $\text{mol}/(\text{dm}^3 \text{ s})$
R^2	Coefficient of the determination for a fitted model
r	Radius, mm
t	Time, s
u	Radial velocity in cfd model, m/s
U	Velocity, m/s
V	Droplet volume, ml, mm^3
w	Axial velocity in cfd model, m/s
x	Volume fraction
z	Summing index
SSQ	Sum of squared differences

Greek alphabet

a	Species stoichiometric coefficient
Δ	Difference
γ	Interfacial tension, n/m
k	Viscosity ratio, μ_d/μ_c
μ	Viscosity, pa s
ρ	density, kg/m^3
Θ	Contact angle, degrees

Subscripts

-	Average
c	Continuous phase
d	Droplet
e	Estimated
E	Eddy diffusivity
Eff	Effective diffusivity
*	Equilibrium
F,c	Formation in cfd model
F	Formation
i	Interface, species index
LS	Levelset
Maj	Droplet major axis
Min	Droplet minor axis
m	Molecular, measured
N	Needle
R	Rise
0	Initial time, maximum value of reaction kinetic constant
	Terminal velocity

Abbreviations

(aq)	Aqueous phase
CFD	Computational fluid dynamics
Cu ²⁺	Copper ion
CuA2	Copper complex
DNS	Direct numerical simulation
H ⁺	Proton
HA	Hydroxyoxime
(i)	Interface
i.d. o.d	Needle inner and outer diameters
LS	Levelset
LLE	Liquid-liquid extraction
(org)	Organic phase
SDS	Sodium dodecyl sulphate
VOF	Volume-of-fluid

Dimensionless numbers

Fo _d	Droplet fourier number, $4D_{m,t}/d_e^2$
Fo' _d	Modified droplet fourier number, $4D_{F,ent}/d_e^2$
Maj	Droplet major axis
Re	Droplet reynolds number, $U_d \rho_d / \mu_c$
Re _n	Needle Reynolds number, $\bar{U}_n \rho_n d_n / \mu_d$
Sh _c	Continuous phase sherwood number, $k_c d / D_m$
SC _c	Continuous phase schmidt number, $\mu_d / (D_m \rho_c)$

References

- Clift R, Grace JR, Weber ME (1978) Bubbles, Droplets and particles, Dover Publication, USA.
- Licht W, Conway JB (1950) Mechanism of Solute Transfer in Spray Towers, Industrial & Engineering Chemistry 42: 1151-1157.
- Licht W, Pansing WF (1953) Solute Transfer from Single Drops in Liquid-Liquid Extraction. Industrial and Engineering Chemistry 45: 1885-1896.
- Liang TB, Slater MJ (1990) Liquid-liquid extraction drop formation: mass transfer and the influence of surfactant. Chemical Engineering Science 45: 97-105.
- Wegener M, Paul N, Kraume M (2014) Fluid dynamics and mass transfer at single droplets in liquid/liquid systems. International Journal of Heat and Mass Transfer 71: 475-495.
- Tamminen J, Lahdenperä E, Koironen T, Kuronen T, Eerola T, et al. (2017) Determination of single droplet sizes, velocities and concentrations with image analysis for reactive extraction of copper. Chemical Engineering Science 167: 54-65.
- Popovich AT, Jervis RE, Trass V (1964) Mass transfer during single drop formation. Chemical Engineering Science 19: 357-365.
- Walia DS, Vir D (1976) Extraction from single forming drops. The Chemical Engineering Journal 12: 133-141.
- Walia DS, Vir D (1976) Interphase mass transfer during drop or bubble formation, Chemical Engineering Science 31: 525-533.
- Heideger WJ, Wright MW (1986) Liquid extraction during drop formation: Effect of formation time. AIChE Journal 32: 1372-376.
- Kumar A, Hartland S (1999) Correlations for Prediction of Mass Transfer Coefficients in Single Drop Systems and Liquid-Liquid Extraction Columns. Chemical Engineering Research and Design 77: 372-384.
- Newman AB (1931) The Drying of Porous Solid: Diffusions and Surface Emission Equations. Trans. Am. Inst. Chem. Eng. 27: 203-220.
- Kronig R, Brink JC (1951) On the theory of extraction from falling droplets. Applied Scientific Research 2: 142-154.
- Handlos AE, Baron T (1957) Mass and heat transfer from drops in liquid-liquid extraction. AIChE Journal 3: 127-136.
- Henschke M, Pfennig A (1999) Mass-transfer enhancement in single-drop extraction experiments. AIChE Journal 45: 2079-2086.
- Henschke M, Pfennig A (2002) Influence of sieve trays on the mass transfer of single drops. AIChE Journal 48: 227-234.
- Altunok MY, Kalem M, Pfennig A (2012) Investigation of mass transfer on single droplets for the reactive extraction of zinc with D2EHPA. AIChE Journal 58: 1346-1355.
- Slater MJ (1995) A combined model of mass transfer coefficients for contaminated drop liquid-liquid systems. The Canadian Journal of Chemical Engineering 73: 462-469.
- Piarah WH, Paschedag AR, Kraume M (2001) Numerical simulation of mass transfer between a single drop and an ambient flow. AIChE Journal 47: 1701-1704.
- Wegener M, Paschedag AR, Kraume M (2009) Mass transfer enhancement through Marangoni instabilities during single drop formation. International Journal of Heat and Mass Transfer 52: 2673-2677.
- Jeon SJ, Pawelski A, Kraume M, Hong WH (2011) Mass transfer enhancement by the alkaline hydrolysis of ethyl acetate in a single droplet system. Journal of Industrial and Engineering Chemistry 17: 782-787.
- Pawelski A, Jeon SJ, Hong WH, Paschedag AR, Kraume M (2013) Interaction of a homogeneous chemical reaction and mass transfer in a single moving droplet. Chemical Engineering Science 104: 260-268.
- Deshpande KB, Zimmerman WB (2006) Simulation of interfacial mass transfer by droplet dynamics using the level set method. Chemical Engineering Science 61: 6486-6498.
- Yang C, Mao ZS (2005) Numerical simulation of interphase mass transfer with the level set approach. Chemical Engineering Science 60: 2643-2660.
- Kenig EY, Ganguli AA, Atmakidis T, Chasanis P (2011) A novel method to capture mass transfer phenomena at free fluid-fluid interfaces. Chemical Engineering and Processing: Process Intensification 50: 68-76.
- Wang Z, Lu P, Wang Y, Yang C, Mao Z (2013) Experimental investigation and numerical simulation of Marangoni effect induced by mass transfer during drop formation. AIChE Journal 59: 4424-4439.
- Lu P, Wang Z, Yang C, Mao ZS (2010) Experimental investigation and numerical simulation of mass transfer during drop formation. Chemical Engineering Science 65: 5517-5526.
- Soleymani A, Laari A, Turunen I (2008) Simulation of drop formation in a single hole in solvent extraction using the volume-of-fluid method, Chemical Engineering Research and Design. ECCE 686: 731-738.
- Lewis WK, Whitman WG (1924) Principles of gas absorption. Industrial and Engineering Chemistry 16: 1215-1220.
- Krishna R, Taylor R (1986) Multicomponent Mass Transfer: Theory and Applications. In Handbook of Heat and Mass Transfer. Chermisinoff NP (ed.), Volume 2: Mass transfer and reactor design. pp: 259-432.
- Hu Y, Liu Z, Yuan X, Zhang X (2017) Molecular mechanism for liquid-liquid extraction: Two-film theory revisited. AIChE Journal 63: 2464-2470.
- Adamson AW (1990) Physical Chemistry of Surfaces 5th Ed, Wiley, New York, USA, pp: 88.
- Haynes WM (2017) CRC Handbook of Chemistry and Physics, 97th Edition CRC Press.
- Ferreira AE, Agarwal S, Machado RM, Gameiro ML, Santos S, et al. (2010) Extraction of copper from acidic leach solution with Acorga M5640 using a pulsed sieve plate column. Hydrometallurgy 104: 66-75.
- Reid CR, Prausnitz JM, Poling BE (1987) The properties of gases and liquids (4th Ed.) McGraw-Hill, USA.
- COMSOL (2017) COMSOL Multiphysics V5.2.

Citation: Lahdenperä E, Tamminen J, Koiranen T, Kuronen T, Eerola T, et al. (2018) Modeling Mass Transfer During Single Organic Droplet Formation and Rise. *J Chem Eng Process Technol* 9: 378. doi: [10.4172/2157-7048.1000378](https://doi.org/10.4172/2157-7048.1000378)

Page 9 of 9

-
37. Szymanowski J (2000) Kinetics and interfacial phenomena. *Solvent Extraction and Ion Exchange* 18: 729-751.
38. Tamminen J, Sainio T, Paatero E (2013) Intensification of metal extraction with high-shear mixing. *Chemical Engineering and Processing: Process Intensification* 73: 119-128.
39. Vasilyev F, Virolainen S, Sainio T (2017) Modeling the phase equilibrium in liquid-liquid extraction of copper over a wide range of copper and hydroxyoxime extractant concentrations. *Chemical Engineering Science* 17: 88-99.
40. Inoue K, Tsunomachi H, Maruuchi T (1986) Interfacial adsorption equilibria of a hydroxyoxime and its metal chelates. *Journal of Chemical Engineering of Japan* 19: 131-133.
41. Grace JR, Wairegi T, Nguyen TH (1976) Shapes and Velocities of Single Drops and Bubbles Moving Freely through Immiscible Liquids. *Trans. Inst. Chem. Eng* 54: 167-173.

Publication IV

J. Tamminen, E. Lahdenperä, T. Koiranen, T. Kuronen, T. Eerola, L. Lensu,
H. Kälviäinen

**The mass transfer and coalescence time scales in binary droplet systems for copper
extraction**

Reprinted from *Journal of Chemical Engineering & Process Technology*, 9(4), 2018,
DOI: 10.4172/2157-7048.1000387



The Mass Transfer and Coalescence Time Scales in Binary Droplet Systems for Copper Extraction

Jussi Tamminen, Esko Lahdenperä, Tuomas Koironen, Toni Kuronen, Tuomas Eerola, Lasse Lensu and Heikki Kälviäinen

School of Engineering Science, Lappeenranta University of Technology, Lappeenranta, Finland

*Corresponding author: Lahdenperä E, School of Engineering Science, Lappeenranta University of Technology, Lappeenranta, Finland, Tel: +358505534258; E-mail: Esko.Lahdenpera@lut.fi

Received date: September 06, 2018; Accepted date: September 21, 2018; Published date: September 26, 2018

Copyright: © 2018 Tamminen J, et al. This is an open-access article distributed under the terms of the Creative Commons Attribution License, which permits unrestricted use, distribution, and reproduction in any medium, provided the original author and source are credited.

Abstract

In this work, we studied whether coalescence has a direct effect on mass transfer in copper extraction. The coalescence of pendant and sessile droplets containing diluted Acorga M5640 in an aqueous copper sulfate solution was recorded on video. The videos were analyzed to determine droplet rest times, sizes, and concentrations. Concentration measurements revealed that coalescence does not enhance mass transfer because coalescence is a rapid phenomenon. A comparison of the experiments performed with and without mass transfer showed that the coalescence dynamics are not affected by mass transfer. A bimodal rest time distribution was observed when the copper sulfate solution was in the continuous phase. The surface flows and cell-like structures observed on the droplet interface are presumed to be because of a Marangoni convection, which is caused by concentration changes because of extraction. The presence and absence of surface flow is anticipated to lead to a bimodal rest time distribution. The presence of surface flow improves coalescence probability because of very short binary droplet rest times.

Keywords: Binary droplet coalescence; Mass transfer; Copper extraction; Liquid-liquid extraction; Image analysis

Notations

a, b: Interpolation function parameters to fit apparent absorptivities

c: Concentration

d: Diameter

l: Length

n: Amount of copper

t: Time

x: Volume percentage

V: Volume

\dot{V} : Volumetric flow rate

Δ : Difference

ϵ : Absorptivity

χ : Chi-test

d_{outer} : Outer (diameter)

d_{inner} : Inner (diameter)

c: Continuous phase

d_{ch} : Chord length

coal: Coalesced

d: Droplet or droplet phase

t_f : Formation (time)

t_c : First contact between droplets

t_{ps} : Start of the feed pumps

t_p : Value for a pendant droplet

t_r : Rest (time)

t_s : Value for a sessile droplet

t_{sc} : Start of the film rupture between droplets

aq: Aqueous phase

CFD: Computational Fluid Dynamics

CuA_2 : Copper complex

HA: Hydroxyoxime i.e., active component of Acorga M5640

Org: Organic phase

Introduction

The basic operating principle in liquid-liquid extraction processes is to mix two phases and the driving force, that is, the deviation from the equilibrium, enables the solute to transfer between the phases. In addition to the driving force, the area available for mass transfer is an important parameter that can affect the mass transfer rate. The mass transfer area is increased by generating droplets using impellers, spargers, or perforated plates. In contacting units, droplets collide with each other and unit walls. Depending on the hydrodynamic conditions, two or more droplets can coalesce into one large droplet, or a single droplet can be broken into smaller droplets. Coalescence is expected to decrease the mass transfer rate by reducing the available mass transfer area.

The binary droplet, that is, droplet-droplet coalescence, has been studied using different operating principles. For example, researchers

[1-4] have studied the coalescence of pendant and sessile droplets, while other group of researchers [5-10] studied the coalescence of adjacent droplet or bubble pairs. The droplet pair was either a pendant or sessile. Eiswirth [11] studied the coalescence of free rising droplets. Mitra and Ghosh [12] have used a different approach, where the set-up consisted of a series of cup-type cells immersed in the continuous phase.

Several studies using binary droplets [1,8,13] have revealed that the coalescence rate depends on the direction of mass transfer. When the direction was from the continuous to dispersed phase, coalescence times increased compared with the opposite direction. Solute concentrations because of the Marangoni convection are also expected to affect coalescence [14]. The effect of droplet size on coalescence was studied by Villwock, Gebauer, et al. [2], and their results indicated that coalescence proceeds only if a rising droplet is larger than a stationary pendant droplet. In experiments with sessile and pendant droplets, on the other hand, Kamp and Kraume [1] were not able to find a clear relationship between the droplet size ratio and coalescence. Some studies have also explored the effect of different additives on coalescence. For example, Mitra and Ghosh [12] found that surfactant addition leads to a notable increase in droplet rest times. The addition of a small amount of salt increased the coalescence times, whereas when increasing the amount of salt, shorter rest times were observed. These studies, however, have not analyzed whether binary droplet coalescence itself influences mass transfer because of interface deformations.

In the present work, the goal was to study whether the coalescence phenomenon itself has any effect on mass transfer because of deformations and movement during the binary droplet coalescence; here, sessile and pendant organic droplets were formed in ambient aqueous solution and using a direct measurement method. Droplet concentrations were determined before and after the coalescence, and the effect of coalescence on mass transfer was determined [15]. The organic feed contained commercial copper extractants in a commercial hydrocarbon diluent; the continuous phase was a copper sulfate solution. The feeds used in the present work are complex compared with the pure liquids used in most literature studies. Typical coalescence studies with mass transfer consist of chemical systems where one substance is transferred between two immiscible phases, and there is no chemical reaction present; in addition, the direction of the mass transfer can be easily controlled. This contrasts with the chemical system used in the present work.

Copper extraction is an interfacial equilibrium reaction, one where copper is complexed at the interface, and the complex is then transferred to the organic phase. Copper (Cu^{2+}) extraction with hydroxyoxime (HA) has the following stoichiometry [16-18].



The reaction mechanism for copper extraction with LIX 65N was presented [16] and has been applied on copper extraction with extractants such as LIX 984 [17] and Acorga M5640 [18]. Copper extraction is also an ion exchange reaction; hydrogen ions are released as aqueous phase copper is complexed with hydroxyoxime. This further complicates the situation because the mass transfer direction is not well defined because there is mass transfer to and from both phases. Also, the transferring species are changing because of the complex formation.

In the current study, the copper concentration in the organic droplets was determined using the image frames of recorded videos, which were analyzed with the image analysis method proposed by Tamminen et al. [15]. The measured copper concentrations in the droplets before and after coalescence (film rupture) were compared with each other. The comparison revealed that the coalescence had a minor effect on the mass transfer mainly because of the short time scale.

Materials and Methods

Experimental set-up

The set-up for the coalescence experiments was custom-made (Figure 1). The pendant and sessile droplets were formed on the tips of two identical steel needles. The droplet formation was made by dispensing the droplet phase with two identical high-precision syringe pumps (World Precision Instruments). The cell was made of PVC plastic, and the top was left open. Two opposite side walls were made from transparent glass to allow for video recording. The set-up used here was like those used previously [1,2]. The volume used in earlier works [1,2] was 500 cm^3 , but in this work, the set-up volume was smaller, 100 cm^3 . It is noted here that although both droplets were attached to needle tips, experiments with one stationary and one moving droplet can be made with the present set-up. The organic feed solution consisted of technical grade chemicals, but organic feeds were not used in extraction prior to the coalescence experiments. The preparation of the feed solutions is described in the supplementary information.

Coalescence experiments

The droplets were formed on the tips of the needles. The pumps were started manually, but they were programmed to dispense a predetermined volume ($8 \mu\text{L}$) at a constant flow rate of $0.4 \text{ cm}^3/\text{min}$. The pumps were set to stop automatically. The same volumetric flow rate setting was used in both pumps. The distance between the needle tips was set to 5 mm, putting the formed droplets in contact with each other. Because the contact between the droplets was gentle, the mass transfer during the coalescence could be studied in the absence of possible mixing effects from droplet collision. All experiments conducted at room temperature.

The experiments were repeated 150 times for the 20 vol% Acorga solution droplets when the continuous phase copper sulfate solution concentration was 0.16 mol/L . The mass transfer during the coalescence was studied by varying the droplet phase extractant concentration and the continuous aqueous phase copper sulfate concentration. Ten repetitions were made to show whether coalescence has any effect on mass transfer when the feed concentrations are changed.

The videos of the coalescence of the pendant and sessile droplets were recorded in color using a Casio Ex-F1 digital camera at a frame rate of 300 fps. The image resolution in the physical dimensions was determined by recording a 5 mm grid with a transparent background. The details of the calibration procedure and concentration analysis are reported [15]. The frame size was 512×384 pixels, which corresponds approximately to $13 \times 10 \text{ mm}$. Three close-up lenses (+1, +2, and +4 diopter) [19] were attached to the camera lens to have a more detailed view of the droplet. The camera settings were kept constant in all experiments. The recorded videos were later manually analyzed for

droplet formation, rest, and coalescence times. The droplet sizes and concentrations were determined from the recorded video frames using an image analysis. The image analysis of all experiments was made for individual video frames, which were extracted from the video using FFmpeg [20]. All image and data analyses were done using MATLAB version 2016a [21].

The concentration analysis of the droplets was conducted using a method [15], with the exception that the droplet region selection was done manually. Recorded droplet image data were correlated with concentrations using the measured droplet geometry and Lambert-Beer law. The experimental results are presented in more detail by Peltola [22]. The measured concentration data are characterized by using the mode, which shows the most typical value of the data set.

The droplet sizes were measured based on fitting ellipsoids to the droplet image data. The lengths of the droplets' minor and major axes were calculated from the measured ellipse dimensions. The droplets were assumed to have a rotational symmetry along the y-axis; that is, it was assumed that the x- and z-axis lengths were equal (Figure 1).

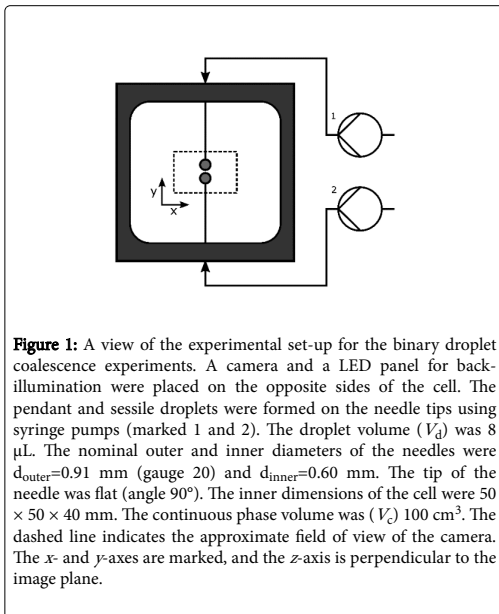


Figure 1: A view of the experimental set-up for the binary droplet coalescence experiments. A camera and a LED panel for back-illumination were placed on the opposite sides of the cell. The pendant and sessile droplets were formed on the needle tips using syringe pumps (marked 1 and 2). The droplet volume (V_d) was 8 μL . The nominal outer and inner diameters of the needles were $d_{\text{outer}}=0.91$ mm (gauge 20) and $d_{\text{inner}}=0.60$ mm. The tip of the needle was flat (angle 90°). The inner dimensions of the cell were $50 \times 50 \times 40$ mm. The continuous phase volume was (V_c) 100 cm^3 . The dashed line indicates the approximate field of view of the camera. The x- and y-axes are marked, and the z-axis is perpendicular to the image plane.

Light scattering and refraction generally cause the droplet image edge to be darker than the image center, and this was considered by calculating the apparent absorptivities (ϵ) of standard solution droplets [15]. An interpolation function was fitted to the apparent absorptivities and was used in the calculation of the concentrations in the droplet. The interpolation function is $\epsilon = a/\ln(l_{ch} + 1) + b$, where a and b are parameters, and l_{ch} is the chord length [15]. The parameters of the interpolation function used in the current work are shown in Table S1. The analysis in the present work was carried out using the method described in an earlier work [15], except the green color channel and a different camera were used. A different camera was used in the present work because the camera used in earlier work had an insufficient

frame rate (7.5 fps) for the current coalescence experiments. The calibration was made for copper containing 10 and 20 vol% Acorga-solution droplets. The continuous phase was 0.16 mol/L $(\text{NH}_4)_2\text{SO}_4$ solution.

The droplet copper concentrations were measured just before and after coalescence. For each coalescence experiment, the concentration difference (Δc) is calculated from the following:

$$\Delta c = c_{\text{coal}} - \frac{(n_s + n_p)}{(V_s + V_p)} \quad (2)$$

where the amount of copper complex in the sessile and pendant droplets is n_s and n_p , respectively. The volumes of the droplets are V_s (sessile) and V_p (pendant). The concentration in a coalesced droplet is $c_{\text{coal}} = n_{\text{coal}}/V_{\text{coal}}$.

The times of the coalescence process were determined from the video by counting the relevant frames. The droplet formation time (t_f) is as follows:

$$t_f = t_{fc} - t_{ps} \quad (3)$$

where t_f is the difference between the start time of pumping (t_{ps}) and the time of the first contact (t_{fc}) between the pendant and sessile droplets. The droplet rest time (t_r) is as follows:

$$t_r = t_{sc} - t_{fc} \quad (4)$$

where t_{sc} is the start time of film rupture. The time between the interfacial film rupture and the formation of the coalesced droplet is the coalescence time (t_{coal}). Droplet contact time describes the time available for mass transfer, that is, in practice, the sum of the formation and rest times.

The coalescence hydrodynamics modeling

The hydrodynamics in the coalescence of sessile and pendant droplets were simulated using Comsol Multiphysics v5.2 [23] software. The two-phase laminar Level-Set method was used to track the droplet-ambient interface in coalescence modeling. The model was implemented without mass transfer and extraction reaction. The main objective of the computational fluid dynamics (CFD) simulation was to determine whether the coalescence of the droplets was affected mainly by the hydrodynamic conditions or whether the mass transfer had any effect on the coalescence process.

The details of the CFD model are described in the supplementary information.

Results and Discussion

Copper reactive extraction

Figure 2 shows a schematic presentation of the reaction. The copper is complexed with the hydroxyoxime at the droplet interface, and a brown-colored copper complex (CuA_2) is formed as the result of the reaction. The time for the reaction (22 s) for the droplet in Figure 2 was not long enough for the diffusion of the complex to fill the droplet, leaving the complex near the droplet surface. At the beginning of the experiment, the droplet was filled with a lighter-colored hydroxyoxime solution. In the image, the droplet's center is observed through two interfaces and layers with a higher complex concentration, which causes the center of the image to have a brown color. Figure 2 is

consistent with the copper extraction being an interfacial reaction and having a low complex concentration in the droplet center.

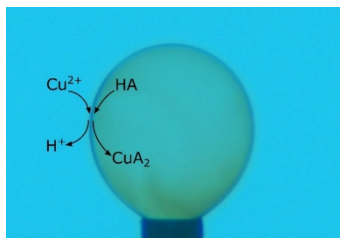


Figure 2: The copper extraction in a sessile organic droplet containing 20 vol% Acorga M5640. The copper extraction reaction (Eq. 1) can be seen to proceed at the droplet interface. Copper cation (Cu^{2+}) reacts with hydroxyoxime (HA) and releases hydrogen ions (H^+) into the aqueous phase. The formed brown-colored complex (CuA_2) can be observed at the droplet surface, especially near the droplet's edge. The continuous phase was the aqueous CuSO_4 solution at a concentration (c_c) of 0.16 mol/L. The droplet has been in contact with the continuous phase 22 s.

Determined rest and formation times

The droplet rest times were determined from the coalescence videos of 20 vol% Acorga M5640 droplets (Figure 3) with 0.16 mol/L ammonium sulfate solution as the continuous phase. Without any copper transfer, the droplet rest time has a wide distribution, with a median of 10 s, and the rest times were normally distributed according to the results of the χ -test for normality.

On the other hand, the rest times obtained from the copper sulfate binary coalescence experiments have a bimodal distribution (Figure 3b). Most of the observations (about 120 of 150) have rest times shorter than 0.5 s. The other observations have much longer rest times, about 2-3 s. If both the long and short rest times are treated as individual data sets, they are both normally distributed according to the χ -test for normality. Thus, the bimodal distribution implies that there are two different phenomena or mechanisms affecting droplet coalescence during copper extraction.

The droplet phase extractant and continuous phase copper concentrations have no clear effect on the observed droplet rest times (Figure S1). These results imply that the measured rest time distributions at the different feed concentrations are like those presented in Figure 3b. Ten measurements were made when the extractant and copper feed concentrations were varied.

The formation times of the pendant and sessile droplets are typically almost equal, but because the feed pumps and droplet formation were started manually, there can be differences. The formation times of the single experiment pendant and sessile droplets are parallel determinations, and the average of them is used as a formation time in the further data analysis.

A short needle distance and low droplet approach velocities were chosen to maximize the probability of droplet contact. Droplet pairs came into contact in all the coalescence experiments, but coalescence

did not always occur. This effect was the most prominent when 0.50 mol/L copper sulfate was used as the feed solution. It is acknowledged here that the frame rate of the camera (300 Hz) was perhaps too low for a detailed coalescence study. However, it is considered enough for determining droplet formation and rest times, which are long compared with the frame interval (3.3 ms).

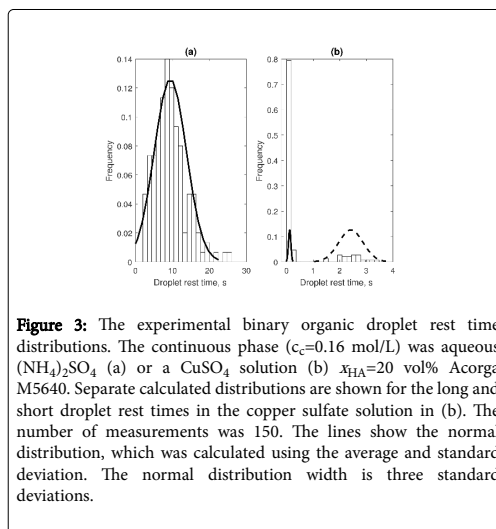


Figure 3: The experimental binary organic droplet rest time distributions. The continuous phase ($c_c=0.16$ mol/L) was aqueous $(\text{NH}_4)_2\text{SO}_4$ (a) or a CuSO_4 solution (b) $x_{\text{HA}}=20$ vol% Acorga M5640. Separate calculated distributions are shown for the long and short droplet rest times in the copper sulfate solution in (b). The number of measurements was 150. The lines show the normal distribution, which was calculated using the average and standard deviation. The normal distribution width is three standard deviations.

Mass transfer during coalescence

The mass transfer during the binary organic droplet coalescence was studied by determining the concentrations in the droplets before and after coalescence, that is, before and after the film rupture and combination of the droplets. The measured concentrations in the pendant and sessile droplets are almost equal because they almost have the same contact times. Like the formation times, the pendant and sessile droplet concentrations of one experiment are considered parallel determinations. The average of the pendant and sessile droplet concentration is the measure of droplet concentration before coalescence (Figure 4).

The concentration (in the coalesced droplet) after coalescence was found to be like the concentration before coalescence. The coalescence time was about 30 ms, as can be seen in the section Coalescence dynamics. This is a short time for the mass transfer to take place. Therefore, all the measured concentrations are essentially the same (Figure 4). In Figure 4, the variation of the concentration data is due to the variation in droplet contact times, that is, in the formation and rest times.

The concentration differences in coalescence are calculated from Eq. 2 and are shown in Figure 5. The calculated differences are small, and some are even negative. The experimental conditions used in the present work are such that copper extraction proceeds according to forward reaction (Eq. 1), and the copper complex concentration is expected to remain the same or increase. However, in Figure 5 [15], certain trends can be observed, but it is believed that they are caused by the experimental variation.

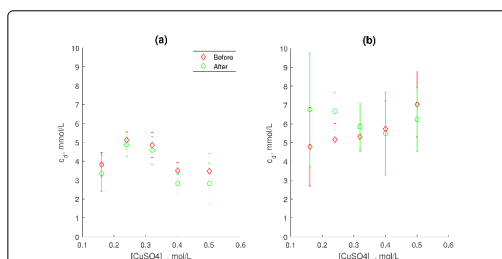


Figure 4: The modes of droplet concentration distributions before and after coalescence. The droplet phase was either 10 (a) or 20 vol % Acorga M5640 (b). The continuous phase was the aqueous copper sulfate solution having an initial concentration $[CuSO_4]_0$. The concentrations before coalescence are an average of the pendant and sessile droplet concentrations. The error bars indicate one standard deviation.

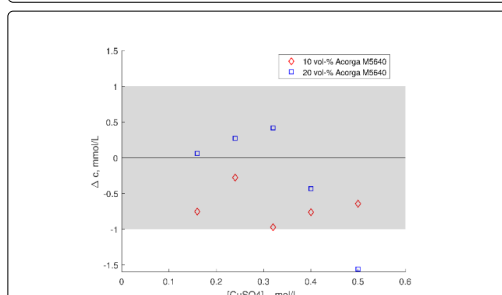


Figure 5: The mode of concentration differences during binary droplet coalescence. The concentration difference was defined as the difference between the droplet concentrations before and after coalescence (see Eq. 2). The difference was calculated separately for each experiment, and as a result, the mode of each data set is presented. The droplet phase was the organic Acorga M5640 solution, and the continuous phase was the copper sulfate solution. The shaded area shows the reproducibility of the method.

The concentration values before and after coalescence are approximately equal (Figure 4), and the subtraction of concentrations can then lead to negative values because of concentration measurement accuracy. The calculated negative concentration differences imply that coalescence does not enhance mass transfer. The variation in the concentration differences and in the measured concentration data (Figure 4) are similar. The variation is approximately 4 mmol/L. The data show that binary droplet coalescence has no major effect on the mass transfer in copper extraction within the studied concentration range, which is mainly because of a short coalescence time (about 30 ms). However, coalescence has an indirect effect on mass transfer because it changes the interfacial area available for extraction.

Coalescence dynamics

The droplet coalescence dynamics from the film rupture to the combination of the pendant and sessile droplet volumes is shown in Figure 6. Coalescence in 0.16 mol/L ammonium (no mass transfer) and copper sulfate (with mass transfer) show that the coalescence dynamics are very similar in both cases. Here, the droplet phase is essentially the same in both cases because the measured organic phase copper concentration was below 10 mmol/L. In Figure 6, the third row shows the coalescence simulation results. The measurements and simulation match remarkably well, implying that the duration of coalescence is defined by the bulk properties of the droplet phase as the droplet contents are flowing together. The simulation and experimental results in Figure 6 indicate that chemical reaction (Eq. 1) and presence of a Marangoni convection (Figures 7 and 8) do not affect droplet combination dynamics.

The coalescence time is approximately the same (about 27 ms) in the experiments and simulations. It is noted here that determining the coalescence time would indeed be more accurate if a higher frame rate would have been used in the experiments. However, how the current study determined coalescence time is considered to have enough accuracy for the purposes of this work. According to Eiswirth [11], the duration of the coalescence of equal-sized toluene droplets in water was 30 ms; this is the same order of magnitude found in the current work (Figure 6). The difference is presumed to be because of the differences in the physical properties of the feeds, such as density, viscosity, and interfacial tension.

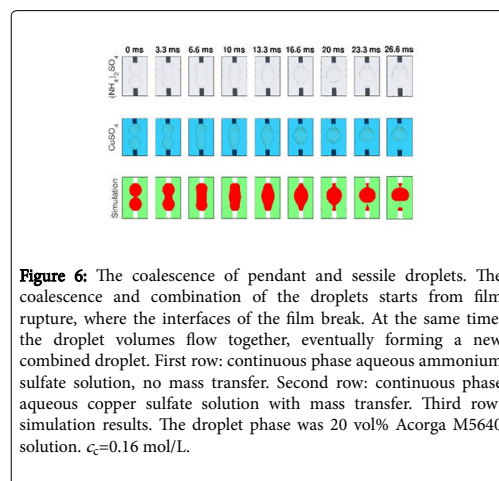


Figure 6: The coalescence of pendant and sessile droplets. The coalescence and combination of the droplets starts from film rupture, where the interfaces of the film break. At the same time, the droplet volumes flow together, eventually forming a new combined droplet. First row: continuous phase aqueous ammonium sulfate solution, no mass transfer. Second row: continuous phase aqueous copper sulfate solution with mass transfer. Third row: simulation results. The droplet phase was 20 vol% Acorga M5640 solution. $c_c=0.16$ mol/L.

The droplet contents are not mixed together in coalescence. The features present in the pendant and sessile droplets prior to coalescence also tend to be visible in the coalesced droplet. In the case of the copper sulfate experiment shown in Figure 6, there is a noncolored layer in the middle of the combined droplet that is being formed. This feature can be seen quite early on, and it remains visible throughout the rest of the coalescence event. The noncolored layer is the result of surface flows away from the droplet apices during later stages of the droplet approach. An example of these surface flows is shown in Figure 7. It is reported that the droplet contents are not

mixed in coalescence when the droplets are similar in size, as is case in the current work [11]. The droplet deformations are then similar because of the symmetry in droplet interactions. This leads to a balance in the forces on both sides of the coalesced droplet. When the droplet sizes are different, the lack of symmetry leads to internal mixing in the coalesced droplet.

Surface flows and marangoni convection

The observed bimodal rest time distribution for copper extraction implies the presence of two phenomena that each have a different effect on coalescence. The presence (and absence) of surface flow (Figures 7 and 8) could be one such phenomenon, where interfacial tension driven flow may lead to the breakage of the film and, thus, coalescence [24].

A surface flow starts from the apex of the droplet and moves toward the needle, and it is made visible because of the strong color of the copper complex (Figure 7). In the case of a pendant droplet, the surface flow was observed to move upwards, away from the droplet apex. The lighter-colored areas on the droplet surfaces contain mostly the extractant, and the darker colored areas contain more of the copper complex (Figures 7 and 8). The surface flow is presumed to be caused by a thin-film type of Marangoni convection [24]. The flow starts from the droplet apex where the film between droplets is the thinnest. The surface-active extractant moves into the thinnest part of the film faster than the other parts, leading to a decrease of the interfacial tension in the droplet apex. Because the interfacial tension is the lowest at the droplet apex, the Marangoni convection direction is away from it [14,24].

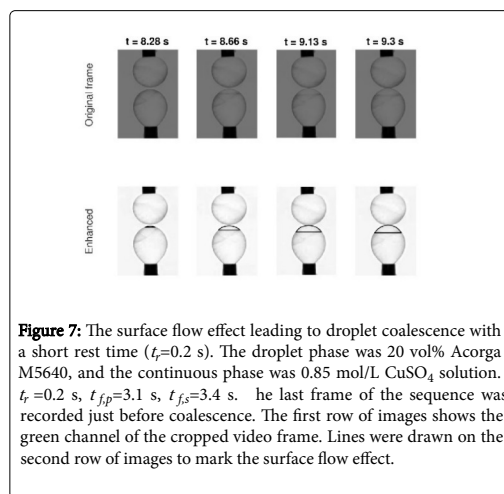


Figure 7: The surface flow effect leading to droplet coalescence with a short rest time ($t_r=0.2$ s). The droplet phase was 20 vol% Acorga M5640, and the continuous phase was 0.85 mol/L CuSO_4 solution. $t_r=0.2$ s, $t_{fp}=3.1$ s, $t_{fs}=3.4$ s. The last frame of the sequence was recorded just before coalescence. The first row of images shows the green channel of the cropped video frame. Lines were drawn on the second row of images to mark the surface flow effect.

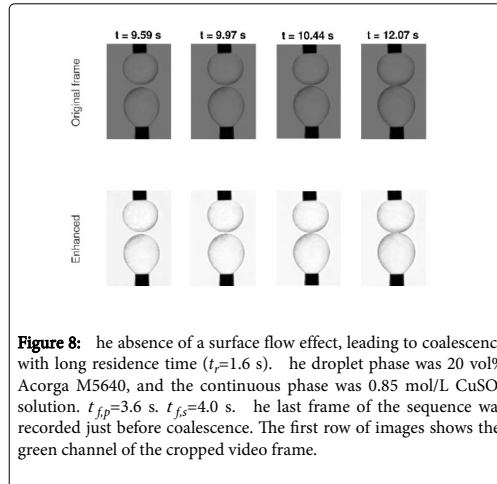


Figure 8: The absence of a surface flow effect, leading to coalescence with long residence time ($t_r=1.6$ s). The droplet phase was 20 vol% Acorga M5640, and the continuous phase was 0.85 mol/L CuSO_4 solution. $t_{fp}=3.6$ s, $t_{fs}=4.0$ s. The last frame of the sequence was recorded just before coalescence. The first row of images shows the green channel of the cropped video frame.

The presence of the surface flow, that is, a thin-film Marangoni phenomenon, leads to a more rapid coalescence by shortening the droplet rest time (Figure 9). Surface flows were not observed in every droplet coalescence experiment. When it occurred, it was observed in either the pendant, sessile, or even in both droplets simultaneously. Figure 9 shows that in practically all cases where the surface flows because of a thin-film Marangoni convection, there were short rest times.

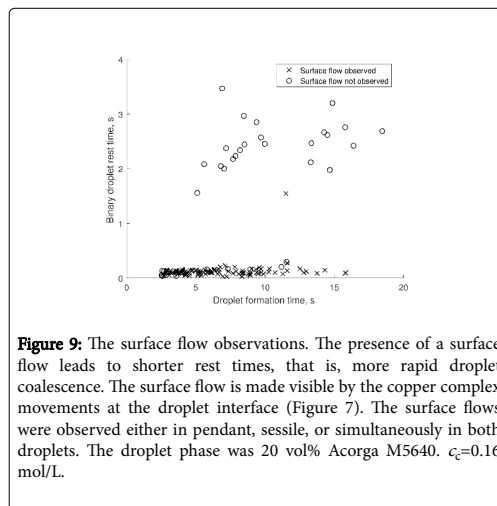


Figure 9: The surface flow observations. The presence of a surface flow leads to shorter rest times, that is, more rapid droplet coalescence. The surface flow is made visible by the copper complex movements at the droplet interface (Figure 7). The surface flows were observed either in pendant, sessile, or simultaneously in both droplets. The droplet phase was 20 vol% Acorga M5640. $c_c=0.16$ mol/L.

The long rest times shown in Figure 9 were observed when the droplet formation time is over 5 s. The data shown in Figure 9 also imply that the thin-film Marangoni convection induced fast coalescence depending on the droplet contact time.

Conclusions

Copper mass transfer into extractant solution droplets during binary droplet coalescence was studied in the present work. The coalescence experiments of pendant and sessile droplets were performed in a custom-made cell and recorded using a digital camera. The organic phase contained Acorga M5640 extractant dissolved in Exxsol D80. The continuous phases were copper sulfate solutions. The coalescence experiments in an ammonium sulfate solution were made for comparison purposes.

In the ammonium sulfate solutions, the observed rest times were normally distributed, with an average of about 10 s. In the copper sulfate solutions, a bimodal distribution was found. Long rest times of about 2 s were observed when there was no surface flow present. On the other hand, the observation of a surface flow was typically found to lead to much shorter droplet rest times (below 0.5 s), thus increasing the coalescence probability. It is assumed that the surface flow was caused by a thin-film Marangoni phenomenon.

An image analysis was used to determine the droplet concentrations; they were measured before and after coalescence to determine whether coalescence had effect on the mass transfer. The concentration analysis showed no increase in the coalesced droplet concentrations; thus, the mass transfer in copper extraction was not enhanced during binary droplet coalescence. Copper extraction is an interfacial reaction, and as such, it is limited by the interfacial area and diffusion of the reactants to the interface. During a short coalescence time (30 ms), mass transfer has no time to significantly effect on the concentrations, even if the driving force has been increased because of mixing. The situation may be different when extraction without a chemical reaction is made. The results can be used to enhance and simplify the flow models because coalescence will cause an interfacial area change, and no extra effects then must be considered when using the model.

Acknowledgements

Authors gratefully acknowledge financial support from the Academy of Finland (Project "Analysis of polydispersity in reactive liquid-liquid systems").

References

- Kamp J, Kraume M (2014) Influence of drop size and superimposed mass transfer on coalescence in liquid/liquid dispersions-test cell design for single drop investigations. *Chemical Engineering Research and Design* 92: 635-643.
- Villwock J, Gebauer F, Kamp J, Bart HJ, Kraume M (2014) Systematic analysis of single droplet coalescence. *Chemical Engineering & Technology* 37: 1103-1111.
- Gebauer F, Villwock J, Kraume M, Bart HJ (2016) Detailed analysis of single drop coalescence-Influence of ions on film drainage and coalescence time. *Chemical Engineering Research and Design* 115: 282-291.
- Chen Y, Shen C, Peterson GP (2015) Hydrodynamics and morphologies of droplet coalescence. *Industrial & Engineering Chemistry Research* 54: 9257-9262.
- Ata S, Davis ES, Dupin D, Armes SP, Wanless EJ (2010) Direct observation of pH-induced coalescence of latex-stabilized bubbles using high-speed video imaging. *Langmuir* 26: 7865-7874.
- Ata S, Pugh RJ, Jameson GJ (2011) The influence of interfacial ageing and temperature on the coalescence of oil droplets in water. *Colloids and Surfaces A: Physicochemical and Engineering Aspects* 374: 96-101.
- Morse AJ, Tan SY, Giakoumatos EC, Webber GB, Armes SP, et al. (2014) Arrested coalescence behaviour of giant Pickering droplets and colloidosomes stabilised by poly (tert-butylaminoethyl methacrylate) latexes. *Soft Matter* 10: 5669-5681.
- Ban T, Kawaiyumi F, Nii S, Takahashi K (2000) Study of drop coalescence behavior for liquid-liquid extraction operation. *Chemical Engineering Science* 55: 5385-5391.
- Wang W, Gong J, Ngan KH, Angeli P (2009) Effect of glycerol on the binary coalescence of water drops in stagnant oil phase. *Chemical Engineering Research and Design* 87: 1640-1648.
- Sagert NH, Quinn MJ (1979) The coalescence of n-hexane droplets in aqueous solutions of n-alcohols. *The Canadian Journal of Chemical Engineering* 57: 29-34.
- Eiswirth RT (2014) Binary droplet coalescence of rising droplets. Doctoral Thesis, Technische Universität Kaiserslautern, Kaiserslautern, Germany.
- Mitra T, Ghosh P (2007) Binary coalescence of water drops in organic media in presence of ionic surfactants and salts. *Journal of Dispersion Science and Technology* 28: 785-792.
- Chevallier JP, Klaseboer E, Masbernat O, Gourdon C (2006) Effect of mass transfer on the film drainage between colliding drops. *Journal of Colloid and Interface Science* 299: 472-485.
- Wegener M, Paul N, Kraume M (2014) Fluid dynamics and mass transfer at single droplets in liquid/liquid systems. *International Journal of Heat and Mass Transfer* 71: 475-495.
- Tamminen J, Lahdenperä E, Koiranen T, Kuronen T, Eerola T, et al. (2017). Determination of single droplet sizes, velocities and concentrations with image analysis for reactive extraction of copper. *Chemical Engineering Science* 167: 54-65.
- Flett DS, Okuhara DN, Spink DR (1973) Solvent extraction of copper by hydroxy oximes. *Journal of Inorganic and Nuclear Chemistry* 35: 2471-2487.
- Tamminen J, Sainio T, Paatero E (2013) Intensification of metal extraction with high-shear mixing. *Chemical Engineering and Processing: Process Intensification* 73: 119-128.
- Vasilyev F, Virolainen S, Sainio T (2017) Modeling the phase equilibrium in liquid-liquid extraction of copper over a wide range of copper and hydroxyoxime extractant concentrations. *Chemical Engineering Science* 171: 88-99.
- Kood International (2017) Accessed 11.9.2017.
- Ffmpeg, Version 20160728-fb91143 (2016) Accessed 29.7.2016.
- MathWorks Inc. (2016) MATLAB release 2016a. Natick, Massachusetts, United States.
- Peltola R (2017) Droplet coalescence and breakage in reactive liquid-liquid extraction. Master's Thesis, Lappeenranta University of Technology, Lappeenranta, Finland.
- COMSOL (2017) COMSOL Multiphysics v5.2. COMSOL AB, Stockholm, Sweden.
- Perez de Ortiz ES (1992) Marangoni phenomena. *JD Thornton, Science and Practice of Liquid-Liquid Extraction* 1: 157.

The mass transfer and coalescence time scales in binary droplet systems for copper extraction

Supplementary information

Jussi Tamminen, Esko Lahdenperä, Tuomas Koiranen, Toni Kuronen, Tuomas Eerola, Lasse Lensu and Heikki Kälviäinen

School of Engineering Science, Lappeenranta University of Technology; P.O. Box 20, FIN-53851 Lappeenranta, Finland

Preparation of feed solutions

The extractant used in experiments was Acorga M5640 (Lot n:o P3GBA524A) from Cytec Solvay Group. The extractant pretreatment and dilution procedure has been described by Tamminen et al. [15]. 10 and 20 vol% solutions of the extractant were used. The corresponding extractant active component (hydroxyoxime) concentrations were 0.2 and 0.38 mol/L, respectively. The diluent was Exxsol D80 from Exxon Mobil Chemical. The extractant and diluent used in the present work are typical to industrial copper extraction processes. The diluted extractant solutions consist of technical-grade chemicals; it is noted here that organic solutions were not used in extraction prior to the coalescence experiments. Any impurities present in the organic feed originated from manufacture processes and hence were not removed in the extractant pretreatment.

The aqueous copper and ammonium sulfate feed solutions were prepared by dissolving analysis-grade copper or ammonium sulfate salt into purified water. The ammonium sulfate solution concentration was 0.16 mol/L. The copper sulfate solution concentrations ($[\text{CuSO}_4]_0$)

were 0.16, 0.24, 0.32, 0.40, and 0.50 mol/L. The initial pH of the aqueous feed solutions were adjusted to 3.1 by using concentrated sulfuric acid.

The parameters of the apparent absorption interpolation function

Table A.1: The concentration calibration in coalescence experiments. The calibration parameters were determined from the standard solution droplet image data. The apparent absorptivity interpolation function parameters (a and b) were determined from the green channel data. Note that the values of a and b are not identical to the values presented in an earlier work [15] because of the different camera and color channel used in the current analysis.

$x_{\text{HA}}, \text{vol}\%$	$a, \text{L}/\text{mmol} \cdot \text{mm}$	$b, \text{L}/\text{mmol} \cdot \text{mm}$
10	4.0×10^{-3}	-1.3×10^{-3}
20	3.0×10^{-3}	-4.9×10^{-4}

The coalescence hydrodynamics model

Formation and coalescence were simulated in the present work using Comsol Multiphysics v.5.2 [23] software and the two-phase laminar Level-Set method. A 2-d axisymmetric geometry was used. The geometry and boundary conditions are shown in Fig. A.1.

Two needles having the diameters $d_{\text{outer}} = 0.91 \text{ mm}$ and $d_{\text{inner}} = 0.60 \text{ mm}$ were used for modelling the inlets. The feed flow rate \dot{V} was set to $0.4 \text{ cm}^3/\text{min}$. The initial droplet volumes V_d were $8.4 \text{ }\mu\text{L}$. The properties of the aqueous and organic phases were set to the properties of 0.16 mol/L copper sulfate solution and 20 vol% Acorga-solution. The contact angle at the fluid-solid interface is set to 120° based on separate measurements. The interfacial tension was 22 mN/m . The densities and viscosities of the organic (droplet) and aqueous (continuous) phases were 834 kg/m^3 , $3.03 \times 10^{-3} \text{ Pa} \cdot \text{s}$ and 1020 kg/m^3 , $1.01 \times 10^{-3} \text{ Pa} \cdot \text{s}$, respectively.

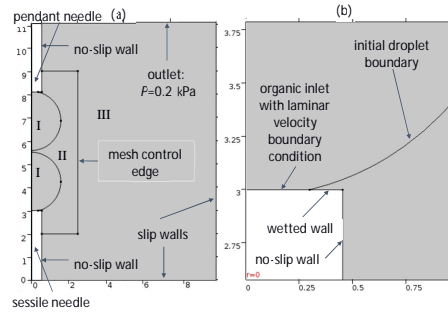


Figure A.1: 2-d axial symmetric CFD geometry and the boundary conditions. Figure (a) shows whole calculation domain and (b) details of the needle tip. The calculation domain has the width of 10 mm and the height of 11 mm. The domain bottom and side walls have free slip boundary conditions. The needle vertical sides are set to no-slip wall conditions, and the needle tip is a wetted wall. The domain top is the outlet, and the pressure is set to the hydrostatic pressure generated by the aqueous phase column on top of the calculation domain. The pressure is 0.2 kPa. The inlet flow is laminar.

The calculation grid consisted of three domains (Fig. A.1) that were meshed using triangular elements. The mesh element limits (max/min) for the exterior space of the droplets (domain III) were 450 and 20 μm . In the mesh control domain (domain II), the limits were set to 100 and 1 μm . In the droplet (domain I), the limits were 80 and 1 μm . The amount of the mesh elements totaled 105×103 .

Initially, both the phase velocities and pressures were set to 0. At the start of the transient adaptive time-step solution, the droplet feed was increased from 0 to the maximum feed using a smooth step function, and it was kept at this rate until the end of the simulation for computational stability. It is assumed that effect on the results is negligible. The calculated simulation time was 30 ms, which corresponds to the experimentally determined time for the coalescence of the pendant and sessile droplets.

The default Level-Set solver was used. Two user controllable Level-Set parameters, the reinitialization parameter, and the interface thickness parameter were adjusted to reach convergence. The reinitialization parameter was set to 0.01 m/s, and the interface thickness parameter was half of the maximum element size.

The rest time distributions measured at different feed concentrations

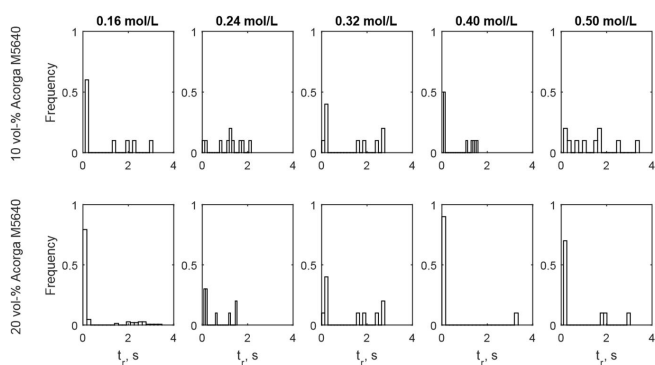


Figure A.2: The experimental droplet rest time distributions at different feed concentrations. $x_{HA} = 10$ or 20 vol% Acorga M5640. The continuous phase was an aqueous copper sulfate solution ($[CuSO_4] = 0.16 - 0.85$ mol/L). The number of measurements was 150 (droplet phase was 20 vol% Acorga M5640, $c_c = 0.16$ mol/L) or 10 (all other measurements).

ACTA UNIVERSITATIS LAPPEENRANTAENSIS

838. GOLMAEI, SEYEDMOHAMMAD. Novel treatment methods for green liquor dregs and enhancing circular economy in kraft pulp mills. 2018. Diss.
839. GERAMI TEHRANI, MOHAMMAD. Mechanical design guidelines of an electric vehicle powertrain. 2019. Diss.
840. MUSIIENKO, DENYS. Ni-Mn-Ga magnetic shape memory alloy for precise high-speed actuation in micro-magneto-mechanical systems. 2019. Diss.
841. BELIAEVA, TATIANA. Complementarity and contextualization of firm-level strategic orientations. 2019. Diss.
842. EFIMOV-SOINI, NIKOLAI. Ideation stage in computer-aided design. 2019. Diss.
843. BUZUKU, SHQIPE. Enhancement of decision-making in complex organizations: A systems engineering approach. 2019. Diss.
844. SHCHERBACHEVA, ANNA. Agent-based modelling for epidemiological applications. 2019. Diss.
845. YLIJOKI, OSSI. Big data - towards data-driven business. 2019. Diss.
846. KOISTINEN, KATARIINA. Actors in sustainability transitions. 2019. Diss.
847. GRADOV, DMITRY. Experimentally validated numerical modelling of reacting multiphase flows in stirred tank reactors. 2019. Diss.
848. ALMPANOPOULOU, ARGYRO. Knowledge ecosystem formation: an institutional and organisational perspective. 2019. Diss.
849. AMELI, ALIREZA. Supercritical CO₂ numerical modelling and turbomachinery design. 2019. Diss.
850. RENEV, IVAN. Automation of the conceptual design process in construction industry using ideas generation techniques. 2019. Diss.
851. AVRAMENKO, ANNA. CFD-based optimization for wind turbine locations in a wind park. 2019. Diss.
852. RISSANEN, TOMMI. Perspectives on business model experimentation in internationalizing high-tech companies. 2019. Diss.
853. HASSANZADEH, AIDIN. Advanced techniques for unsupervised classification of remote sensing hyperspectral images. 2019. Diss.
854. POPOVIC, TAMARA. Quantitative indicators of social sustainability applicable in process systems engineering. 2019. Diss.
855. RAMASAMY, DEEPIKA. Selective recovery of rare earth elements from diluted aqueous streams using N- and O –coordination ligand grafted organic-inorganic hybrid composites. 2019. Diss.
856. IFTEKHAR, SIDRA. Synthesis of hybrid bio-nanocomposites and their application for the removal of rare earth elements from synthetic wastewater. 2019. Diss.

857. HUIKURI, MARKO. Modelling and disturbance compensation of a permanent magnet linear motor with a discontinuous track 2019. Diss.
858. AALTO, MIKA. Agent-based modeling as part of biomass supply system research. 2019. Diss.
859. IVANOVA, TATYANA. Atomic layer deposition of catalytic materials for environmental protection. 2019. Diss.
860. SOKOLOV, ALEXANDER. Pulsed corona discharge for wastewater treatment and modification of organic materials. 2019. Diss.
861. DOSHI, BHAIRAVI. Towards a sustainable valorisation of spilled oil by establishing a green chemistry between a surface active moiety of chitosan and oils. 2019. Diss.
862. KHADIJEH, NEKOUEIAN. Modification of carbon-based electrodes using metal nanostructures: Application to voltammetric determination of some pharmaceutical and biological compounds. 2019. Diss.
863. HANSKI, JYRI. Supporting strategic asset management in complex and uncertain decision contexts. 2019. Diss.
864. OTRA-AHO, VILLE. A project management office as a project organization's strategizing tool. 2019. Diss.
865. HILTUNEN, SALLA. Hydrothermal stability of microfibrillated cellulose. 2019. Diss.
866. GURUNG, KHUM. Membrane bioreactor for the removal of emerging contaminants from municipal wastewater and its viability of integrating advanced oxidation processes. 2019. Diss.
867. AWAN, USAMA. Inter-firm relationship leading towards social sustainability in export manufacturing firms. 2019. Diss.
868. SAVCHENKO, DMITRII. Testing microservice applications. 2019. Diss.
869. KARHU, MIIKKA. On weldability of thick section austenitic stainless steel using laser processes. 2019. Diss.
870. KUPARINEN, KATJA. Transforming the chemical pulp industry – From an emitter to a source of negative CO2 emissions. 2019. Diss.
871. HUJALA, ELINA. Quantification of large steam bubble oscillations and chugging using image analysis. 2019. Diss.
872. ZHIDCHENKO, VICTOR. Methods for lifecycle support of hydraulically actuated mobile working machines using IoT and digital twin concepts. 2019. Diss.
873. EGOROV, DMITRY. Ferrite permanent magnet hysteresis loss in rotating electrical machinery. 2019. Diss.
874. PALMER, CAROLIN. Psychological aspects of entrepreneurship – How personality and cognitive abilities influence leadership. 2019. Diss.
875. TALÁSEK, TOMÁS. The linguistic approximation of fuzzy models outputs. 2019. Diss.



ISBN 978-952-335-436-4
ISBN 978-952-335-437-1 (PDF)
ISSN-L 1456-4491
ISSN 1456-4491
Lappeenranta 2019